


<b>Title</b>	Electron beam lithography assisted high-resolution pattern generation
<b>Author(s)</b>	Gangnaik, Anushka S.
<b>Publication date</b>	2015
<b>Original citation</b>	Gangnaik, A. 2015. Electron beam lithography assisted high-resolution pattern generation. PhD Thesis, University College Cork.
<b>Type of publication</b>	Doctoral thesis
<b>Rights</b>	<p>© 2015, Anushka Gangnaik.</p> <p><a href="http://creativecommons.org/licenses/by-nc-nd/3.0/">http://creativecommons.org/licenses/by-nc-nd/3.0/</a></p> 
<b>Item downloaded from</b>	<a href="http://hdl.handle.net/10468/2441">http://hdl.handle.net/10468/2441</a>

Downloaded on 2018-08-23T17:52:55Z



# **ELECTRON BEAM LITHOGRAPHY ASSISTED HIGH-RESOLUTION PATTERN GENERATION**

**Anushka Gangnaik, B.Sc.**

*Tyndall National Institute and Department of Chemistry,*

*University College Cork.*

*Ireland.*

**Presented for the PhD. Degree to the National University of Ireland,  
Cork**

**Supervisor**

**Prof. Justin D. Holmes**

**October 2015**



## Declaration

I, Anushka Gangnaik, certify that this Thesis is my own work and I have not obtained a degree in this University or elsewhere on the basis of this PhD Thesis.

---

Anushka Gangnaik

## ABSTRACT

This thesis details the top-down fabrication of nanostructures on Si and Ge substrates by electron beam lithography (EBL). Various polymeric resist materials were used to create nanopatterns by EBL and Chapter 1 discusses the development characteristics of these resists. Chapter 3 describes the processing parameters, resolution and topographical and structural changes of a new EBL resist known as ‘SML’. A comparison between SML and the standard resists PMMA and ZEP520A was undertaken to determine the suitability of SML as an EBL resist. It was established that SML is capable of high-resolution patterning and showed good pattern transfer capabilities.

Germanium is a desirable material for use in microelectronic applications due to a number of superior qualities over silicon. EBL patterning of Ge with high-resolution hydrogen silsesquioxane (HSQ) resist is however difficult due to the presence of native surface oxides. Thus, to combat this problem a new technique for passivating Ge surfaces prior to EBL processes is detailed in Chapter 4. The surface passivation was carried out using simple acids like citric acid and acetic acid. The acids were gentle on the surface and enabled the formation of high-resolution arrays of Ge nanowires using HSQ resist.

Chapter 5 details the directed self-assembly (DSA) of block copolymers (BCPs) on EBL patterned Si and, for the very first time, Ge surfaces. DSA of BCPs on template substrates is a promising technology for high volume and cost effective nanofabrication. The BCP employed for this study was poly (styrene-*b*-ethylene oxide) and the substrates were pre-defined by HSQ templates produced by EBL. The DSA technique resulted into pattern rectification (ordering in BCP) and in pattern multiplication within smaller areas.



## ACKNOWLEDGEMENTS

At every stage of our lives, there are various people who contribute to our good fortune. The journey through my PhD has been a remarkable one and indeed, there are many people whom I would like to give credit to.

I will firstly express my deepest gratitude to my supervisor, Prof. Justin D. Holmes, for providing me with this valuable opportunity to come to Cork and to study under his remarkable guidance at U.C.C. He has been an excellent guide right from my very first day at Cork (although, I missed him at the coach station!) till my ultimate days in UCC. I would also take this opportunity to thank him and his family for being the warmest hosts for all the Christmas Days that I spent in Cork.

The next person I am prominently grateful to is Prof. Yordan M. Georgiev. It was a truly an exceptional experience working with him and I was lucky to have a calming source of energy around to escape to daily hustle-bustle of Tyndall. His support has been of utmost importance during my PhD for gaining all knowledge that I have about the electron beam lithography. Personally and professionally, he has been a great encouragement for me in Tyndall and in Cork.

The next two girls who made Tyndall a fun place are Michele “Shelly” Conroy and Roisin Kelly. It was always fun to have them around whilst having some intelligent ‘EBL, germanium and nano-rods’ conversations. I would also like to acknowledge all the members of our MCAG group for their friendships and for their assistance at some stage during my time here; Subhajit, Nikolay, John, Michael, Pat Carolan (thanks, for answering all the EBL calls!), Gillian, Jessica, Giuseppe, Brenda and Ray Duffy. Lab 343 is no different to ours, so the very first thanks would be to Tandra (ji) who was not only a good guide, but a good friend. My warmest gratitude towards Cian and Tim (had a hard time understanding their Cork accent!), Atul T., Ram Shankar, Sola Raj, Elsa, Parvaneh and the lovely lady, Barbara. I would also

like to take a little space here to mention our ex-group member, Richard Hobbs, who had been kind to me and very informative about the work that I undertook from him.

The cleanroom in Tyndall had been a second home to me, and I made some very good friends there too. I would like to express my thankfulness towards Dan O'C., Ann F., Brendan McC., Carmel M., James O'C., John J., Richard D. and Pat C.. I have had a very good company in Tyndall to keep me cherished throughout, which resulting into some strong friendships here; Monika, Illias, Azura, Shirin, many more and the friendliest Security blokes; acknowledging everyone would probably require more pages than my thesis. An authentic shout-out to all my "Desi-friends" in Tyndall; Gangotri, Dhiman, Umar, Usman, Asfwan, Gautam, Anil, Tuhin, Nitin, Charles and Santosh. My very good friend, Anjana, thanks for being the positivity around. Also, a very exceptional mention to John Hanley, who's petite, antique garage (Jack Hanley & Son) falls on my way to Tyndall. He surely did cheer me up every time I would meet him!

My deepest appreciations are towards these guys, who encouraged me (pushed me, rather!) to undertake the PhD in the first place; Pavan, Kawal and Amar. Cheers to Puneet, for being there. The support of my friends from back home was never sparse - Ashwini, Apoorva, Aniruddha, Sanil, Sagar, Abhishek, Skand and Yatin. Lastly, a huge shout-out to Atul Chaudhari! For being my constant company at home, in UCC, in the lab and basically in the whole of Cork! This is a friendship I will cherish for many years to come (a mention to Akshay Kumar, too!).

Finally, the supreme strength of my life - my mom and my dad. I can never thank them enough for their constant support and love that they shower upon me and for making me the person that I am today.

Above all, the biggest 'Thank you' would be to Lord Ganpati for His continuous supply of blessings which guides to a better self-assembly of me as a person!

## LIST OF PUBLICATIONS

**Anushka Gangnaik**, Yordan M. Georgiev, Brendan McCarthy, Nikolay Petkov, Vladimir Djara and Justin D. Holmes. *Characterisation of a novel electron beam lithography resist, SML and its comparison to PMMA and ZEP resists*. Microelectronic Engineering, 1<sup>st</sup> July 2014, Volume 123, 126.

**Anushka Gangnaik**, Yordan M. Georgiev and Justin D. Holmes. “*Correlation of Lithographic Performance of the Electron Beam Resists SML and ZEP with their Chemical Structure*”. Journal of Vacuum Science & Technology B, 8<sup>th</sup> July 2015, Volume 33, 041601.

Ray Duffy, Maryam Shayesteh, Kevin Thomas, Emanuele Pelucchi, Ran Yu, **Anushka Gangnaik**, Yordan M. Georgiev, Patrick Carolan, Nikolay Petkov, Brenda Long and Justin D. Holmes. *Access resistance reduction in Ge nanowires and substrates based on non-destructive gas-source dopant in-diffusion*. Journal of Material Chemistry, 25<sup>th</sup> September 2014, Volume 48 (2), 9248.

Cian Cummins, Roisin A. Kelly, **Anushka Gangnaik**, Yordan M. Georgiev, Nikolay Petkov, Justin D. Holmes and Michael A. Morris. *Solvent Vapor Annealing of Block Copolymers in Confined Topographies: Commensurability Considerations for Nanolithography*. Macromolecular Rapid Communications, April 2015, Volume 36 (8), 762.

Cian Cummins, **Anushka Gangnaik**, Roisin Ann Kelly, Dipu Borah, John O'Connell, Nikolay Petkov, Yordan M. Georgiev, Justin D. Holmes and Michael A. Morris. *Aligned Silicon Nanofins via the Directed Self-Assembly of PS-*b*-P4VP Block Copolymer and Metal Oxide Enhanced Pattern Transfer*. Nanoscale, 2<sup>nd</sup> April 2015, Volume 7 (15), 6712.

John O'Connell, Giuseppe Verni, **Anushka Gangnaik**, Maryam Shayesteh, Brenda Long, Yordan M. Georgiev, Nikolay Petkov, Gerard McGlacken, Michael Morris and Ray Duffy. “*Organo-arsenic molecular layers on silicon for high density*

*doping.*” ACS Applied Materials & Interface. 26<sup>th</sup> June 2015, Volume 7 (28), 15514.

Cian Cummins, **Anushka Gangnaik**, Roisin A. Kelly, Alan J. Hydes, John O’Connell, Nikolay Petkov, Yordan M. Georgiev, Dipu Borah, Justin D. Holmes and Michael A. Morris. “*Parallel Arrays of Sub-10 nm Aligned Germanium Nanofins from an ‘In-situ’ Metal Oxide Hardmask using Directed Self-Assembly of Block Copolymer.*” Chemistry of Materials, 11<sup>th</sup> August 2015, Volume 27 (17), 6091.

Roisin A. Kelly, Bartosz Liedke, Stefan Baldauf, **Anushka Gangnaik**, Subhajit Biswas, Yordan M. Georgiev, Justin D. Holmes, Matthias Posselt and Nikolay Petkov. “*Epitaxial post-implant recrystallization in Germanium nanowires*”. Crystal Growth and Design, 14<sup>th</sup> August 2015, Volume 15 (9), 4581.

**Anushka Gangnaik**. “*How man fabricates nano-sized objects*”. The Boolean, 2014, Pages 36-41.

Brenda Long, Giuseppe A. Verni, John O’Connell, Maryam Shayesteh, **Anushka Gangnaik**, Yordan M. Georgiev, Patrick Carolan, Dan O’Connell, K. J. Kuhn, Scott B. Clendenning, Roger Nagle, Ray Duffy and Justin D. Holmes. “*Doping Top-down E-Beam Fabricated Germanium Nanowires Using Molecular Monolayers*”. (Submitted to Journal of Materials Chemistry C on 1<sup>st</sup> May 2015).

*Dedicated to Ganpati, Mummy and Pappa*

*“Happiness can be found even in the darkest of times,*

*if one only remembers to turn on the light.”*

*-Albus Dumbledore*

## TABLE OF CONTENTS

<b>DECLARATION</b>	<b>i</b>
<b>ABSTRACT</b>	<b>ii</b>
<b>ACKNOWLEDGEMENTS</b>	<b>iii</b>
<b>LIST OF PUBLICATIONS</b>	<b>v</b>
<b>1. INTRODUCTION</b>	<b>1</b>
1.1. THE PHOTOLITHOGRAPHY PROCESS	3
1.2. THE CHARGED PARTICLE LITHOGRAPHY	5
1.3. ELECTRON BEAM LITHOGRAPHY	6
1.3.1 CONTRAST AND SENSITIVITY	7
1.3.2 DEVELOPER SOLVENTS	9
1.3.3 TEMPERATURE	11
1.3.4 AUXILIARY FACTORS	14
1.4. EBL RESIST FAMILIES	16
1.4.1 CHEMICALLY AMPLIFIED RESISTS (CARS)	18
1.4.2 NON-CARS	22
1.4.3 FULLERENE DERIVATIVES RESISTS	24
1.4.4 METHYLACRYLATE RESISTS	30
1.4.5 INORGANIC RESISTS	33
1.4.6 MISCELLANEOUS RESISTS	37
1.5. LITHOGRAPHY BY GRAPHOEPI TAXY	42
1.6. ADVANCED LITHOGRAPHY	53
1.7. CONCLUSION	54
1.8. THESIS SUMMARY	60
1.9. BIBLIOGRAPHY	60
<b>2. EQUIPMENT AND EXPERIMENTAL</b>	<b>68</b>
2.1. PHYSICAL TOOLS	68

2.1.1	ELECTRON BEAM LITHOGRAPHY SYSTEM	68
2.1.2	PATTERN TRANSFER TOOLS	69
2.1.3	PATTERN TRANSFER : ETCHING TECHNIQUE	70
2.1.4	PATTERN TRANSFER : METAL LIFT-OFF TECHNIQUE	72
2.1.5	SCANNING ELECTRON MICROSCOPE	73
2.1.6	SURFACE PROFILER	74
2.1.7	FOURIER TRANSFORM INFRARED (FTIR) SPECTROSCOPY	75
2.2.	EXPERIMENTAL	75
2.2.1	RESIST CHARACTERISATION	76
2.2.2	PATTERNING GERMANIUM WITH HSQ RESIST	78
2.2.3	DIRECTED SELF-ASSEMBLY OF BLOCK COPOLYMERS ON Si AND Ge SURFACES	83
2.3	BIBLIOGRAPHY	86
	<b>3. SML RESIST CHARACTERISATION</b>	<b>88</b>
3.1.	RESULTS AND DISCUSSIONS	91
3.1.1	CONTRAST CURVES	91
3.1.2	LITHOGRAPHY QUALITY	95
3.1.3	PATTERN TRANSFER CAPABILITIES	97
3.1.4	ROUGHNESS MEASUREMENTS	103
3.1.5	FTIR MEASUREMENTS	109
3.2.	CONCLUSION	115
3.3.	BIBLIOGRAPHY	116
	<b>4. PATTERNING OF GERMANIUM SURFACE WITH HSQ RESIST</b>	<b>119</b>
4.1.	RESULT AND DISCUSSION	122
4.1.1	GERMANIUM PATTERNING WITH ACID TREATMENT	122
4.1.2	XPS ANALYSIS	124
4.1.3	FTIR ANALYSIS	125
4.1.4	LITHOGRAPHIC QUALITY	129
4.2.	APPLICATIONS	132



4.2.1	FOUR PROBE NANOWIRE DEVICE FABRICATION	132
4.2.2	SUSPENDED GERMANIUM NANOWIRES	137
4.2.3	PATTERNING FOR DIRECTED SELF-ASSEMBLY OF BLOCK COPOLYMERS	140
4.3.	CONCLUSIONS	142
4.4.	BIBLIOGRAPHY	143
<b>5.</b>	<b>DIRECTED SELF ASSEMBLY OF BLOCK COPOLYMERS ON Si AND Ge SURFACES</b>	<b>146</b>
5.1.	RESULTS	148
5.1.1	DSA WITH VARIED CONDITIONS ON SILICON SUBSTRATES	148
5.1.2	IRON INCLUSION	156
5.1.3	PATTERN TRANSFER	158
5.1.4	DISCUSSION	160
5.1.5	CONCLUSION FOR SILICON	161
5.2.	GERMANIUM SUBSTRATES	162
5.2.1	DSA ON GE WITH VARIED SURFACE CONDITIONS	162
5.2.2	IRON INCLUSION ON GE	169
5.2.3	PATTERN TRANSFER ON GE	171
5.2.4	CONCLUSION FOR GERMANIUM	173
5.3.	BIBLIOGRAPHY	174
<b>6.</b>	<b>CONCLUSIONS</b>	<b>178</b>
6.1.	FUTURE WORKS	182

# CHAPTER 1

---

## INTRODUCTION

## 1. INTRODUCTION

The inquisitive nature of human beings has led to great evolutionary discoveries. In an effort to make life easier, tools such as axes, spears and arrows were invented in early life. With the increase in the cranial capacity, technology started to improve and get more complex. The appearance of modern humans resulted in an expansion in technology and many new scientific discoveries. First, great findings in the fields of agriculture, textile, manufacturing, mining and transportation were made. This was followed by the invention of electricity and electricity driven devices and machines. Technology from then has improved immensely and new concepts put forward during this period formed the fundamentals of today's knowledge. Present-day technology is largely based on the miniaturisation of devices, leading to novel but complex scientific breakthroughs, is universally known as “*nanotechnology*”.

Nanotechnology is more generally defined as the art and science of shaping matter in such a way that resulting structures (nanostructures) have at least one dimension between 1 and 100 nm. Nanotechnology covers a large range of scientific fields from chemistry, physics, biology and engineering to micro-fabrication, surface science and medicine. Nanotechnology research is also very diverse and includes nanodevice fabrication, molecular self-assembly techniques and generation of new materials. Nanotechnology has enabled us to achieve advanced, superior and powerful products used for the betterment of human life, and to some extent the destruction as well! Due to promising outcomes from this nanotechnology, Governments all over the World are investing enormous amount of money for

research and development in this field. The USA government based programme National Nanotechnology Initiative (NNI) will have spent approximately \$21 billion dollars on nanotechnology from 2001 to 2015.<sup>1</sup> The annual total public and private sector funding worldwide for nanotechnology is around \$13-14 billion. Estimates from the 2008 show that the European Union spending was €3.5 billion.<sup>2</sup>

One of the most prominent applications of nanotechnology is in the semiconductor industry, due to the miniaturisation of complex circuitry in microelectronic devices. This scaling down of size has pushed the scale limit of integrated circuits to beyond sub-50 nm and hence demands for fabrication methods with superior performance. There are two fundamental approaches on the basis of which nanofabrication is currently carried out: Bottom-up and Top-down approaches. These two approaches can be applied individually or in combination. The top-down approach involves carving out nanostructures from bulk substrates to remove material and can involve several processes, *e.g.* lithography combined with additive/subtractive processes of pattern transfer, such as thin film deposition, implantation, diffusion, etching, *etc.* Bottom-up approaches act in the reverse direction, *i.e.* the nanostructures are formed by starting from atomic/molecular elements which are gradually assembled until the desired structure is obtained; through processes such as the self-assembly of molecules, nanoscaffolding, *etc.*

The top-down approach is still the prevailing technique in the micro- and nanoelectronics industry. Nanolithography plays a central role in this approach, where a stencil with the required pattern is created in a sacrificial layer called “resist”, deposited on the main working material, *e.g.* silicon (Si). Nanolithography

techniques include photolithography, electron beam lithography (EBL), soft lithography, nanoimprint lithography (NIL), X-ray lithography, photon beam lithography (PBL), scanning probe lithography and the directed self-assembly (DSA) of block co-polymers (BCP).

In general, nanolithography is a branch of lithography that deals not only with nanoscale fabrication, but also includes the study and application of the nanostructures formed. Early records of lithography date back to the late 19<sup>th</sup> century. Nicéphore Niépce, the inventor of photography, first recognised the technique of lithography in 1882.<sup>3</sup> He created patterns by using asphalt mixed in lavender oil and stones. His technique involved treating paper with the oil, on which stones were placed, and leaving the paper under sunlight for two to three hours. Areas that were shielded from the sun remained softer than the unshielded areas and were easily washed off with lavender oil, leaving behind a pattern formed by the shaded areas. Over the years, photolithography has advanced immensely and is now widely used in the semiconductor industry.

### 1.1 THE PHOTOLITHOGRAPHY PROCESS

Photolithography is the most commonly used lithographic processes. Based on Niépce's method, modern photolithographic processes use light of various wavelengths to create desired patterns. Typically, a suitable base substrate is coated with a thin film of a polymeric substance called a 'resist'. A photomask, usually made of ~80 nm thick patterned chromium metal layer deposited on a quartz plate, are held very closely or pressed against the resist-coated substrate and light of the

desired wavelength is radiated on the mask for a certain time interval. The areas of the resist below the fused silica are exposed to the light and the irradiation brings about changes in the chemical structure of the underlying resist material. In *positive*-acting resists, long polymers chains will break down into smaller components, and in *negative*-acting resists, polymer chains will crosslink on exposure to irradiation, an example of this is the very first photoresist that was produced, poly (vinylcinnamate).<sup>3</sup> The substrate is then immersed in specific solutions called ‘developer’ and the exposed areas are selectively dissolved (positive) or remain insoluble (negative) in the solution. These substrates is then ready for further processing, *e.g.* such as etching, metal deposition, *etc.*

Optical lithography is the most widely used technique in the integrated circuit (IC) industry. During the past two decades photolithography has matured and improved its capability to create very small features. However, with the ever-increasing demand for newer generation devices, the miniaturisation of device components has rapidly developed. Photolithography, due to its diffraction limits is not able to produce extremely small and densely populated features much below 50 nm; the diffraction effect from the mask opening and reflection effects within the resist degenerate the quality of the obtained structures.<sup>4</sup> Deep ultraviolet (DUV) lithography has enabled resolution to reach sub-50 nm, by employing wavelengths of 193 and 248 nm. Large-scale integrated photonic ICs are currently fabricated by DUV lithography, but the equipment required is very expensive.<sup>5</sup> Techniques like extreme ultraviolet (EUV) and X-Ray lithography have also be developed, which use even shorter wavelengths than DUV, *i.e.* 13.5 and 10’s nm (soft x-rays), respectively. However, these approaches require complex and expensive

instrumentation.

### 1.2 THE CHARGED PARTICLES LITHOGRAPHY

In order to overcome the shortcomings of photolithography, alternative lithography techniques have been developed, which use charged particles instead of photons to create patterns. Using charged particles, such as electrons, ions, or protons, allows both simultaneous patterning and imaging of a substrate. Whilst photolithography involves ‘flood-type’ exposure through a mask, direct writing can be achieved with a narrow beam of charged particles. This lithographic approach is a mask-less method, wherein desired designs are generated on computers and then directly written with the particle beam onto a substrate. The beam sequentially writes the pattern, exposing point by point at a time or one pixel per interval. A small beam size, down to 1-2 nm, can be achieved by fine focusing and adjusting the aperture through which the beam passes. Due to the nature of charged particles, unlike photolithography, diffraction issues do not interfere with patterning thus yielding sub-20 nm size features very conveniently.

The most extensively used charged particle techniques are the electron beam lithography (EBL) and ion beam lithography (IBL). As the names suggest, the beam in the EBL consists of high-energy electrons that are used to write the desired pattern, whereas in IBL they are high-energy ions. Extremely small beam sizes can be attained at the expense of increased writing times. An example of this is illustrated in section 1.3.4, where different beam sizes have affected the writing times immensely. Amongst the two, EBL, like photolithography, is a resist-base

lithography. The EBL resists are specially formulated to undergo chemical reactions once they are exposed to high-energy electrons. IBL, on the other hand, may be used both with and without resist, since ions are much heavier than electrons and can easily mill substrates like silicon (Si) or germanium (Ge), carving the desired pattern. Both techniques are thus capable of producing very small structures, since the beams can be finely focused and, in contrast to photolithography, they do not suffer from diffraction. However, as mentioned previously, expose of patterns pixel by pixel will increase writing time, especially for complex patterns with high design densities. Therefore, the throughput of EBL and IBL is low and hence, beam techniques are mainly used in research and development (R&D) as well as in small volume production and in industry for photomask fabrication.

In summary, although photolithography, in particular the DUV lithography, is still the main technique used for mass production in the semiconductor industry, EBL is becoming increasingly widespread and is the dominant nanolithography method used in academic and research environments; due to its flexibility and mask-less nature, very high (sub-10 nm) resolution as well as maturity and affordability. The following discussions will focus on EBL, as this was the technique utilised to undertake the work described in this thesis.

### 1.3 ELECTRON BEAM RESISTS

The techniques hitherto discussed, all have a common parameter without which they would be futile processes. Resists are usually polymeric materials that can be deposited on most surfaces that are subjected to patterning with photolithography or



EBL. Over the few years, many new commercial resists have emerged with the aim of improving resolution limits. In the following section new EBL resists introduced over the last 5-6 years shall be discussed in detail. Generally, a thin layer of the resist, ranging from 20-25 nm up to a micrometre is spin coated onto a substrate. The electron beam irradiates the resist in such a manner that after development the radiated portion will be eliminated (*positive tone*) or will persist (*negative tone*) on the substrate. The patterning resolution of a polymer resist depends on its chemical structure. These polymers are organic or inorganic and can be broadly classified into two types with respect to their tones, *i.e.* either positive or negative tone. Nevertheless, to achieve the best possible resolution, with both positive and negative EBL resists, requires manipulation of many parameters.

### 1.3.1 Contrast and Sensitivity

Contrast and sensitivity are the primary characterisation factors to be taken into consideration when choosing any resist. Contrast is the property of a resist to differentiate between exposed and unexposed areas. This is in turn coupled with a property known as sensitivity, which defines the extent of alteration in the resist material with respect to the electron beam dose. An electron dose is usually expressed in  $\mu\text{C}/\text{cm}^2$  and is the number of electrons/electric charge per unit area required to achieve the desired changes in a resist.<sup>6</sup> Contrast and sensitivity together give rise to a contrast curve of a resist which is obtained by simply plotting the remaining resist thickness as a function of increasing electron beam dose. The plot shown in Figure 1.1 illustrates the contrast curves for a positive and negative resist. The plot shows the decrease (positive) or increase (negative) of the remaining resist

thickness versus the exposure dose. According to the curve, the sensitivity is the dose  $D_{100}$  at which the resist is completely developed (for a positive resist) or reaches the full initial resist thickness (for a negative resist) and contrast is the slope of the curve.

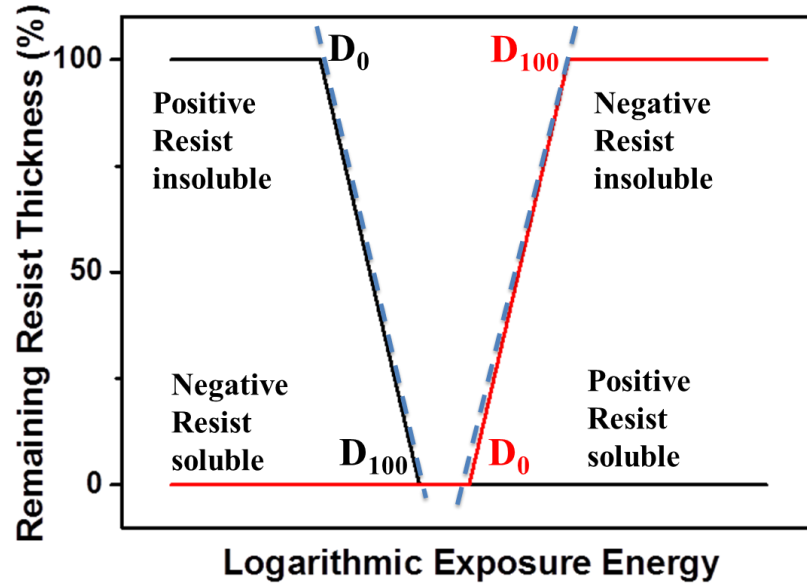


*Figure 1.1. Typical contrast-sensitivity plots for positive and negative EBL resists*

Sensitivity and contrast are inversely proportional to each other and are expressed by the equation 1.1:<sup>8</sup>

$$\gamma = \frac{1}{\log \frac{D_{100}}{D_0}}$$

(1.1)

where  $\gamma$  is the contrast value,  $D_0$  is the highest dose at which the resist is not yet affected by the electron irradiation (for a positive resist its thickness is still 100 % of

the original thickness and for a negative resist its thickness is still 0), whereas  $D_{100}$  is the minimum dose at which the resist has undergone a complete change of its chemical structure (a positive resist has been completely removed from the substrate and for a negative resist the remaining thickness is 100 % of its original thickness).<sup>9</sup> Ideally, a resist must possess a high sensitivity and contrast. In reality however, due to their inverse relationship, an increase in one parameter will result in a decline of the other and vice versa. Hence, resists are often tuned to have a good balance of both parameters. Sensitivity of a resist varies with respect to resist type, electron energy, developer solvents and development conditions. Substrate materials to be patterned also play an important role.

### 1.3.2 Developer Solvents

Other factors that govern contrast-sensitivity balance are developer solvents, developing time and temperature. Substrates, after the EBL exposure, are developed in solvents that separate the exposed from the unexposed resist. The resist-developer interdependency can immensely influence the contrast-sensitivity balance. For example, poly methylmethacrylate (PMMA) is the most well established and extensively studied EBL resist. Table 1.1 illustrates the effect on contrast, sensitivity and the surface roughness of PMMA resist having 950 K molecular weight (MW) by varying development conditions.

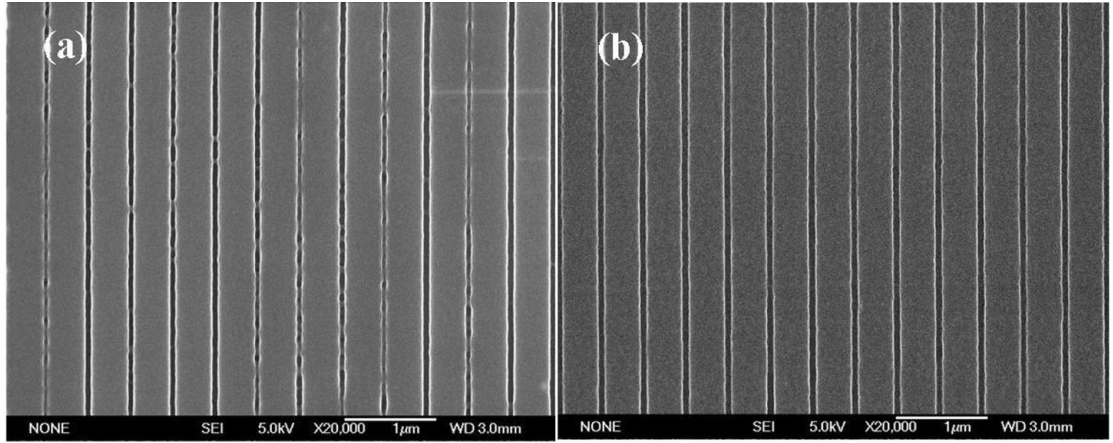
Table 1.1 shows that isopropyl alcohol (IPA) and methyl isobutyl ketone (MIBK) in a 3:1 ratio, which is the standard developer for PMMA, exhibits a higher sensitivity than pure IPA for all time intervals. Conversely, the contrast is the highest for

PMMA developed in pure IPA for 5 s and is higher than IPA:MIBK by a difference of 3.3. Moreover, surface roughness of the exposed area has also been reduced upon moving from IPA:MIBK to pure IPA. These factors impact on the lithographic performance of PMMA, as shown in Figure 1.2.

**Table 1.1.** Comparison of sensitivity, contrast and surface roughness of PMMA (MW 950 K) for different development condition.<sup>9</sup>

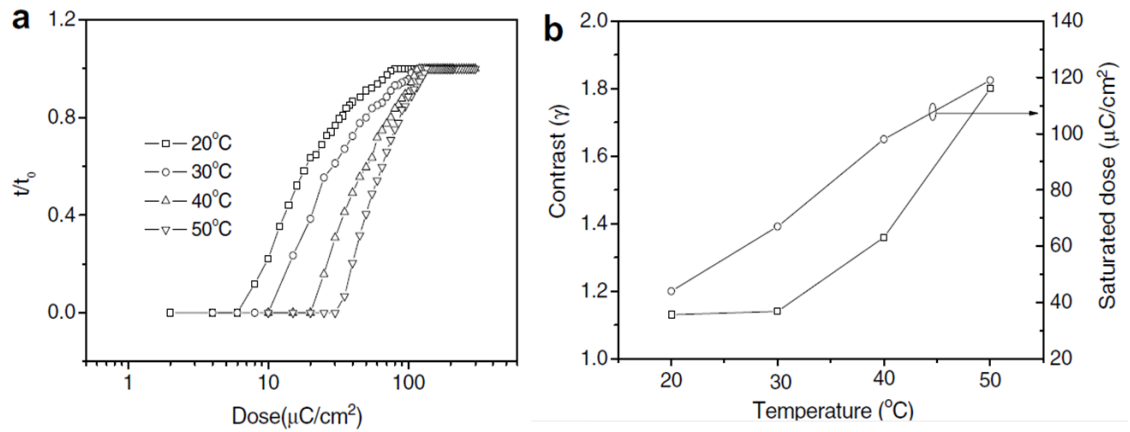
	Sensitivity ( $\mu\text{C}/\text{cm}^2$ )	Contrast	Max. RMS of surface roughness
IPA:MIBK 3:1 for 30 sec	100	4.3	4.2
IPA for 30 sec	250	6.1	5.9
IPA for 15 sec	270	7.2	4.4
IPA for 5 sec	300	7.6	3.1

Figure 1.2(a) shows that the 50 nm gratings achieved by an electron dose of  $180 \mu\text{C}/\text{cm}^2$  produces poorly defined structures when developed with IPA:MIBK. However, with pure IPA, although the sensitivity is reduced to  $750 \mu\text{C}/\text{cm}^2$ , 50 nm gratings are very well resolved. Reduced sensitivity but improved contrast is therefore achieved using IPA as a developer, as opposed to IPA:MIBK, for EBL lithography of PMMA resist.



**Figure 1.2.** Scanning electron microscopy (SEM) images of semi-dense line arrays in PMMA resist with a 50 nm linewidth. The arrays are exposed with dose of (a)  $180 \mu\text{C}/\text{cm}^2$  and (b)  $750 \mu\text{C}/\text{cm}^2$  and developed with (a) a IPA:MIBK 3:1 mixture for 30 s and (b) IPA for 5 s.<sup>9</sup>

### 1.3.3 Temperature



**Figure 1.3.** Development temperature dependence of (a) contrast curves for HSQ resist (100 kV) and (b) variation of the contrast and saturation dose with the development temperature in 2.5 % TMAH developer.<sup>10</sup>

The temperature of a developer can also affect the lithographic performance of a

resist. Hydrogen silsesquioxane (HSQ) is a negative tone EBL resist having very high (sub-5 nm) resolution, high etch resistance (chlorine chemistry) and is very stable during scanning electron microscopy (SEM) inspection. In a study on the temperature dependence of developer solutions, contrast curves for HSQ were measured at different temperatures in a 2.5 % TMAH (tetramethylammonium hydroxide) developer. The temperatures were varied from 20 to 50 °C and are presented in Figure 1.3.<sup>10</sup>

Figure 1.3 shows that the temperature of the developer has a considerable effect on the contrast-sensitivity of HSQ resist. As the temperature is raised from room temperature (20° C) to 50° C, the contrast is improved but at the cost of reduced sensitivity. The main reason for this is that warm developers are more effective in dissolving the resist molecules than the cold ones. Therefore, at room temperature the developer is not able to dissolve the resist areas that are partially exposed by forward- and backscattered electrons (only partially cross-linked), leading to good sensitivity (less primary dose necessary to form a resist structure remaining on the substrate) but poor contrast. At elevated temperatures, however, the partially exposed resist is completely dissolved, which results in lower sensitivity (more primary dose necessary to form a resist structure remaining on the substrate) but higher contrast (better differentiation between exposed and unexposed or partially exposed resist).

In the case of a positive resist, the opposite effect is observed, *i.e.* cooler developer solutions have shown to improve the contrast immensely, however negatively affecting the sensitivity.<sup>11</sup> Here the reason for this behaviour is again the same as

with the negative resists but working in the opposite direction, since the electron exposure dissociates the molecular bonds in positive resists, causing scission of molecules, whereas it cross-links the molecular bonds in negative resists, causing networking of molecules. Therefore, at room temperature the developer is able to dissolve the partially exposed positive resist, leading to good sensitivity (less primary dose necessary to remove the resist from the substrate) but poor contrast. At low temperatures, however, the partially exposed positive resist is not dissolved by the developer, which results in lower sensitivity but higher contrast. Figure 1.4 illustrates the contrast curves of the positive resist SML at different voltages developed in a 7:3 ratio of IPA:water. Two developer temperatures were employed, *i.e.* room temperature and 0 °C. The plot shows that the sensitivity of the resist developed at 0 °C is reduced by 4 times compared to room temperature and the contrast is moderately increased (by approximately 1.6 times).

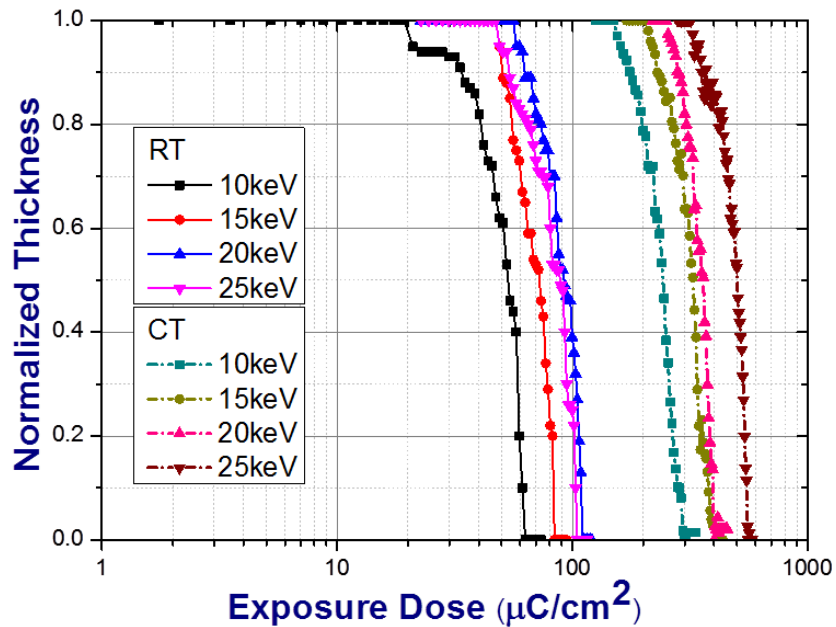


**Figure 1.4.** Contrast curves of SML 50 developed in a 7:3 ratio of IPA:water developer at cold temperature (0 °C) and at room temperature.<sup>11</sup>

### 1.3.4 Auxiliary Factors

In this section other factors that contribute to resist profiling are briefly discussed. Technical restrictions arising from a particular lithography tool also contributes to the resolution of the resist. EBL systems are usually designed with voltages from 1 to 30 kV, for converted SEMs, and from 25 to 100 kV for dedicated beam systems. The sensitivity and resolution of a resist depends largely on the energy of the electron beam. For any resist, the sensitivity decreases when higher voltages are employed whereas the contrast (resolution) improves. The main reason for this is that slow electrons interact more readily with solids and hence they expose the resist much more efficiently than fast electrons. Therefore, resists are more sensitive to irradiation with low-energy electrons than with high-energy electrons. Since the electrons are light particles, they are easily scattered in solids. Therefore, when a resist is exposed to an electron beam, it is irradiated by the primary electrons on their first passage through the resist (forward scattered electrons) as well as by electrons that have already reached the substrate and are scattered back into the resist (backscattered electrons).<sup>12</sup> In addition, secondary electrons generated by both forward and backscattered electrons also irradiate the resist. These phenomena leads to the fact that the resist is exposed not only in the intended areas but also in wide adjacent regions, causing a distortion of the designed pattern known as a "proximity effect".<sup>13</sup> At low voltages, *e.g.* 10 kV or less, forward scattering is high, causing significant widening of the electron beam. In addition, backscattered electrons have a short range and are confined around the point of incidence of the electron beam causing substantial exposure of the resist. Therefore, at low electron energies the



proximity effect is relatively high and may lead to considerable distortion of the exposed pattern. Conversely, when a high voltage, *e.g.* 100 kV, is employed the forward scattering is reduced. The back scattering area gets deeper and wider and the backscattered electrons lose a significant part of their energy before again reaching the resist.<sup>12</sup> Therefore, although spread over a large area, the backscattered exposure has a relatively low intensity and appears as a weak background exposure. As a result, at high electron energies the proximity effect is relatively less pronounced than at low electron energies and the exposed pattern is usually closer to the original design.

Thus, for low resolution and large structures, *i.e.* micron sizes and above, low voltage beams can be used to reduce the exposure time. However, for critical high-resolution patterns requiring also high precision, high voltages are needed. For instance, Figure 1.5 illustrates a germanium-on-insulator (GeOI) test device structure patterned to measure the resistance across a nanowire having a width of 20 nm. This device was fabricated at two different exposures; the nanowires were fabricated at 10 kV whereas the contact pads were exposed at 1 keV. At 10 kV the writing time for the large contact pads would have been approximately 15 minutes, however due to the lower voltage used the write time was reduced to 1 minute.

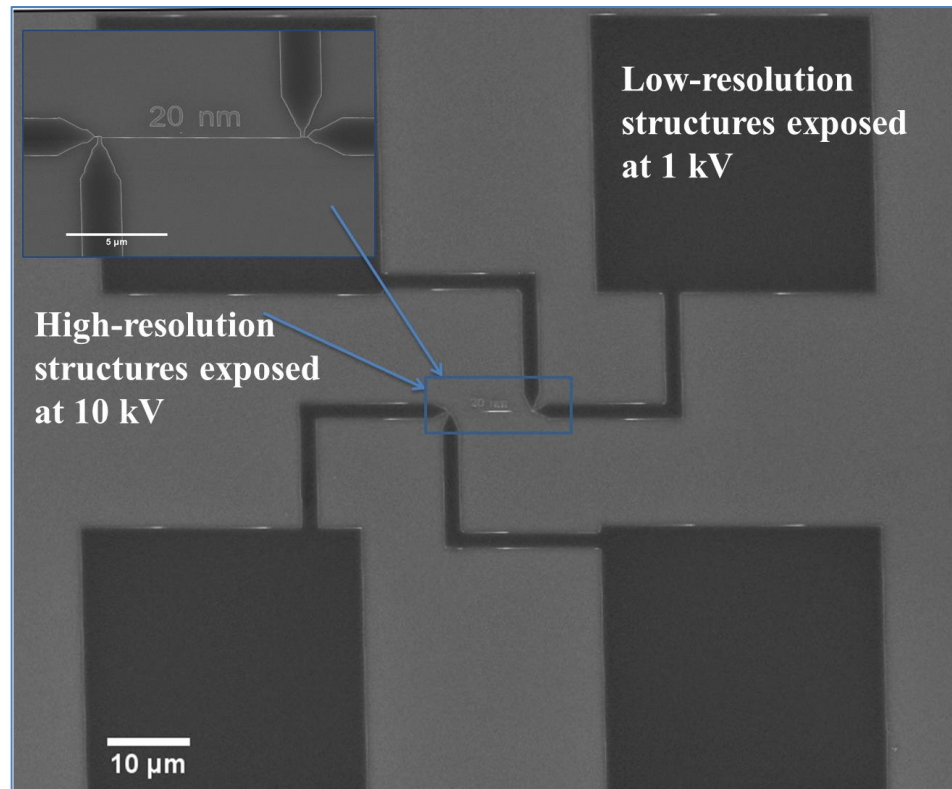


**Figure 1.5.** SEM micrograph of a test device on germanium on insulator for measuring the resistance across a 20 nm wide nanowire

## 1.4 EBL RESIST FAMILIES

EBL is a direct-write process and due to the lightweight nature of the electrons, the beam cannot engrave typically used substrate materials. Resists are thus an integral part of an EBL process. The resist pattern produces a stencil on the substrate, which can be transferred into the substrate with further fabrication processes. Over the years, many new resists have been formulated to fulfil various nanofabrication demands. Traditional resists like PMMA, ZEP and HSQ are the most commonly used due to their superior lithographic outputs. This section will highlight new classes of EBL resists that have been introduced during the past 5-6 years.

While defining electron resists, the aforementioned words PMMA, ZEP and HSQ appear regularly in the literature. Most of the literature reports on resists, irrespective of resist tones, often consider these resists as standard for resolution comparison with new resists.<sup>6,10,11,14</sup> HSQ (Dow Corning) is the resist that has by far, provided the highest resolution EBL structures down to sub-5 nm.<sup>15</sup> HSQ is an inorganic material belonging to the spherosiloxane family, with a low dielectric constant (2.8).<sup>16</sup> HSQ's high-resolution capability, ease of imaging post-exposure and etch resistance are its prominent features. However, the resist suffers from several drawbacks, such as a very limited shelf life of up to 6 months and a necessity to be store at a temperature below 5 °C, thus requiring a high standard of maintenance. HSQ is extremely sensitive to moisture, hence the interval between spin casting and exposure must be as minimum as possible to avoid unsolicited crosslinking of polymer molecules. From the lithography point of view, the resist suffers a relatively low sensitivity, *e.g.* an electron dose of between 900-1000  $\mu\text{C}/\text{cm}^2$  is required to generate a 50 nm wide line at 10 kV, which eventually increases the writing time in comparison with PMMA ( $\sim 330 \mu\text{C}/\text{cm}^2$ ) and especially ZEP ( $\sim 120 \mu\text{C}/\text{cm}^2$ ). Thus, even though HSQ exhibits commendable lithographic qualities, it is still a difficult resist to handle.

PMMA is a well-established positive resist having a good balance of sensitivity, contrast and roughness. PMMA is by far the most widely utilised EBL resist. PMMA with different molecular weights can be used in various applications involving EBL fabrication. Sub-10 nm resolution structures have been demonstrated with PMMA using high beam voltages and cold temperature developments, thus

requiring higher e-beam doses.<sup>17</sup> The positive resist ZEP was developed at the end of 1980's.<sup>18</sup> And initial studies showed its commendable resolution, better etch durability and sensitivity improvement (one order of magnitude) in comparison to PMMA.<sup>19</sup> However, over the last couple of years the commercial value of ZEP has risen by tenfold in Europe: a litre currently costs approximately €7000 compared to €200 for PMMA.<sup>20</sup>

Many new resists have emerged in the past few years. Other than their lithographic perspectives, aspects such as cost, shelf life, perilousness and compatibility with industrial semiconductor processes need to be taken into account. Resists are broadly classified into two divisions, positive and negative, depending on their reaction upon e-beam radiation. However, based on their chemical structures, they can be further classified into families, irrespective of their tones.

### 1.4.1 Chemically Amplified Resists (CARS)

A family of resists known as chemically amplified resists (CARS) emerged in the 1980s as powerful lithographic materials due to their supreme sensitivity and resolution.<sup>21,22</sup> These resists were initially proposed and developed by IBM as photoresists but are now also regularly used for EBL.<sup>22</sup> They are basically a blend of an acid reactive polymer, such as an epoxy group based polymer, and a photo-acid generator (PAG).<sup>23,24</sup> They are also formulated in two tones of the resists. Upon electron irradiation, the photo-acid is released which catalyses further reactions without an additional electron dose, thus enhancing sensitivity. The substrate is then baked after exposure in order to the released the photo-acid and to catalyse the resist

matrix.<sup>6</sup> However, as device miniaturisation has continued, several factors have affected the resolution of CARS. Firstly, the non-uniform acid diffusion and migration within the resist film during post-exposure baking limits the critical resolution of CARS.<sup>25,26</sup> Secondly, as a result of acid diffusion, roughness in patterned structures arises. Thus, controlling acid diffusion is a priority to acquire high-resolution feature sizes from CARS. One of the methods used to overcome this problem was to bond a PAG unit to the polymer sidechain, rather than blending the PAG with the polymer.<sup>26</sup> Thus, several polymer-bound PAG CARS resists have been developed over the last few years.

Polymer-bound PAG resists are therefore usually a merger of complex polymers. Recently, such a negative tone CAR comprising of glycidyl methacrylate (GMA), methyl methacrylate (MMA) and triphenylsulfonium salts methacrylate (TPSMA) was developed for EBL and was compared with a polymer blended PAG CARS for sensitivity and contrast.<sup>27</sup> Firstly, the two polymers were polymerised together to give the product poly (GMA-co-MMA) which was further polymerised with the PAG to give poly (GMA-co-MMA-co-TPSMA) powder (Avg. Mol. wt. = 23,800 g/mol). The resist solution was prepared by dissolving the powder in dimethylformamide (DMF) or propylene glycol monomethyl ether acetate (PGMEA). Their sensitivity, lithographic performance and etch resistance were evaluated in the study. The contrast curve of the first CAR revealed a sensitivity of  $300 \mu\text{C}/\text{cm}^2$  without any post-exposure bake. The sensitivity of the second polymer blend, poly (GMA-co-MMA) with TPSMA, was measured as  $125 \mu\text{C}/\text{cm}^2$  without post-exposure bake, which further reduced to  $70 \mu\text{C}/\text{cm}^2$  by post-exposure baking at

80 °C for 60 s. The resists were developed in a mild 7:3 ratio of IPA:water developer solution for 1 min followed by rinsing in deionised (DI) water. The smallest feature size that was acquired from the resist was a 15 nm line with a 1:15 pitch size, as illustrated in Figure 1.6(a). Dense grating of 20 nm lines using a 1:1 pitch size was also obtained and shown in Figure 1.6(b). However, post-exposure bake accelerated acid diffusion in the resist, thus unfavourably affecting the line edge roughness (LER), as shown in Figure 1.6 (c). The post-exposure bake can however be excluded hence, cutting down a process step at the expense of lower sensitivity.

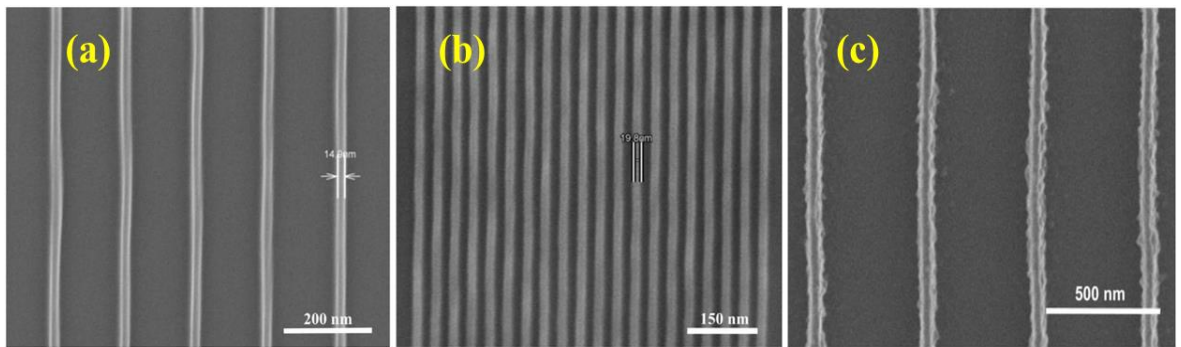


**Figure 1.6.** SEM images of gratings produced using the negative tone poly (GMA-co-MMA-co-TPSMA) resist: (a) 14 nm grating with a 1:15 pitch, (b) dense gratings with a 19 nm linewidth in 1:1 pitch and (c) gratings with post-exposure bake at 80 °C for 60 s.<sup>27</sup>

Positive tone CARS have also been employed and a chemically amplified (CA) photoresist recently used for EBL is 40TX. Such resists, when employed alone, produced an almost insoluble top layer due to the reaction between photo-acid evaporation and basic air contaminants.<sup>28,29</sup> Therefore, in a study a protective coat

was spun on the CA resist which was comprised of acidic poly (3,4-ethylenedioxythiophene) poly(styrene-sulfonate) (PEDOT:PSS). Contrast curves were generated for the resist at 20 kV using the standard developer AZ® 726MIF in various dilutions with DI water. The high sensitivity range of this resist lies between 7-10  $\mu\text{C}/\text{cm}^2$  and the contrast varies from 7-14. The effects of various developer dilutions on contrast-sensitivity values are given in Table 1.2. The critical dimension (CD) of the resist in this study was measured after the complete lift-off process, hence the CD values were between 80 to 110 nm as shown in Table 1.2. Gold nano-gratings, approximately 90 nm in width and 70 nm apart, were fabricated using this resist, as illustrated in the SEM image shown in Figure 1.7. The purpose of the study was to fabricate robust structures with this CAR, as there were no significant linewidth or sensitivity variations observed even when the samples were stored for 24 h in vacuum or air.<sup>30</sup>

**Table 1.2.** Contrast and sensitivity values of 40XT positive CARS for different development parameters.<sup>30</sup>

Developer dilution [% vol. DI water]	Development time [s]	Contrast ( $\gamma$ )	Sensitivity ( $D_C$ ) [ $\mu\text{C}/\text{cm}^2$ ]	Critical dimension (CD) [nm]
0%	5	$8 \pm 2$	8	$95 \pm 10$
0%	10	$7 \pm 0.5$	7	$110 \pm 5$
33%	20	$14 \pm 2$	10.5	no undercut
33%	40	$10 \pm 0.5$	9	$85 \pm 5$
33%	60	$9 \pm 0.5$	8	$85 \pm 5$
40%	60	$11 \pm 0.3$	9	$80 \pm 5$
40%	120	$10 \pm 0.3$	7.5	$80 \pm 5$

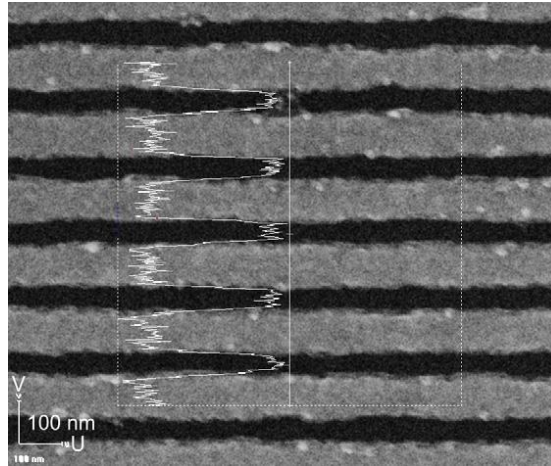


**Figure 1.7.** Line and space pattern: 90 nm wide gold lines on a  $\text{SiO}_2$  substrate spaced 70 nm apart (80 nm half-pitch), structured with the after lift-off process. The sample was developed for 60 s in a developer diluted with 40 % vol. DI water.<sup>30</sup>

#### 1.4.2 Non-CARS

Whilst CARS have demonstrated extremely high sensitivity, the LER and line width roughness (LWR) constrains the sub-20 nm feature size, as acid diffusion in the resist is uncontrolled.<sup>31</sup> To counter this effect, advanced classes of resists are being formulated which are sensitive directly to radiation.<sup>32</sup> In order to increase the irradiation sensitivity, a radiation sensitive group must be incorporated into the polymer unit. Such resists are known as non-chemically amplified resists (n-CARS). Sulphonium salts have been known to be sensitive to UV and electron beam radiations and can be incorporated into polymer units.<sup>33</sup> In a recent study, a copolymer of (4-(methacryloyloxy) phenyl) dimethylsulfonium triflate (MAPDST), the radiation sensitive group, and methyl methacrylate (MMA) was synthesised (MAPDST-MMA).<sup>34</sup> This copolymer was dissolved in methanol to give a negative tone resist solution. The copolymer resist coated substrates were exposed at 20 kV



and were subjected to post-exposure bake at 100 °C for 120 s, followed by development in a 0.022 N TMAH solution. The customary characteristics of this resist were evaluated. The exceptionally high sensitivity of  $2.06 \mu\text{C}/\text{cm}^2$  was observed with a contrast of 1.8, which can be seen in the contrast curves shown in Figures 1.8(a). In Figure 1.8(b), the highest resolution lines of 20 nm width, with 100 nm spacing, are illustrated. These lines were obtained at a dose as low as  $40 \mu\text{C}/\text{cm}^2$ , in contrast to the popular negative HSQ resist which requires a dose close to  $2000 \mu\text{C}/\text{cm}^2$  to pattern lines of similar width and spacing. The gratings also exhibited a reasonable LER of between 1.8 to 2.2 nm.

Hence, the addition of a sulphonium group to the polymer unit enhances the sensitivity of the resist tremendously. Structures as fine as 20 nm could be easily resolved with this resist. Thus, the resist is a good candidate for future high resolution EBL due to its high sensitivity and contrast and ability to generate low LER structures.

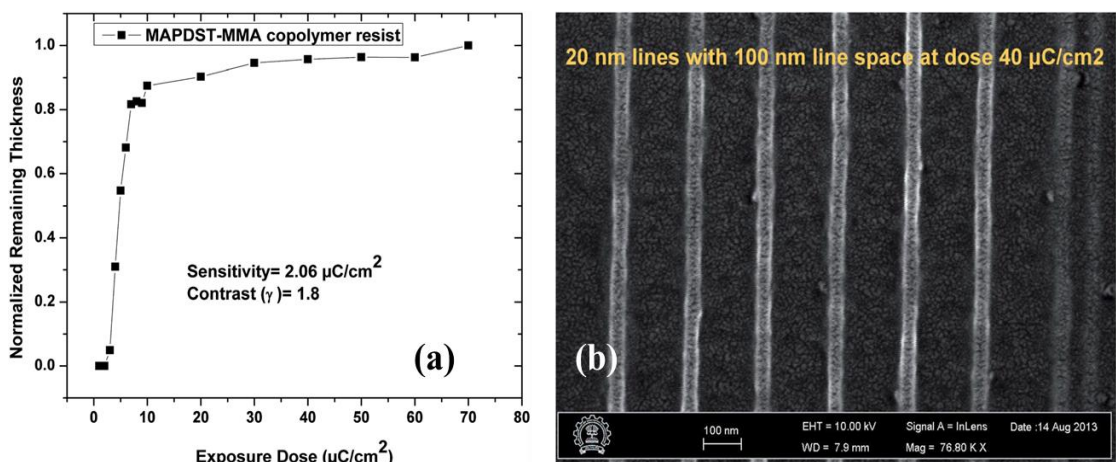


**Figure 1.8.** (a) Contrast curve of MAPDST-MMA copolymer negative resist, (b) SEM image of the e-beam patterning of the negative tone copolymer resist for

*isolated 20 nm line patterns with 100 nm space; patterns exposed at a dose of 40  $\mu\text{C}/\text{cm}^2$ .*<sup>34</sup>

### 1.4.3 Fullerene Derivatives Resists

Buckminsterfullerene (hence after referred as fullerene),  $\text{C}_{60}$ , is an allotrope of carbon containing 60 C-atoms to form a spherically shaped unit. Fullerene's potential as a negative tone EBL resist was first recognised by Tada *et al.* due to its reactivity towards UV light.<sup>35</sup>  $\text{C}_{60}$  has small diameter, of around 0.7 nm, making it ideal for high-resolution lithography.<sup>36</sup> Tada *et al.* showed that electron beam irradiation caused the solubility of a  $\text{C}_{60}$  film to reduce in a toluene developer, thus allowing it to be used as a negative-tone resist.<sup>35</sup> However,  $\text{C}_{60}$  has a very low sensitivity of about 12  $\text{mC}/\text{cm}^2$  and requires preparation via vacuum sublimation.<sup>37</sup> Nevertheless, in the last few years, new types of polymer-bound fullerene derivative resists, which can be spin coated onto substrates, have been fabricated. Two such resists,  $\text{C}_{60}$ -containing poly (p-tert-butoxystyrene) and  $\text{C}_{60}$ -containing poly (p-tert-butoxycarbonyloxystyrene), have been developed for photolithography.<sup>38</sup> In the case of EBL resists, two of the fullerene derivatives developed in recent years, with different polymer chains shall be discussed in the section below.

The first study involved the blending of two polymers, poly (p-chloromethylstyrene) (PCMS) and poly (hydrostyrene) (PHS), in which the  $\text{C}_{60}$  moiety was incorporated.<sup>39</sup> The main motive behind using the PCMS polymer was because it exhibits a high electron sensitivity, whereas  $\text{C}_{60}$  alone has a tremendously low sensitivity of approximately  $10^4 \mu\text{C}/\text{cm}^2$ .<sup>40,35</sup> The use of PHS was because the hydroxyl group

aids in the adhesion of the C<sub>60</sub> derivative resist to a substrate. Various blends of the three unities consisting of different weight fraction of C<sub>60</sub> have been produced, as shown in Table 1.3.

**Table 1.3.** *Blends of PCMS and PHS polymers consisting of different weight fraction of C<sub>60</sub> for preparing resists.*<sup>40</sup>

Code	Yield (%)	$M_n$ calcd <sup>d</sup>	Wt. fract. of C <sub>60</sub> (wt%)	$T_g$ (°C)
C <sub>60</sub> -(PCMS) <sub>2</sub>			7.6	90
C <sub>60</sub> -(P(CMS <sub>46</sub> -HS)) <sub>2</sub>	89	7,700	9.4	>130
C <sub>60</sub> -(P(CMS <sub>31</sub> -HS)) <sub>2</sub>	96	7,500	9.6	>130
C <sub>60</sub> -(P(CMS <sub>14</sub> -HS)) <sub>2</sub>	95	7,900	9.1	>130
C <sub>60</sub> -(PHS) <sub>2</sub>	94	5,400	13	>130

The resist-coated substrates were exposed at 100 kV and developed with toluene or acetone to evaluate their lithographic performance. Figure 1.9 illustrates the reaction mechanism of a C<sub>60</sub> derivative resist upon electron beam radiation. The C<sub>60</sub> derivative shown in Figure 1.9 is coded as C<sub>60</sub>-(P(CMS<sub>*x*</sub>-HS))<sub>2</sub> where *x* = 14, 31 or 46, thus varying the weight fraction of C<sub>60</sub>, according to Table 1.3. The developer used was acetone however strong aggregations of C<sub>60</sub> moieties were found, which resulted into swelling and deformation of the structures. Figure 1.10 shows a SEM image of 50 nm gratings, the minimum resolution obtained with C<sub>60</sub>-(P(CMS<sub>14</sub>-HS))<sub>2</sub>, at a dose of 286 μC/cm<sup>2</sup> and a LER of ~7 nm.

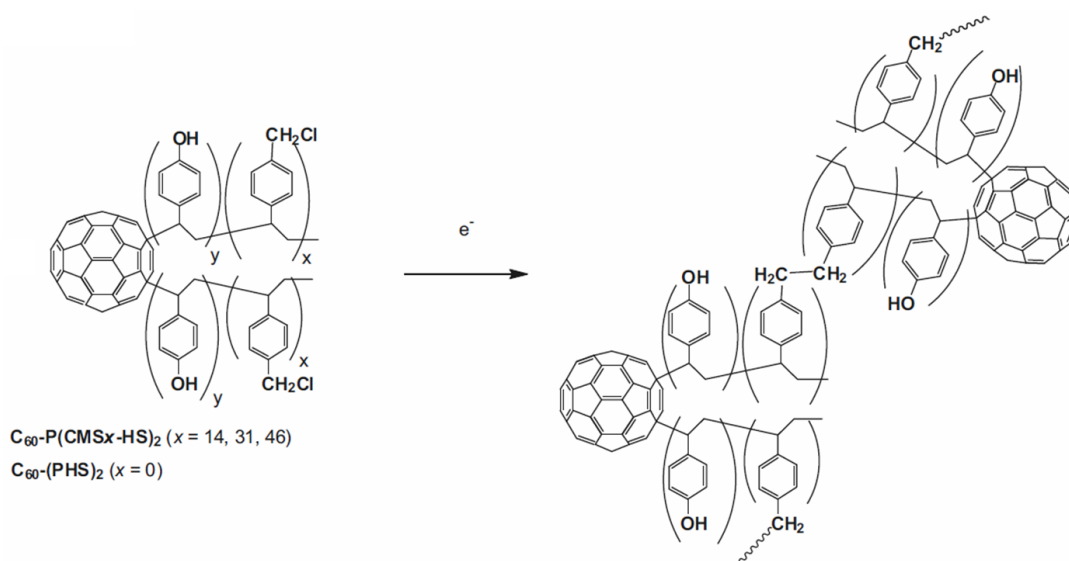


**Figure 1.9.** Crosslinking of the  $C_{60}$  derivative upon electron beam radiation.<sup>40</sup>

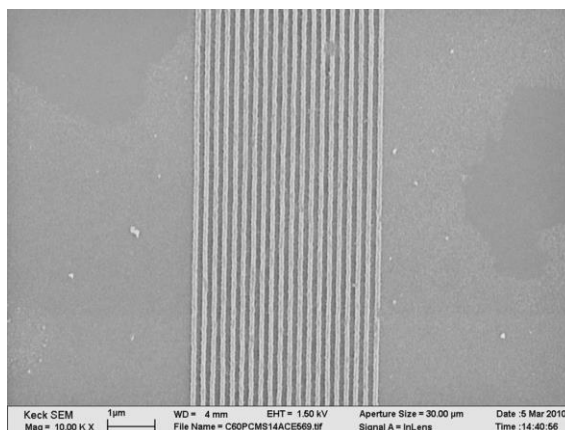


**Figure 1.10.** SEM image obtained after EB exposure using  $C_{60}\text{-(P(CMS}_{14}\text{-HS))}_2$ , at a dose of  $286 \mu\text{C}/\text{cm}^2$  and developed in acetone for 10 s.<sup>40</sup>

The  $C_{60}\text{-(P(CMS}_{14}\text{-HS))}_2$  resist gave the best result in terms of resolutions amongst the other compositions given in Table 1.3. Hence, it was concluded that  $C_{60}$  could be utilised as negative tone EBL resists. The sensitivity of the  $C_{60}$  moiety was reduced by 3 orders of magnitude with the addition of the copolymers, achieving high-resolution structures down to 50 nm in each case.

In the second recent study, three phenol-based fullerene negative tone resists have been presented for next generation electron beam lithography.<sup>41</sup> Not only was the resist a fullerene derivate, but also a CAR consisting of a crosslinker and a PAG component. The first fullerene derivative prepared consisted of phenolic methanofullerene (IM-MFP12-3). The other two resists consisted of tertiary butoxycarbonyl (tBOC) protecting groups, however they differed in that one had a longer side chain (IM-MFP12-8) than the other (IM-MFP12-2). The resists were prepared by dissolving the fullerene derivative, epoxy crosslinker and triphenylsulphonium hexafluoroantimonate PAG in propylene glycol monomethyl ether (PGME), with a 10-20 g/L concentration. They were then mixed in one part fullerene derivative, two parts crosslinker and one part of the PAG and spin-coated onto Si substrates. The chemical structure of the three fullerene derivatives along with their contrast curves can be seen in Figure 1.11.

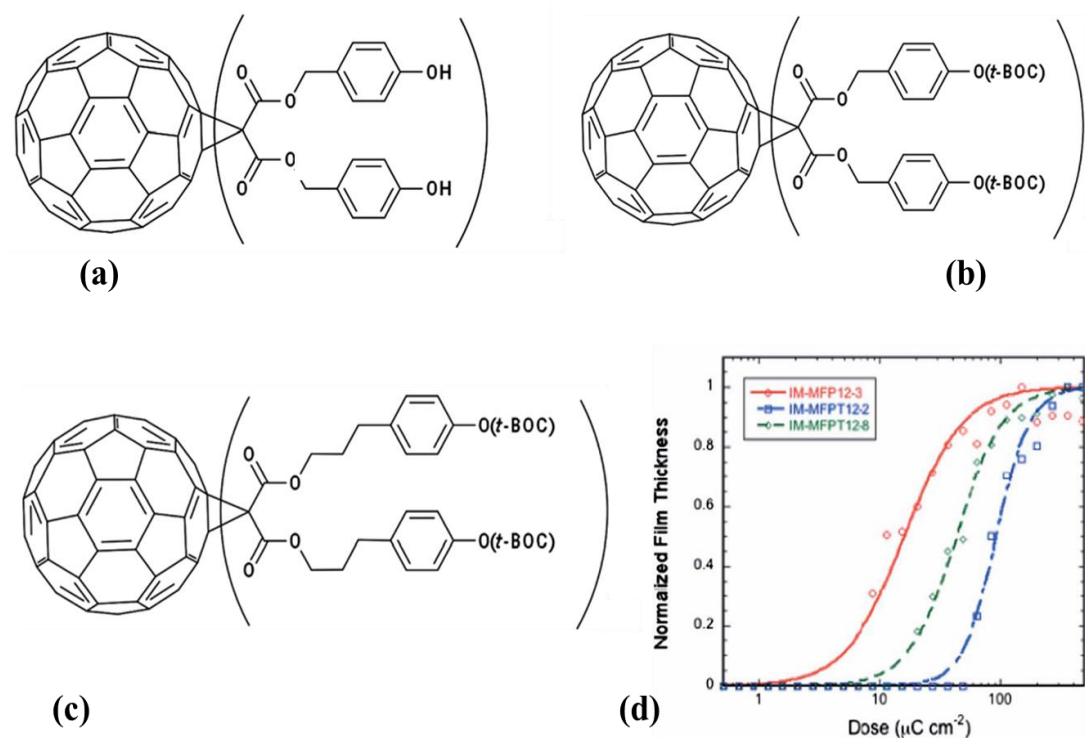


**Figure 1.11** Chemical structures of (a) (3-phenol-1-propyl malonate)-methano-[60] fullerene, (b) (t-butoxycarbonyl malonate)-methano-[60] fullerene and (c) [3-(4-butoxycarbonyl) phenyl-1-propyl malonate]-methano-[60] fullerene and (d) contrast curves for the three resist derivatives.<sup>41</sup>

The Si substrates were post-exposure baked at 90 °C followed by dip development in 1:1 monochlorobenzene (MBC) and IPA. Figure 1.11(d) shows the calculated contrast curves of the three resists and their sensitivity (contrast in brackets): 93  $\mu\text{C}/\text{cm}^2$  (1.8), 43  $\mu\text{C}/\text{cm}^2$  (1.3) and 32  $\mu\text{C}/\text{cm}^2$  (1.0) for IM-MFP12-2, 3 IM-MFP12-8 and IM-MFP12-3, respectively. Thus the enhanced sensitivity, amongst the tBOC-protected material, of IM-MFP12-8 was attributed to the higher flexibility of longer polymer chains helping to improve crosslinking. Long chains have previously been reported to enhance acid diffusion, which is evident in this study.<sup>42</sup>

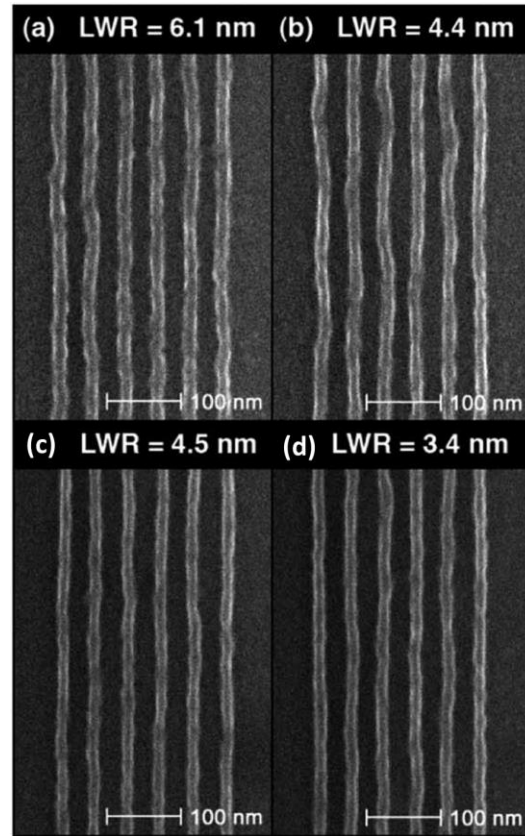


**Figure 1.12.** SEM images of dense single pixel features of IM-MFP12-8 resist, with the top row developed without post-exposure bake and the bottom row with 90 °C post-exposure bake. The pitches are 48 nm for (a) and (c); and 46 nm for (b) and (d) with their corresponding LWR.<sup>41</sup>

Figure 1.12 illustrates the SEM images of single pixel gratings exposed on IM-MFP12-8 resist developed with 1:1 MBC:IPA. The linewidth observed for the gratings lies between 13-15 nm; exposed at 30 kV within a dose range of between 240-350 pC/cm<sup>2</sup>. From the SEM images shown in Figure 1.12, LWR is higher for exposures developed without the post-exposure bake, thus indicating the requirement of post-exposure bake for the complete development of partially exposed resists for smoothing the LWR. A new negative phenol-based fullerene resist was conclusively presented in this study. The resist offered high sensitivity as well as a high resolution

at low exposure doses as compared to the traditional high resolution HSQ resist.

A positive tone fullerene derivate resist containing the acid labile groups tert-butyl acetate (tBAC) and (tBOC), has also been reported in literature.<sup>43</sup> The sensitivity of the resist was found to lie in the range of 100-150  $\mu\text{C}/\text{cm}^2$  and isolated lines as small as 20 nm were successfully patterned. Thus, fullerene comprising materials have emerged as a new high-resolution class of resists.

### 1.4.4 Methacrylate Bases Resists

PMMA was the first resist of the methacrylate family and also the earliest EBL resist to be developed.<sup>44</sup> This family of resists consist of a methacrylate backbone ( $\text{CH}_2\text{CHCO}_2\text{CH}_3$ ) and are usually used as positive resists, however upon elevating the electron dose the resists can also behave as negative tone resists. PMMA is still regarded as the standard high-resolution resist and is the most widely used EBL resist. Lines as small as sub-5 nm have been resolved in PMMA by cold temperature development.<sup>45</sup> The other renowned resist of the same family is ZEP, which is a 1:1 copolymer of  $\alpha$ -chloro methacrylate and methyl styrene. The high sensitivity and etch durability, as well as the stability of this resist are prominent.<sup>14,46</sup> Both the resists mentioned can be commonly developed in organic solvents such as MIBK, xylene based, amyl acetate, hexyle acetates and IPA. Methacrylate-based resists offer good lithographic outcomes with ease of handling and hence both compounds have established themselves as mainstay electron beam resists.

During the last 5 years, two new resists with a methacrylate backbone have been



reported: SML (EM Resist Ltd. United Kingdom) and chemically semi-amplified resist 62 (CSAR 62) (Allresist GmbH, Germany). The complete chemical structures of both these resists have withheld, however the presence of a methacrylate group in SML and CSAR 62 has been reported.<sup>11,47</sup> Further details of the SML is presented in depth in Chapter 3 of this thesis. CSAR 62 is a CAR consisting of the copolymer of  $\alpha$ -chloro methacrylate and methyl styrene in anisole, much like ZEP. However, unlike ZEP this resist includes additives to enhance its sensitivity, hence semi-chemically amplified.<sup>47</sup> In a very initial study of CSAR 62, its parameters have been compared with those of ZEP and PMMA resists. For the contrast-sensitivity measurement, CSAR was developed using amyl acetate, which is the standard ZED N50 developer of a ZEP resist, o-xylene as well as using a combination of both solvents. The contrast curves plots generated at 100 kV under various conditions are illustrated in Figure 1.13.

Developing CSAR 62 with amyl acetate gave the highest contrast value of 5.2, as seen in Figure 1.13(b), however a large amount of resist residues were observed even after the clearance dose. On the other hand, the use of o-xylene developer reduced the residues but at the expense of contrast. The o-xylene dip after developing in amyl acetate gave a contrast ( $\gamma$ ) and sensitivity ( $S$ ) very similar to that of ZEP resist ( $\gamma_{\text{ZEP}} = 4.18$ ,  $S_{\text{ZEP}} = 180\mu\text{C}/\text{cm}^2$  and  $\gamma_{\text{CSAR62}} = 4.77$ ,  $S_{\text{CSAR62}} = 172\mu\text{C}/\text{cm}^2$ ). The ultimate resolution of this resist was presented by another group using a 180 nm thick CSAR 62 resist where lines approximately 10 nm wide were resolved with a pitch of 100 nm, as evident in Figure 1.14.<sup>48</sup>

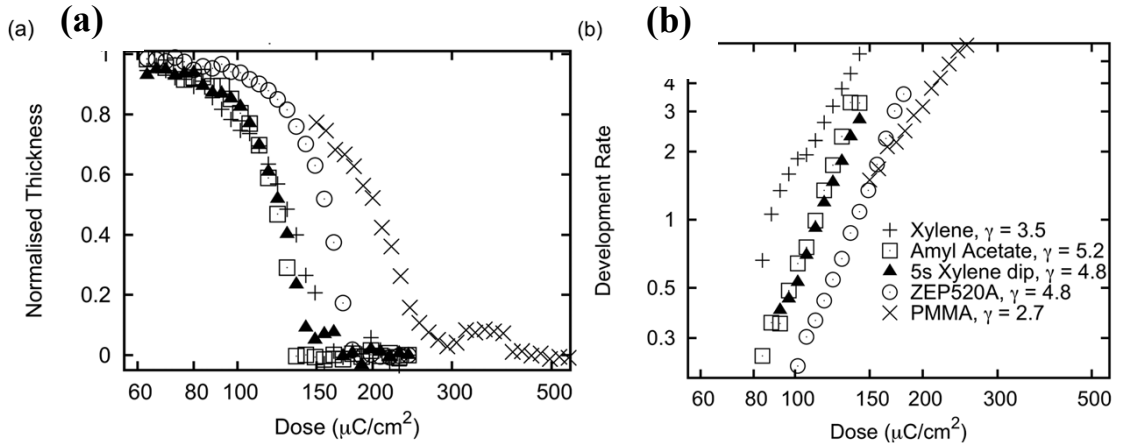


**Figure 1.13.** Contrast plots for (+) CSAR 62 developed using *o*-xylene, ( $\square$ ) CSAR 62 developed using amyl acetate, ( $\blacktriangle$ ) CSAR 62 developed using amyl acetate followed by a 5 s dip in *o*-xylene, ( $\circ$ ) ZEP520A, and ( $\times$ ) PMMA. (a) The normalised remaining resist thickness vs log dose, (b) log development rate plotted against log dose. The contrast,  $\gamma$ , for each resist is also shown.<sup>47</sup>

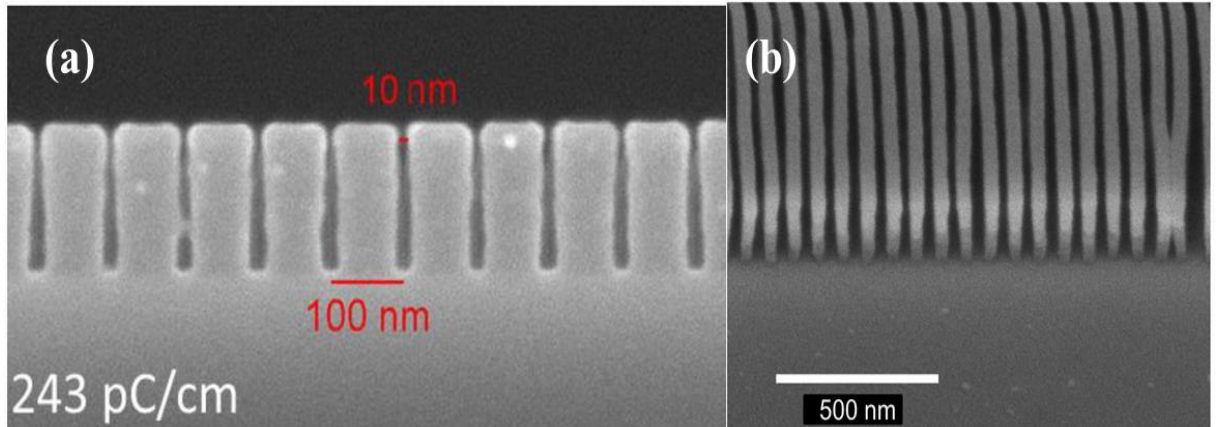


**Figure 1.14.** SEM images showing (a) the critical resolution of a 180 nm thick CSAR 62 resist, (b) 200 nm thick CSAR 62 resist image showing 75 nm period lines, some of which show signs of collapse.<sup>48</sup>

### 1.4.5 Inorganic Resists

In comparison to organic resists, inorganic resists generally possess higher contrast and better etch resistance due to their chemical structure, but invariably suffer a reduced sensitivity. The most efficient resist, which has staunchly maintained its high performance, is HSQ. HSQ is the smallest member of the polyhedral oligosilsesquioxane (POSS, trademarked by Hybrid Plastics) family, and has a cubic structure ( $\text{HSiO}_{3/2}$ ).<sup>49</sup> On electron beam exposure, the cubic HSQ molecules cross-link forming network structures.<sup>50</sup> HSQ has demonstrated a linewidth resolution of 7 nm, with a pitch size of 14 nm, at a dose of nearly 1 nC/cm (30 kV).<sup>51</sup> 6 nm isolated lines and 7-nm dense lines at doses of 5.5 and 33 mC/cm<sup>2</sup> respectively, have also been reported previously.<sup>52</sup> Nevertheless, due to its sensitivity issues and short shelf-life, HSQ is often troublesome to work with. Nevertheless, newer inorganic resists with silsesquioxane moieties and others containing metal fragments have emerged.

In 2007 two negative, inorganic resists constituting of hafnium and zirconium oxide sulphates, known as  $\text{HfSO}_x$  and  $\text{ZircSO}_x$  respectively, were reported.<sup>53</sup> Resist solutions were prepared by combining  $\text{HfOCl}_2(\text{aq})$  or  $\text{ZrOCl}_2(\text{aq})$  with a mixture of  $\text{H}_2\text{SO}_4$ ,  $\text{H}_2\text{O}_2$  and 18 M $\Omega$  purified water to give metal: sulphate ratios of 1: 0.5 and 0.7. The resists were spin-coated onto Si to achieve 35 nm thin films. The contrast curves and high-resolution performance of the resists were evaluated using 30 kV. Figure 1.15 presents the contrasts curves of the two metal sulphate resist developed with TMAH ( $\text{HfOCl}_2 = 90$  s and  $\text{ZrOCl}_2 = 240$  s). Figure 1.15(a) shows the contrast curves for  $\text{HfSO}_x$  and  $\text{ZircSO}_x$  having a metal: sulphate ratio of 1: 0.55 and 1: 0.5,

respectively. The sensitivity of  $\text{HafSO}_x$  was determined to be  $21 \mu\text{C}/\text{cm}^2$  with a contrast of 2.5, whereas that of  $\text{ZircSO}_x$  was a remarkable  $7.6 \mu\text{C}/\text{cm}^2$  with a contrast of 2.6. For an inorganic resist with no chemical amplification the sensitivity of both the resists is praiseworthy. Figure 1.15(b) shows a contrast-sensitivity plot of  $\text{ZircSO}_x$  having a metal: sulphate ratio of 1: 0.7. The sensitivity can be observed to decrease by a factor of 36 relative to its lower sulphate formulation, but with an improving contrast value up to 5.2. In this study the sensitivity of resist was correlated to the electron density of the material. The electron density was measured from the critical angle X-ray reflectivity measurements and was found to be  $1.9 \text{ mol e}^-/\text{cm}^3$  for  $\text{HafSO}_x$  and  $1.5 \text{ mol e}^-/\text{cm}^3$  for  $\text{ZircSO}_x$ , and for comparison  $0.64 \text{ mol e}^-/\text{cm}^3$  for PMMA. The Bethe equation, modified by Joy and Luo, states that the stopping power for an electron in a solid is directly proportional to the electron density of the solid.<sup>54</sup> Thus, from the electron densities values measured the new resists were observed to absorb the energy of the incident electrons more effectively compared to PMMA. This, in turn, will reduce the unwanted exposure of the resist due to the backward scattering of the electrons. In addition, due to the increased energy deposited in the new resists during exposure, their sensitivity is also improved compared to PMMA. However, the forward scattering of electrons from the beam can have a negative impact, which can be avoided by using thinner resist films.

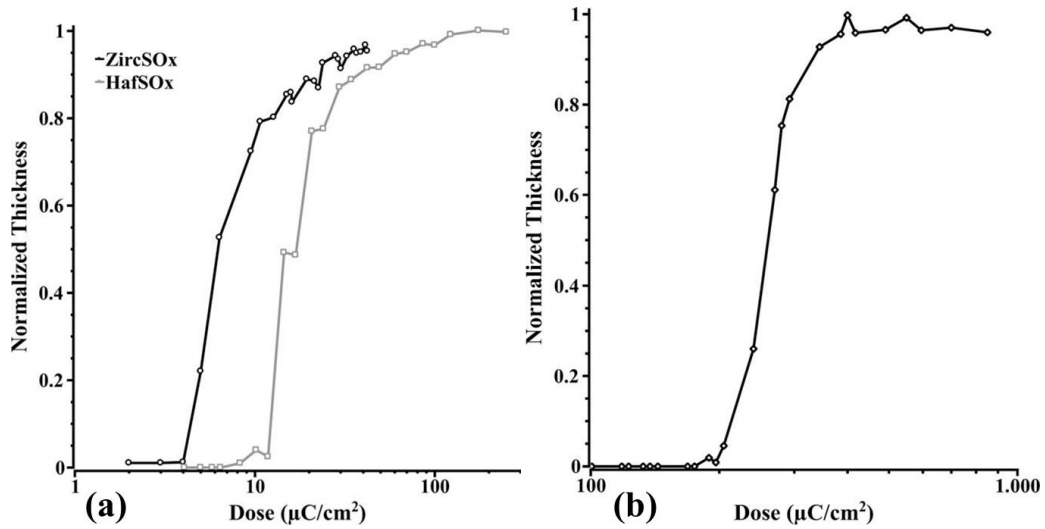


**Figure 1.15.** (a) Contrast curves of ZircSO<sub>x</sub> and HafSO<sub>x</sub> developed in TMAH and having metal: sulphate ratio of 1: 0.55 and 1: 0.5, respectively. (b) Contrast curve of ZircSO<sub>x</sub> having a metal: sulphate ratio of 1:0.7.<sup>53</sup>

The resolution of ZircSO<sub>x</sub> resist was evaluated by exposing line patterns on Si. The highest resolution achieved was a 16 nm isolated line, from a 1: 0.5 ratio of ZircSO<sub>x</sub> and sulphate as shown in Figure 1.16(a), and a dense grating with line widths of 28 nm and a period of 100 nm period, as shown in Figure 1.16(b). Isolated and dense gratings with 1: 0.7 ratio of ZircSO<sub>x</sub> and sulphate are illustrated in Figures 1.16(c) and (d), respectively. The obvious difference between the two types of gratings is the LER, which appears higher for structures prepared with the 1: 0.5 resist mixtures. The  $3\sigma$  line width roughness values calculated for isolated and dense lines were 3.4 and 6.4 nm, respectively. In comparison, the  $3\sigma$  values with the 1: 0.7 resist mixtures were 1.9 nm for an isolated line and 2.1 nm for a dense grating. For the line shown in Figure 1.16(a), a dose of 112  $\mu\text{C}/\text{cm}^2$  was required, whereas the isolated line shown Figure 1.16(c) was achieved with a dose of 999  $\mu\text{C}/\text{cm}^2$ . Thus, by increasing the sulphate concentration the quality of the structures is improved, but at

the cost of reduced sensitivity. The etch rates of  $\text{HfSO}_x$  and  $\text{ZircSO}_x$  were determined as 2.2 nm/min and 2.9 nm/min respectively, by reactive  $\text{CHF}_3$  plasma etching.

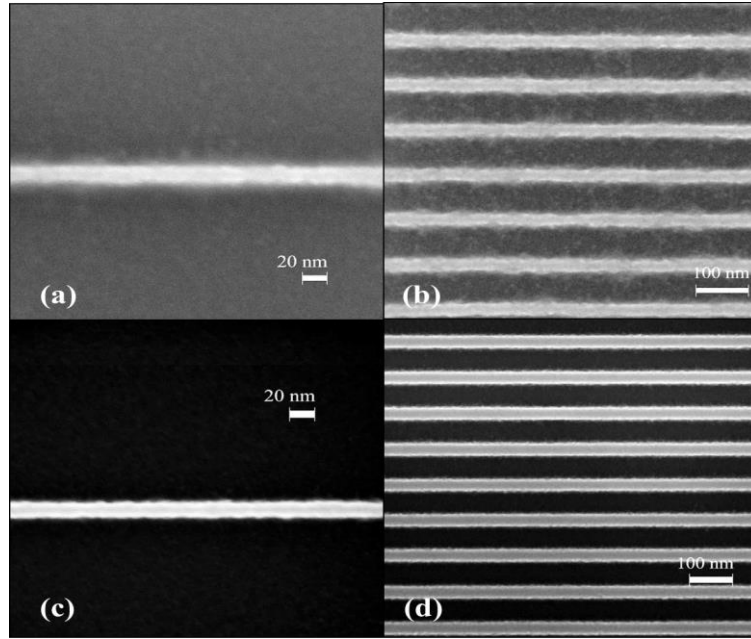


**Figure 1.16.** SEM image of a 16 nm isolated line in  $\text{ZircSO}_x$  at a dose of  $112 \mu\text{C}/\text{cm}^2$ , (b) SEM image of 28 nm lines in a 100 nm period in  $\text{ZircSO}_x$  at a dose of  $50 \mu\text{C}/\text{cm}^2$ , (c) SEM image of a 15 nm isolated line in  $\text{ZircSO}_x$  at a dose of  $999 \mu\text{C}/\text{cm}^2$  and (d) SEM image of 36 nm lines at a 100 nm period in  $\text{ZircSO}_x$  at a dose of  $810 \mu\text{C}/\text{cm}^2$ .<sup>53</sup>

Thus, these resists exhibit high-resolution structures and high sensitivity comparable to that of CARS, with lower roughness values and a good etch durability. Significantly, the sensitivity of these resists is very high when compared to HSQ. Very high resolution is also achievable using  $\text{HfSO}_x$  and  $\text{ZircSO}_x$  resists.

### 1.4.6 Miscellaneous Resists

There is a variety of commercial resists available with different lithographic parameters. For instance, incorporating metal into a material can boost the etch resistance of a resist. Metal salts of methacrylic acids (MAA), *e.g.* Pb, Ba, Ca and Sr, have been incorporated into PMMA resists.<sup>55</sup> The sensitivity of PMMA was improved by a factor of 3 by the best-suited metal, *i.e.* Pb. Additionally, metal-impregnated PMMA resists better withstand acidic and basic etch chemistries compared to PMMA alone. Along with the resist parameters, one major concern is the environmental and human impact of chemicals used in lithography processes. Keeping this point in mind, water-soluble resists have been reported for EBL technology that can help reduce the carbon footprint. In the next section, two different water-soluble resists are discussed.

With the purpose of achieving a creditable etch durability whilst lessening the environment impact, poly (sodium 4-styrenesulphonate) (PSS) was recently employed as an EBL resist.<sup>56</sup> Sodium not only has a positive effect on the etch resistance but, due to the ionic nature of PSS, it can also be dissolved and developed in water. The resist solution was prepared by dissolving 70 kg/mol PPS (Sigma Aldrich) in DI water to make a 7 wt/vol% solution, which produced a thin resist film of approximately 180 nm. The film was then baked and exposed with a 20 kV beam to procure contrast curves and high resolution patterns. Post exposure, the resist was developed with DI water for 10 s at room temperature. Figure 1.17 illustrates the contrast curve for the PSS resist along with its chemical structure and the high resolution patterning by EBL in PSS.

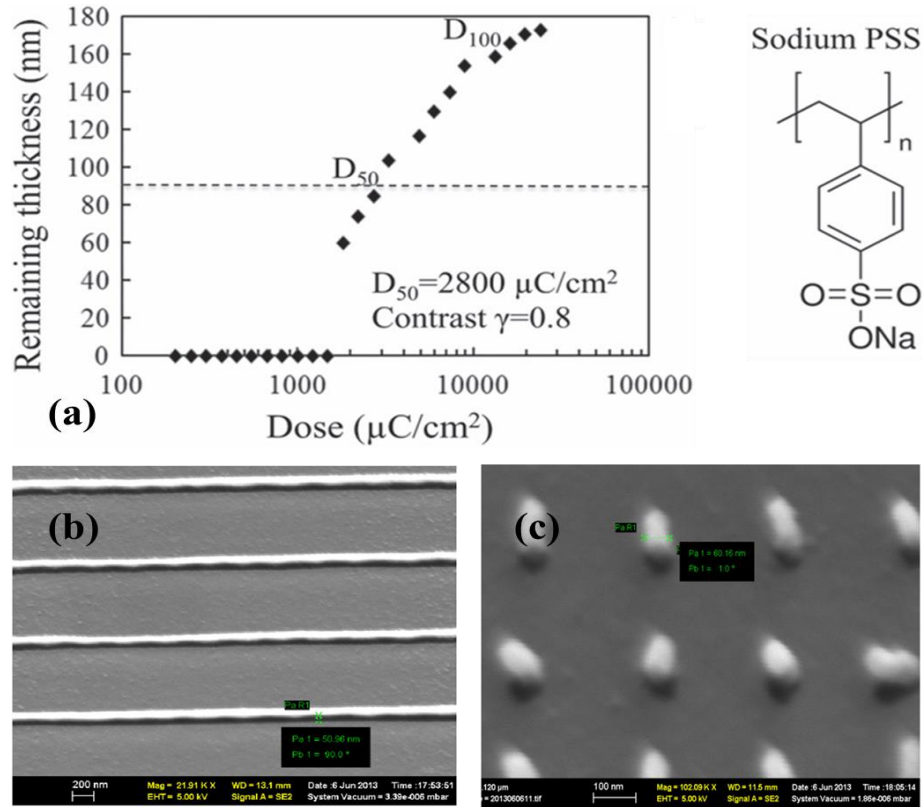


**Figure 1.17.** (a) Contrast curve of the water-soluble PSS resist, (b) SEM image showing a line array with a line width  $\sim 60$  nm (narrower lines were found to have collapsed). (c) SEM images showing arrays of pillars with a mean diameter of 60 nm.<sup>56</sup>

From the contrast curve in Figure 1.17(a), the sensitivity of  $2800 \mu\text{C}/\text{cm}^2$  is poor, as is the contrast of 0.8. However, the authors suggest that the use of higher molecular weight PSS to improve its sensitivity drastically, since for the cross-linking polymer chains the exposure dose is found to be inversely proportional to its molecular weight.<sup>57</sup> However, the resist would not be ideal for high-resolution patterning as the EBL process would be extremely sluggish. For testing the etch resistance, an  $\text{O}_2$  plasma RIE test (20 sccm  $\text{O}_2$ , 20 mTorr, 20 W RF power) of PSS was compared to PMMA. PSS showed 17 times higher etch resistance than PMMA, and 6 times



higher than SU-8 and polystyrene resists (from literature), which have similar sensitivity and contrast to that of PSS. The etch test with  $\text{CF}_4$  gas (20 sccm  $\text{CF}_4$ , 20 mTorr, 100 W RF power, room temperature) revealed that the selectivity relative to PMMA was only 3.5 times higher. This low selectivity with  $\text{CF}_4$  is thought to be because of the low percentage of Na in PSS. Finally, to assess the resolution of this poorly sensitive resist, high-resolution gratings and pillars were exposed on a 180 nm thick resist film. The resist was not good for dense exposures and gratings with 100 nm spacing were not achievable. The critical dimensions achieved were 60 nm linewidth and pillars with a mean diameter of 60 nm, which are quite reasonable for a 180 nm thick resist film. However, gratings with lower spacing and pillars smaller than 40 nm in diameter collapsed due to the capillary force during drying after water development. Additionally, the authors demonstrated a metal lift-off of 2 kV exposed structures by DI water. To conclude, although PSS is not a model resist for fast and dense critical patterning, it definitely exhibits an excellent etch durability. Moreover, the fact that it can be developed and further processed with water, makes it environmentally friendly and makes handling the process less hazardous for humans.

Tufts University engineers have developed an apparent ‘green alternative’ resist.<sup>58</sup> Silk, a biologically fabricated material, has long been enjoyed as a luxurious and beautiful fabric, yet it is tougher than most of the synthetic fibres currently present in the market.<sup>59</sup> For this reason, silk proteins have been utilised in recent years in areas as diverse as photonics, electronics, drug delivery and bio-scaffolds.<sup>59,60,61</sup> Engineers in Tufts University expanded the possibility of using silk as a nanofabrication material. They showed that EBL was able to change the protein structure upon

irradiation thus making it a candidate for EBL resists. This report demonstrated that the silk resist can be used as either a negative (amorphous silk form) or positive (crystalline silk form) resist. Moreover, silk can be converted into ‘functional resists’ by doping the resist solutions with organic, inorganic or even biologically active materials. In this segment silk resist preparation, sensitivity values and its resolution will be discussed.

Resist solutions were produced by boiling silk cocoons in sodium carbonate solution to obtain fibres, which were then dried overnight. The dried fibres were subsequently dissolved in 9 M lithium bromide resulting in a ~7 % aqueous resist solution of silk fibroin. The resist was then spun onto a substrate to give a 200 nm thick silk layer; the thickness of which could be controlled by the spin speed. In order to yield a negative resist, after spin coating the intermolecular crosslinking within the resist was achieved by either exposing the substrates to water vapour for > 12 h or by dipping in methanol for 60 s, followed by exposure to water vapour for 2 h. Both resists were typically exposed with high-energy beams of 100 and 125 kV. The development of the resists was done by simple immersion in DI water for 60 s and drying.

The minimum doses required to fabricate nanostructures at 100 kV were reported. In the case of the positive resist the dose required to fabricate nanoscale features was  $2250 \mu\text{C}/\text{cm}^2$  and that for the negative form was  $25,000 \mu\text{C}/\text{cm}^2$ . These values are 2.5 times higher than that required by PMMA at 100 kV.<sup>62</sup> Figure 1.18 illustrates photonic crystals formed, having various spacing, obtained by EBL exposure of both

varieties of the silk resist.

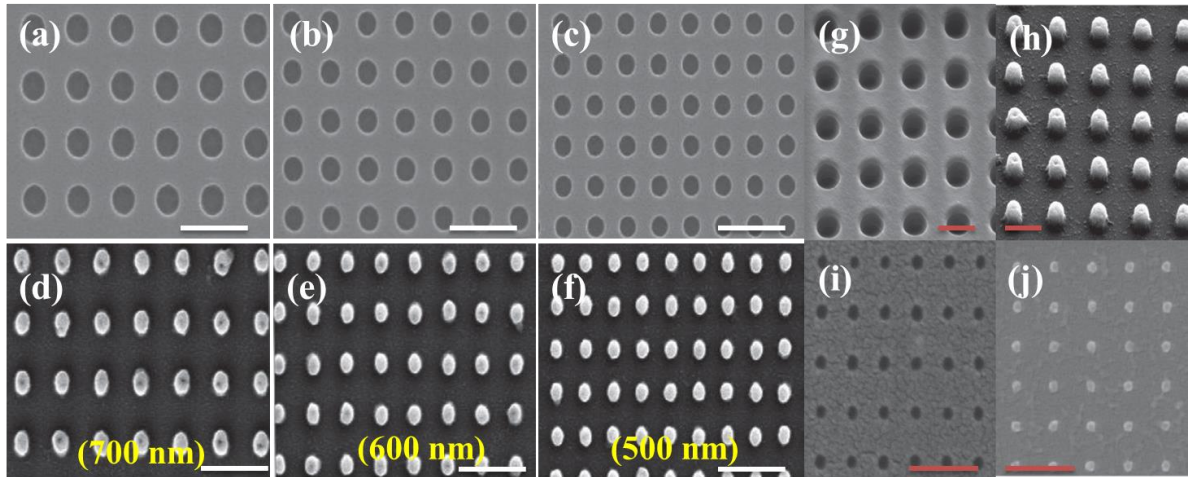


**Figure 1.18.** (a-c) SEM images of photonic crystals fabricated with positive silk whereas (d-f) are with negative silk; with a lattice constant or periodicity for (a) and (d) of 700 nm; for (b) and (e) 600 nm; for (c) and (f) 500 nm; (g) and (h) are 200 nm diameter holes and pillars, respectively; (i) and (j) are highest resolution 30 nm holes and pillars patterned by the silk resist.<sup>58</sup>

Evident from the SEM images shown in Figure 1.18 is that the ‘green’ resist is capable of fabricating nanostructures competently. Images from Figures 1.18(a-c) are the photonic crystals fabricated with a positive silk resist, whereas Figures 1.18(d-f) are produced with a negative silk resist, with lattice constant (periodicity) of 700 nm (Figures 1.18(a and d)), 600 nm (Figures 1.18(b and e)) and 500 nm (Figures 1.19(c and f)). The diameters of the crystals were designed to be 200 nm; and from the SEM images in Figures 1.18(g) and (h) it can be seen that there is no widening or narrowing of the structures, thus suggesting that the resist is capable of good lithography. Figures 1.18(i) and (j) illustrate the highest resolution obtainable with the two resists, that is, 30 nm holes and pillars with positive and negative

resists, respectively. Furthermore, the authors suggested that these resolution limits can be pushed further by tuning the molecular weight of the silk solution or by adding other biomolecules, for instance, microbial transglutaminase or mushroom tyrosinase. Thus, the possibility of using a biomaterial, silk, for EBL process was successfully demonstrated in this study. Moreover, another advantage of using silk, highlighted by them, is the ease of functionalising them to act like a unique class of bio-active resist. To conduct their tests, the silk solutions were doped with quantum dots, green fluorescent proteins (GFP) or horseradish peroxidase enzyme (HRP). They were able to validate the fabrication of high-quality nanoscale optics like quantum dots (inorganic) or GFPs (organic) that enhanced the fluorescent signalling from the silk devices. To conclude, this is a new, eco-friendly resist which minimises the need to work with toxic chemicals and is potentially a step towards establishing a green cleanroom process.

### 1.5 LITHOGRAPHY BY GRAPHOEPI TAXY

By the beginning of 21<sup>st</sup> century, the improved performance of microelectronic devices showed signs of slowdown, largely due to limitations arising from patterning tools.<sup>63</sup> In order to deliver further miniaturisation, methods must be fashioned which allow material engineering at the molecular level. Bottom-up technologies are an instinctive alternative to traditional top-down lithography, which mainly involves the use of various polymers. They involve simpler processes of lithography and furthermore, they are the cheaper option to the former since they do not require expensive facilities or equipment. Lithography with such polymer materials is also compatible with the existing integrated circuits technology since they are chemically

similar to photo or EBL resists. In this approach, the nanoscale features are obtained from their molecular constituents that are driven to self-assembly by kinetic processes or thermodynamic forces.<sup>64</sup> The term self-assembly defines the spontaneous yet regular arrangement of nanoscale units in order to attain a minimum free energy by minimising the repulsive and maximising the attractive molecular interactions.<sup>65</sup>

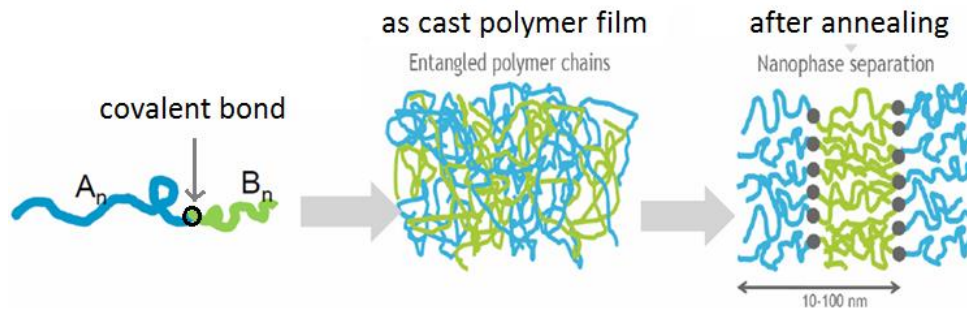


**Figure 1.19.** Schematic illustration of a di-block copolymer bonded covalently, forming entangled polymer chains after depositing on a substrate and finally phase-separating into nanodomains post annealing.<sup>70</sup>

Recently, block copolymers (BCP) have been an area of interest for nanofabrication due to various potentials such as molecular scale pattern precision, ultrafine line edge roughness (LER), and low-cost processing.<sup>66,67,68</sup> BCPs are a special class of polymers where two or more homopolymers subunits are polymerised to produce BCP chains.<sup>67</sup> BCPs consisting of two or three homopolymers are known as di-BCP or tri-BCP, respectively. In this thesis, the emphasis is on using di-BCPs, *i.e.* two blocks of polymers, which are immiscible, chemically distinct but covalently bonded to each other as illustrated in Figure 1.19. These covalently bonded BCPs are dissolved in organic solvents to give homogenous polymer solutions. The BCP

solution is spin-casted on the functional substrate and forms a thin BCP film on it. The thin film is subsequently annealed above the glass transition ( $T_g$ ) temperature but below the order–disorder transition temperature (ODT) to promote microphase separation between the two blocks of polymers.<sup>69</sup> The two immiscible blocks of the BCPs can microphase separate to form morphologies like spheres, gyroids, lamella, *etc.*, depending on the composition ratio of the two blocks of monomers. Thusly formulated ordered nanoscale features have a larger output by a very simple approach and can be used as lithography masks for arrays of dense lines or hexagonally packed dots.

The BCP can microphase separate into various complex nano-sized morphologies depending on the volume of one of the blocks with respect to the other. Self-assembly or ordering is dependent on two primary parameters:  $\chi$  and  $N$ , which are the Flory-Huggins segment-segment interaction parameter and the total degree of polymerization, respectively. The Flory-Huggins interaction parameter,  $\chi_{AB}$ , describes the driving force for this micro-phase separation (equation 1.2)<sup>71</sup>

$$\chi_{AB} = \left( \frac{z}{k_B T} \right) \left[ \epsilon_{AB} - \frac{1}{2}(\epsilon_{AA} + \epsilon_{BB}) \right] \quad (1.2)$$

where , A and B are the two blocks of the BCP,  $k_B T$  is the thermal energy, and  $\epsilon_{AB}$ ,  $\epsilon_{AA}$ , and  $\epsilon_{BB}$  are the interaction energies per monomer between A and B, A and A, and B and B, respectively (a negative or positive  $\epsilon$  indicates favourable or unfavourable interactions, respectively) and  $z$  is the number of nearest neighbours per monomer in the polymer.<sup>72</sup> According to the self-consistent field theory, when the value of  $\chi_{AB} N$  ( $N$  = degree of polymerisation) is greater than 10.5, microphase

separation will occur.<sup>72</sup> The two blocks of the BCP are fundamentally non-miscible, however they do not macro-phase separate, instead, owing to the fact that they are covalently bonded, the phase separation occurs on a molecular level and the system adopts extended chain conformations. The two blocks will separate from each other to minimise the interfacial energy and consequently, the interfacial surface area. The morphology resulting due to the minimisation of energy represents the most favourable configuration for a specific block copolymer.<sup>71</sup>

However, the spontaneity of microphase separation causes random orientation of the nanostructures formed, which limits the potential of this technique. This issue has led to a host of attempts to order BCP domains, particularly using predefined templates. Predefined templates are typically engineered using top-down nanofabrication techniques. Such an amalgamation of top-down with the bottom-up technology is known as directed self-assembly (DSA). In this manner, ordered lamellar or cylindrical domain patterns, often with density multiplication, can be obtained. DSA of BCPs are often conducted via two routes, *i.e.* epitaxial self-assembly or by graphoepitaxy.<sup>73</sup> In the case of epitaxial self-assembly, a surface is chemically pre-defined to direct the self-assembly of the BCP. The surface can be passivated chemically which can promote ordering of one or both the blocks, thus resulting into well-aligned patterns. On the other hand, in graphoepitaxy topological patterns are produced by top-down techniques such as EBL, photolithography, and such, to give pillars, trenches or boxes for guiding the self-assembly of the BCPs, as first introduced in 2001.<sup>74</sup> Figure 1.20 illustrates a simple graphoepitaxy process.<sup>75</sup> One of the blocks must exhibit selective affinity towards the trench sidewalls, which can enforce lateral ordering of the domains of

the BCP along the sidewalls. This process not only orders the BCP alignment, but also multiplies the pattern density between by subdividing the two trenches.

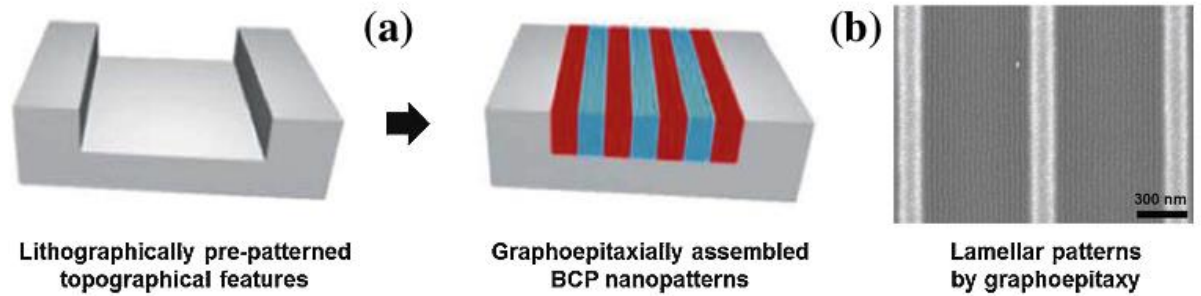


**Figure 1.20.** (a) Schematic illustration of graphoepitaxy using topological patterns created by top-down lithography process for guiding the alignment of BCP. (b) SEM image of dense and highly aligned lamellar patterns formed by graphoepitaxy<sup>74</sup>

One such example is the application of HSQ posts patterned by the EBL which has been used for guiding the thin BCP film of poly (styrene-*b*-dimethylsiloxane) (PS-*b*-PDMS) with a molecular weight of 51.5 kg/mol.<sup>75</sup> This particular BCP was chosen because both the polymers have a high Flory-Huggins  $\chi$  parameter, which facilitates their maximum phase separation. Moreover, the chemical selectivity between the two blocks is very high, which was useful during pattern transfer via reactive ion etching by CF<sub>4</sub> chemistry.



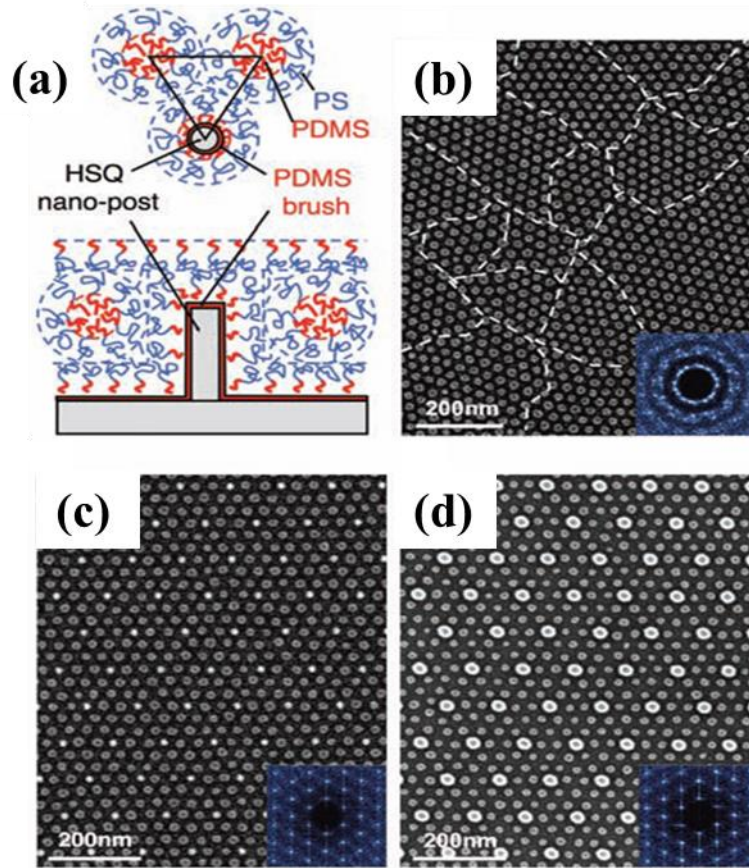


**Figure 1.21.** (a) Top-down and side-view schematics showing the arrangement of PS-b-PDMS block copolymer molecules in the region surrounding a single post made from cross linked HSQ resist. The post and substrate surfaces have been chemically functionalised by a monolayer of a short-chain PDMS brush. (b) SEM images of a poorly ordered monolayer of BCP spherical domains formed on a flat surface, i.e., without templating. The boundaries between different grain orientations are indicated with dashed lines. The inset is a 2D Fourier transform of the domain positions that shows the absence of long-range order. (c) and (d) SEM images of ordered BCP spheres formed within a sparse 2D lattice of HSQ posts (brighter dots). The substrate and post surfaces were functionalised with a PDMS brush layer in (c), which corresponds to the schematic in (a), and with a PS brush layer in (d). The insets show the 2D Fourier transforms in which the low-frequency

*components originate from the post lattice.*<sup>75</sup>

Figure 1.21 illustrates the process of graphoepitaxy of PS-*b*-PDMS BCP by HSQ pillars fabricated by top-down method. Figure 1.21(a) shows a schematic of a HSQ pillar coated with a PDMS brush so that the HSQ post exhibits an affinity to one of the blocks; which will help to improve the ordering of the BCP. Figure 1.21(b) shows an SEM image of a surface having randomly arranged PDMS due to the lack of HSQ pillars. The dashed lines indicate the boundary between different grains or dot orientation. Figure 1.21(c) shows the SEM image of well-ordered PDMS domains around the HSQ pillars (brighter dots) on a surface pre-treated with a PDMS brush layer. The HSQ posts were designed to be ~12 nm (size similar to that of the PDMS domains) and were covered by ~2 nm of PDMS layer, making them approximately 16 nm sized posts. Whereas, the SEM image shown in Figure 1.21(d) is of the template surface pre-treated with a PS brush. The ordering of PDMS domains is visibly better than that on plain surface but not as good as compared to Figure 1.21(c). The fact that PDMS-coated pillars allow better ordering of the BCP compared to the PS-brush or the untreated pillars is because PDMS has a higher surface diffusivity.<sup>76</sup> However, as seen in Figure 1.21(d), the HSQ posts were designed to have a diameter similar to that of PS component (major BCP component), which is larger than the PDMS posts. Therefore, PS brush template required wider HSQ posts for good arrangement of the BCP. Also, in all of the SEM images the PS matrix is selectively etched to retain the PDMS and HSQ posts on the surface. Thus, it is evident from this study that templating the surface prior to BCP spinning can seamlessly orient nanostructures. This technique is not confined to just one BCP system.

In another study, poly(styrene-*b*-methyl methacrylate) (PS-*b*-PMMA) was used to rectify the quality of arrays of EBL generated dots, *i.e.* to obtain uniform and ordered arrangement of the BCP nanodots over a larger area, and to increase the pattern density of EBL output.<sup>77</sup>

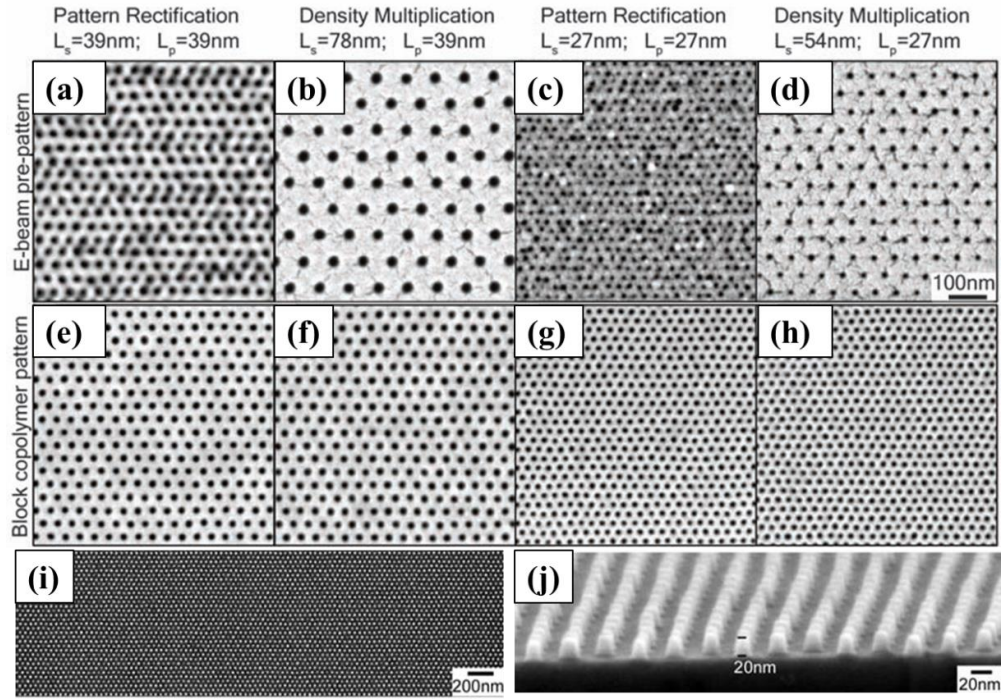


**Figure 1.22.** (a) to (d) SEM images of developed PMMA resist with  $L_s = 39, 78, 27,$  and  $54$  nm, respectively. (e) to (h) SEM images of the block copolymer film on top of the pre-pattern defined by the corresponding EBL pattern above. The lattice pitch on the block copolymer samples was  $L_p = 39, 39, 27,$  and  $27$  nm, respectively.<sup>77</sup>

This work describes good example of graphoepitaxy, where EBL assistance is important for healthy long range ordered arrangement of BCP domains and BCP, on the other hand, supplements to densify the EBL pattern structures. The study

extended to successful patterning of large areas of well-arranged nanopillars up to  $100 \times 100 \mu\text{m}^2$  and  $3000 \times 50 \mu\text{m}^2$  and subsequently transferring the dot array into  $\text{SiO}_x$  substrates. The experimental process in this study slightly varied from the previous study mentioned.<sup>71</sup> In this process EBL exposure was carried out after depositing the PS brush ( $M_n = 6 \text{ Kg/mol}$ ) with hydroxyl termination. The periodicity of the PMMA cylinders in the PS matrix are given by  $L_p$  and  $L_s$  is the periodicity of EBL patterned dots. Figure 1.22 demonstrates a schematic representation of the entire process wherein the final product is supposedly a dense and superior quality array of dots.

EBL exposures were done using 950 K PMMA and holes were drawn in the resist with  $L_s = 39$  and  $27 \text{ nm}$  for pattern rectification and  $L_s = 78$  and  $54 \text{ nm}$  for density multiplication. After this step the nanopillars were exposed to oxygen plasma to generate a chemical contrast on the substrate and the EBL resist was subsequently stripped-off from the substrate. A suitable BCP solution was then spin-coated onto this substrate and further processes were conducted. Figure 1.22 illustrates the SEM micrographs from (a) to (d) of the EBL patterned resist structures and (e) to (f) of their corresponding BCP repaired patterns. In Figures 1.22(a) and (c) the periodicity of EBL patterns was  $39$  and  $27 \text{ nm}$ , respectively, *i.e.*  $L_s = L_p$ . After depositing the BCP film, the PMMA block preferentially settles on the areas exposed with plasma and the PS block wets the background areas. The PMMA block is subsequently removed and Figures 1.22(e) and (g) correspond to the SEM images of the EBL pattern ( $L_s = 39$  and  $27 \text{ nm}$ , respectively) emended by the BCP system. SEM images in Figures 1.22(b) and (d) define the widely spaced EBL holes, having  $L_s = 78$  and

54 nm, respectively. A BCP thin film was spin-coated on this surface to increase the pattern density which can be seen in Figures 1.22(f) and (h). This process was successful in rectifying the pattern and multiplying its density efficaciously. Long range ordering of pre-patterned areas, up to  $3000 \times 50 \mu\text{m}^2$  was also reported. The authors also estimated that the defect density was less than  $<10^{-4}$  for patterns with  $L_s = 39, 78$  and  $27$  nm and  $<10^{-3}$  for those with  $54$  nm. Figures 1.22(i) and (j) illustrate the pattern transferred using this DSA method wherein Figure 1.22(i) shows the chromium metal dots achieved by lift-off and Figure 1.22(j) shows  $20$  nm tall Si pillars achieved by etching the Cr metal mask. A possible application of such high density arrays of defect-free dots is in patterned media (a potential future hard disk drive technology) which requires  $1$  terabit per square inch of orderly structured dots. Moreover, they can be used for quantum dots fabrication or for creating nanoporous membranes.<sup>78,79</sup>

A newer technique of graphoepitaxy involving the use of nanoimprint lithography (NIL) has recently been developed.<sup>80</sup> DSA was achieved using low molecular weight PS-*b*-PDMS ( $11 - 5$  kg/mol) blocks where sub- $10$  nm features were fabricated. The interesting fabrication process is described in Figure 1.23. The four imprint molds were PS and PDMS coatings, passivated with fluoroalkyles (FA) and hydroxy (OH) groups to aid the release of the mold from the patterned substrate. Subsequently, Si substrates were spin-coated with the BCP in toluene solution. Thermal nanoimprinting of the Si substrates was executed by pressing the Si substrate and the molds between two metal plates at  $\sim 50$  psi and were subsequently annealed at  $200^\circ\text{C}$  for  $1$  h. The system was then gradually cooled down over a



period of 1 h and the molds were removed along the length direction of the molds. The substrates were then subjected to a 5 s  $\text{Cl}_2$  etch to remove the top PDMS film and then  $\text{O}_2$  etched for 10 s to reveal long range 8 nm wide  $\text{SiO}_x$  lines with a  $(20 + 8)$  nm pitch size on the Si substrates. Out of the fluoroalkyl terminated molds, FA-PS gave the best results. However, amongst the four mold types, OH-PDMS mold showed the most enhanced performance, *i.e.* released the BCP film from the thermally imprinted molds easily and was used up to 10 times without regenerating the brush.<sup>80</sup> This behaviour is due to the fact that PDMS has a lower peel-fracture than the perfluoro groups, potentially giving lower friction losses than that of FA-PS when the mold is removed from the patterned film.<sup>81</sup>

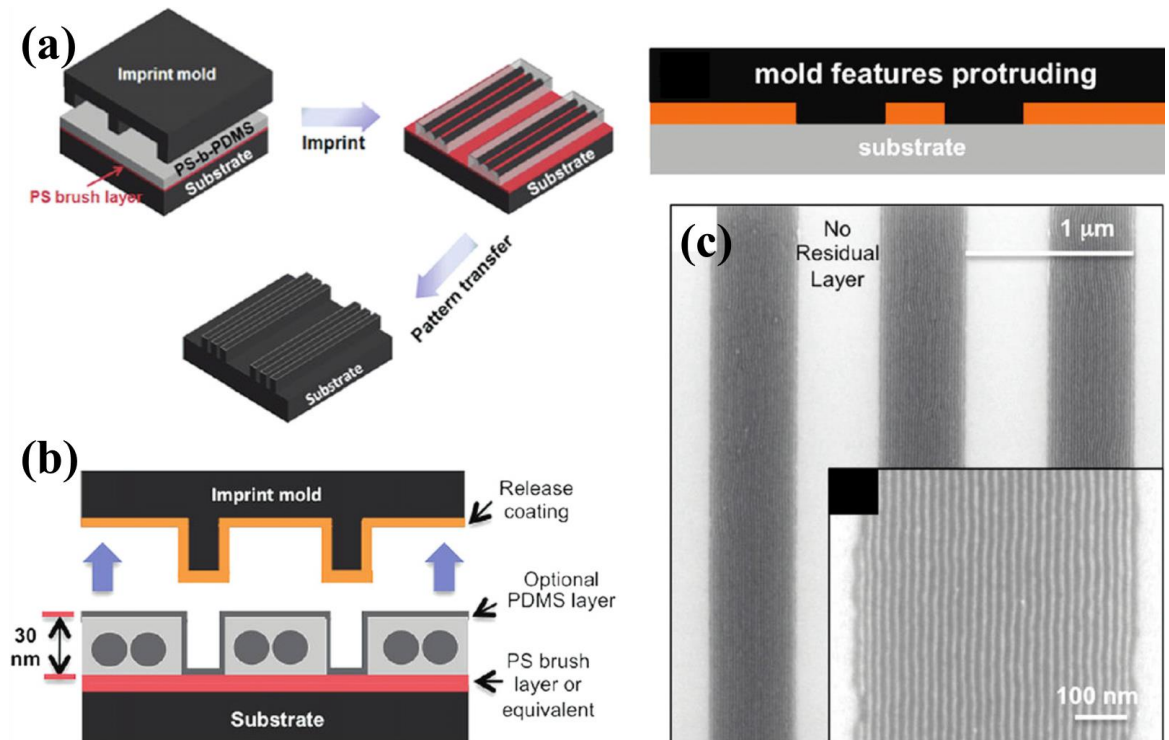


**Figure 1.23.** (a) Schematic illustration showing thermal nanoimprint inducing the alignment of cylindrical domain of PS-b-PDMS along the length of the mold followed by the pattern transfer in the substrate. (b) Substrate coated with PS layer

*that attracts the PS block and imprint mold is treated with a layer that attracted the PDMS block. The layer on the mold promotes release of the mold and alignment of one of the BCP blocks. (c) SEM image showing O<sub>2</sub> plasma etched BCP film after the nanoimprint process. Inset shows magnified oxidized PDMS cylinders aligned parallel to the sidewall of the imprint mold<sup>80,81</sup>*

BCP lithography is an incipient technology for nanoscale fabrication because it is compatibility with the current semiconductor industry requirements and is a low budget route as compared to top-down lithography ones. The lack of long range order of BCPs can be controlled by introducing boundaries produced by conventional top-down lithography processes. To extract maximum benefits from BCPs for nanofabrication purpose, control of the long range BCP arrangement, pattern densification of sub 10 nm features and transferring the pattern successfully in the functional substrates is coveted. If and when the process for controlling these parameters are mastered, the pressure on top-down lithography for continued scaling-down can be eased. Graphoepitaxy, thus, offeres a low cost and simple route for high-resolution nanofabrication.

### 1.6 ADVANCED LITHOGRAPHY

Top-down fabrication of the devices has, over the years, improved tremendously. Presently, the trend has diverted to three dimensional (3D) device fabrication.<sup>82</sup> 3D devices find applications in a large number of fields including photonic crystals, biosensors and metamaterials.<sup>82,83,84</sup> Especially the devices that are fabricated with EBL technique require multiple steps and precise alignment of different layers.<sup>85,86,87</sup>

Besides the EBL method, advances in appliances employed in device fabrications are also being upgraded continuously and form the so-called next generation lithography (NGL) systems, which are highlighted earlier in section 1.2. Few of the NGL systems are discussed next. Proton beam lithography or proton beam writing (PBW) is used for nanofabrication. Reports of utilising this technique for high aspect ratio and 3D fabrication are published, wherein multiple p-beams with different energies (and at different incident angles) are used for nanofabrication.<sup>88,89</sup> Helium ion lithography (HIL) is also an example of a NGL process, which has successfully patterned not only non-traditional semiconductor materials like graphene but is capable of also directly patterning metals. Due to the fact that ions are much heavier than electrons, they experience less scattering in the resist and the substrate and the proximity effect here is almost negligible, enabling resolution beyond that of EBL.<sup>90</sup>

The next generation lithography (NGL) techniques are, however, relatively expensive and not mature enough for widespread application. Their use for mass-production seems at the moment highly unlikely. Therefore, it is necessary to better understand these top-down techniques as well as to improve the existing techniques for nanoscale fabrication. Bottom-up techniques like DSA of BCPs are also a promising technology favouring the progress of nanofabrication.

### 1.7 CONCLUSION

Lithography is a vital element of nanoscale fabrication. In the last decade, the critical dimension of microelectronic devices has dramatically reduced while circuit



complexity has increased. Consequently, the requirement for microfabrication technology reaches into the nanometre regimen. In order to meet the requirements, the need has arisen for finer pattern generation and lithography systems with superior performance specifications. Advances in EBL systems have led to reduction in the beam size diameter down to 2 to 1 nm. However, achieving feature sizes equivalent to this small probe size remains difficult to achieve, mainly due to the issues with resist morphologies and lithographic processes. To obtain the best outcome from any EBL process the tool and the resist parameters must be optimised for good outcomes. All the resist parameters collectively described in Section 1.3 of this Chapter determine the quality of a resist. Nevertheless, it is not always that a single resist will exhibit all the parameters commendably, *i.e.* the resist may have a high resolution but may suffer low sensitivity value or etch durability. Due to the growing interest of lithography community to attain high performance lithography, interest has been raised to develop novel EBL resists. In this thesis, several new resists belonging to various families and exhibiting various functions are detailed. The resist families are classified according to their chemical compositions.

Firstly, the chemically amplified resists (CARS) were discussed and it is evident from the new as well as early reports that this division of resists are extremely sensitive to electron beam. State-of-art CARS exhibit electron sensitivity from  $7 \mu\text{C}/\text{cm}^2$  up to  $200\text{-}300 \mu\text{C}/\text{cm}^2$  and are able to offer high resolution structures down to 15 nm. The main issue with CARS is photo acid generation, not only during exposure but also in the interval between spinning the resist and exposure. This issue has been countered by casting a protective layer over the resist, which

does not affect the sensitivity of the resist and protects it from unwanted alterations in the composition due to acid diffusion. Thus, by protecting the resist their stability is improved, which can lead to enhanced sensitivity and also ease patterning that requires mix-and-match lithography wherein one substrate requires two different patterning procedures with different or same tools. By controlling the acid diffusion within the resist after electron exposure and exploiting the advantage of high sensitivity of CARS, they project as worthy next-generation lithography resists. Conversely, in order to eradicate the additional, unwanted acid-diffusion concern of the CARS completely, non-CARS resists are formulated. Such resists include, mainly, a sulphonium salt portion that will allow these resist to exhibit high sensitivity.

The infusions of a fullerene,  $C_{60}$ , moiety into various polymer blends leads to beneficial resist characteristics like high sensitivity and resolution, high etch resistance, low line width roughness and compatibility with industrial processing. Such resists can account for newer class of resists. In order to gain the best productivity from such resists exploring more about the exposure mechanism, better understanding the role of  $C_{60}$  in the whole EBL process and tuning resists parameters should be undertaken.

Methacrylate based resists are one of the generally preferred families of resists, due to the ease of handling and simplicity in their chemical formulation and exposure mechanism as compared to CARS or fullerene based resists. Conventional resists like PMMA, ZEP or SAL (Shipley Advanced Lithography) belong to this family of resists. Newer products from this family, such as SML or CSAR are modified to

have increased sensitivity, etch durability and high resolution.

The highest resolution of  $\sim 7$  nm nanoscale features have been achieved by EBL using an inorganic resist.<sup>91</sup> The widespread use of these resists is usually hindered due to their low sensitivity. HSQ is one of the most commercially and scientifically successful EBL resist, but it displays relatively low sensitivity. Thus, the inorganic resists prepared recently exhibit higher sensitivity while maintaining high resolution. Most of these new inorganic resists contain metal components such as hafnium, zirconium or aluminium.<sup>53</sup> These resist do not only break the sensitivity limitations of inorganic resists but are also compatible for nanofabrication processes. They can be deposited easily from their aqueous solutions and also form even thickness films on substrates.

Traditional EBL resists are mainly formulated with a view to gain maximum throughput over a fast processing period, often leading to the use of hazardous chemicals for processing, or even the resists themselves can be perilous in nature. Recently, benign resist materials have also been developed, for example the use of polyanilines water-based conducting EBL resists.<sup>92</sup> Biomaterials such as silk have also been demonstrated as potential eco-friendly EBL resists.

**Table 1.4.** Summary of the resists based on their family, tone; positive (P) or negative (N), developers, sensitivity, contrast, electron beam voltage and the critical dimension (CD) attained in the resists

Name	Family	Tone	Developer	Sensitivity ( $\mu\text{C}/\text{cm}^2$ )	Contrast	EBL Voltage kV	CD (nm)
<b>Poly(GM A-co-MMA-co-TPSMA)</b>	CARS	N	7:3 IPA:DI water	125	-	100	15
<b>PEDOT-PSS</b>	CARS	P	AZ®7 26MIF	7	7	20	80
<b>MAPDST-MMA</b>	CARS	N	TMAH	2	1.8	20	20
<b>C<sub>60</sub>-P(CMS<sub>14</sub>-HS))</b>	Fullerene Derivative	N	Acetone/Toluene	40	-	100	50
<b>IM-MFP12-3</b>	Fullerene Derivative	N	Acetone	90	1.8	20	50
<b>SML</b>	Meth-acrylate	P	7:3 IPA:DI water	60	9.2	10	15
<b>CSAR 62</b>	Meth-acrylate	P	Amyl-acetate	172	5.2	100	10
<b>HafSO<sub>x</sub></b>	Inorganic	N	TMAH	21	2.5	30	-
<b>ZircSO<sub>x</sub></b>	Inorganic	N	TMAH	8	2.6	30	16
<b>PSS</b>	Water-soluble	N	DI water	2,800	0.8	20	60
<b>Silk</b>	Water-soluble	P & N	DI water	2,250 (P) 25,000 (N)	-	100	200 (dot)

In conclusion, in the past few decades, many materials have been suggested as potential EBL resists. High sensitivity and resolution together with good etch resistance continually remain the most desirable characteristics of EBL resists. The different classes of resists detailed in this Chapter highlights the recent progress currently being made in the development of resist materials. Table 1.4 summarises all the resists reported hitherto along with their family type, tones, developers, sensitivity and contrast values achieved at specific electron beam voltages and the critical dimension achieved by the resist. It is to be noted that in the case where two or more resist derivatives were reported, only the one with the best performance are tabulated in table 1.4.

The main motivation of the research represented in this thesis is to fabricate novel nanowire devices taking the top-down approach. In order to conduct this study, EBL tool was to be employed. Hence, it was of utmost importance to thoroughly understand the EBL technique and the processes that follow it, to push the limits of existing nanometre resolution achieved by the EBL in general. Thus, the research consists of work explaining new and longstanding EBL resists, which are an integral part of the EBL technology. Followed by, enhancing the critical dimensions of an existing high-resolution EBL resist. Therefore, to gain an insight on the resist processing was described in the previous sections of this Chapter. Lastly, exploring an alternative, cost-effective and time-preserving method, that also involves the bottom-up approach. Graphoepitaxy was, hence, expressed in Section 1.5 of this thesis. The final accomplishment was to demonstrate the applications of the techniques that were developed for actual semiconductor nanofabrication.

## 1.8 THESIS SUMMARY

This thesis highlights the advancements in EBL patterning in order to achieve high resolution patterning. Chapter 3 details characteristics of the new positive tone resist SML and its competence as an EBL resist with respect to conventional PMMA and ZEP resists. The chemical structure of SML is also related to the lithography performance of the resist.

Chapter 4 informs the EBL patterning of Ge surfaces with HSQ resist using a new technique. Thus, this chapter describes this innovative surface passivation procedure and the mechanism of this reliable patterning technique of Ge with HSQ. Moreover, the application of this fabrication procedure along with SML resist in the fabrication of functional devices is also detailed in this Chapter.

The directed self-assembly of block copolymers on EBL defined substrates is detailed in Chapter 5. This method was used to fabricate dense arrays of nanowires on Si and, for the first time, on Ge surface. The chapter elucidates the fabrication and characterisation of the self-assembled block copolymers on the two different surfaces.

## 1.9 BIBLIOGRAPHY

1. H. Chen, M.C. Roco, X. Li, Y. Lin. *Nat. Nanotechnol.* 2008, **3**, 123.
2. <http://www.nanowerk.com/nanotechnology>

3. C.G. Willson, R.R. Dammel, A. Reiser. *Proc. SPIE, Emerging Lithographic Technologies*. 1997, **3048**, 28.
4. G.R. Brewer, in *Electron-Beam Technology in Microelectronic Fabrication*. Ed. 1980, pp. 2-56.
5. [http://www.epixfab.eu/index.php?option=com\\_content&view=article&id=57&Itemid=72](http://www.epixfab.eu/index.php?option=com_content&view=article&id=57&Itemid=72)
6. A.E. Grigorescu, C.W. Hagen. *Nanotechnology*. 2009, **20**, 292001.
7. H. Kirchauer. *Photolithography Simulation* (Doctoral Dissertation). Institute for Microelectronics, TU Vienna. 1998.
8. Z. Cui in *Nanofabrication: principles, capabilities and limits*. 2008.
9. J.-S. Wi, H.-S. Lee, K.-B. Kim. *Electronic Mater. Lett.* 2007, **3**, 1.
10. H. Yang, A. Jin, Q. Luo, C. Gu, Z. Cui. *Microelectron. Eng.* 2007, **84**, 1109.
11. A. Gangnaik, Y.M. Georgiev, B. McCarthy, N. Petkov, V. Djara, J.D. Holmes, *Microelectron. Eng.* 2014, **123**, 126.
12. C. S. Wu, Y. Makiuchi, C. Chen, in *Lithography*, ed. M. Wang, Intech, Vukovar, 2010, pp. 241-266.
13. T.H.P. Chang. *J. Vac. Sci. Technol.* 1975, **12**, 1271.
14. K. Koshelev, M.A. Mohammad, T. Fito, K.L. Westra, S.K. Dew, M. Stepanova. *J. Vac. Sci. Technol. B*. 2011, **29**, 306.
15. J.K. Yang, B. Cord, H. Duan, K.K. Berggren, J. Klingfus, S.W. Nam, K.B. Kim, M.J. Rooks. *J. Vac. Sci. Technol. B: Microelectron. Nanometer. Struct.–Process., Meas., Phenom.* 2009, **27**, 6.
16. A. Novembre, S. Liu in *Nanolithography: The Art of Fabricating Nanoelectronic and Nanophotonics Devices and Systems*, ed. M Feldman. 2014, pp. 194-286.

17. S. Yasin, D.G. Hasko, H. Ahmed. *Microelectron. Eng.* 2002, **745**, 61.
18. Y. Nakamura, S. Takechi, Y. Tsurunaga, K. Fujino, Y. Ban. *Polym. preprints, Jpn.* 1987, **36** 2078.
19. T. Nishida, M. Notomi, R. Iga, T. Tamamura. *Jpn. J. Appl. Phys.* 1992, **31** 4508.
20. <http://www.allresist.com/ebeamresist-positiv-csar62-alternative-zep/>
21. M. Murata, T. Miura, Y. Yumoto, T. Ota, E. Kobayashi. *Google patents*, Number **5, 580, 695**, 1996.
22. H. Ito. *IBM J. Res & Dev.* 1996, **41**, 69.
23. A. Voigt, M. Heinrich, C. Martin, A. Llobera, G. Rius, G. Gruetzner, F. Perez-Murano. *Microelectron. Eng.* 2007, **84**, 1075.
24. M. Aktary, M.O. Jensen, K.L. Westra, M.J. Brett, M.R. Freeman. *J. Vac. Sci. Technol. B.* 2003, **21**, L5.
25. H. Wu, K.E. Gonsalves. *Adv. Funct. Mater.* 2001, **11**, 271.
26. R.A. Lawson, C.T. Lee, W. Yueh, L. Tolbert, C.L. Henderson. *Microelectron. Eng.* 2008, **85**, 959.
27. J.B. Yoo, S.-W. Park, H.N. Kang, H.S. Mondkar, K. Sohn, H.-M. Kim, K.-B. Kim, H. Lee. *Polymer.* 2014, **55**, 3599.
28. O. Nalamasu, E. Reichmanis, J.E. Hanson, R.S. Kanga, L.A. Heimbrook, A.B.F. Emerson. A. Baiocchi. *Polym. Eng. Sci.* 1992, **32**, 1565.
29. S.A. MacDonald, W.D. Hinsberg, H.R. Wendt, N.J. Clecak, C.G. Willson, C.D. Snyder. *Chem. Mater.* 1993, **5**, 348.
30. J. Kofler, K. Schmoltner, A. Klug, E.J.W. List-Kratochvil. *J. Micromech. Microeng.* 2014, **24** 095010.
31. S. V. Postnikov, M.D. Stewart, H.V. Tran, M.A. Nierode, D.R. Medeiros, T.



- Cao, J. Byers, S.E. Webber, C.G. Wilson. *J. Vac. Sci. Technol. B.* 1999, **17**, 3335.
32. M. Krysak, B. Jung, M.O. Thompson, C.K. Ober. *Proc. SPIE, Advances in Resist Materials and Processing Technology XXIX.* 2012, **8325**, 83250M.
33. K. Gonsalves, H. Wu. *Adv. Mater.* 2001, **13**, 195.
34. V. Singh, V.S.V. Satyanarayana, S.K. Sharma, S. Ghosh, K.E. Gonsalves. *J. Mater. Chem. C.* 2014, **2**, 2118.
35. T. Tada, T. Kanayama. Nanolithography using fullerene films as an electron beam resist. *Jpn. J. Appl. Phys.* 1996, **35**, L63.
36. J. Manyam. *Novel Resist Materials for Next Generation Lithography.* (Doctoral Dissertation). University of Birmingham. 2010.
37. F.P. Gibbons, A.P.G. Robinson, R.E. Palmer, M. Manickam, J. A. Preece. *Small*, 2006, **2**, 1003.
38. H. Okamura, T. Takemura, M. Tsunooka, M. Shirai. *Polym. Bull.* 2004, **52**, 381.
39. H. Okamura, D.C. Forman, C.K. Ober. *Polym. Bull.* 2014, **71**, 2395.
40. H.S. Choong, F.J. Kahn. *J. Vac. Sci. Technol.* 1981, **19**, 1121.
41. D. X. Yang, A. Frommhold, X. Xue, R. E. Palmer, A. P. G. Robinson. *J. Mater. Chem. C.* 2014, **2**, 1505.
42. I. Takemoto, Y. Fuji, I. Yoshida, K. Hashimoto, T. Miyagawa, S. Yamaguchi, K. Takahashi, S. Konishi, Y. Lee. *J. Photopolym. Sci. Technol.* 2005, **18**, 3.
43. J. Manyam, A. Frommhold, D.X. Yang, A. McClelland, M. Manickam, J.A. Preece, R.E. Palmer, A.P.G. Robinson. *Proc. SPIE, Advances in Resist Materials and Processing Technology XXIX.* 2012, **8325**, 83251U.

44. I. Haller, M. Hatzakis, R. Srinivasan. *IBM. J. Res. Dev.* 1968, **12**, 251.
45. W. Hu, G.H Bernstein, K. Sarveswaran, M. Lieberman. *IEEE-NANO. Third IEEE Conference.* 2003, **2**, 602.
46. M.A. Mohammad, K. Koshelev, T. Fito1, D.A. Z. Zheng, M. Stepanova, S. Dew. *Jpn. J. Appl. Phys.* 2012, **51**, 06FC05.
47. Stephen Thoms, D.S. Macintyre. *J. Vac. Sci. Technol. B.* 2014, **32**, 06FJ01.
48. M. Schirmer, B. Büttner, F. Syrowatka, G. Schmidt, T. Köpnick, C. Kaiser. *Proc. SPIE, 29th European Mask and Lithography Conference.* 2013, **88860**, 88860D.
49. R.G. Hobbs. *Semiconductor nanowire fabrication via bottom-up & top-down paradigms.* (Doctoral Dissertation). University College Cork. 2011.
50. H. Namatsu, Y. Takahashi, K. Yamazaki, T. Yamaguchi, M. Nagase, K. Kurihara. *J. Vac. Sci. Technol. B.* 1998, **16**, 69.
51. J.K.W. Yanga, K.K. Berggren. *J. Vac. Sci. Technol. B.* 2005 **25**, 2025.
52. A.E. Grigorescu, M.C. van der Krogt, C.W. Hagen, P. Kruit. *Microelectron. Eng.* 2007, **84**, 822.
53. J. Stowers, D.A. Keszler. *Microelectron. Eng.* 2009, **86**, 730.
54. D.C. Joy, S. Luo. *Scanning.* 1989, **11**, 176.
55. D.J. Webb, M. Hatzakis. *J. Vac. Sci. Technol.* 1979, **16**, 2008.
56. A.S. Abbas, S. Alqarni, B.B. Shokouhi, M. Yavuz. B. Cui. *Mater. Res. Express.* 2014, **1**, 045102.
57. C. Con, R. Dey, M. Ferguson, J. Zhang, R. Mansour, M. Yavuz, B. Cui. *Microelectron. Eng.* 2012, **98**, 254.
58. S. Kim, B. Marelli, M.A. Brenckle, A.N. Mitropoulos, E.-S. Gil, K. Tsioris, H. Tao, D.L. Kaplan, F.G. Omenetto. *Nat. Nanotechnol.* 2014, **9**, 306.

59. F.G. Omenetto, D.L Kaplan. *Science*. 2010,**329**, 528.
60. S. Kim, A.N. Mitropoulos, J.D. Spitzberg, H. Tao, D.L. Kaplan, F.G. Omenetto. *Nature Photon*. 2012, **6**, 818.
61. S. Bhumiratana, W.L. Grayson, A. Castaneda, D.N. Rockwood, E.S. Gil, D.L. Kaplan, G. Vunjak-Novakovic. *Biomaterials*. 2011, **32**, 2812.
62. W. Chen, H. Ahmed. *Appl. Phys. Lett*. 1993, **62**, 1499.
63. E.-H. Lee, S.-G. Lee, O Beomhoan, S.-K. Kim. *Proc. SPIE, Optoelectronics, Materials and Devices for Communications*. 2001, **4580**, 263.
64. S. Stepanow, M. Lingenfelder, A. Dmitriev, N. Lin, Th. Strunskus, Ch. Wöll, J.V. Barth, K. Kern. *BESSY – Highlights 2003 – Scientific Highlights*. 2003.
65. C.T. O'Mahony, R.A. Farrell, T. Goshal, J.D. Holmes, M.A. Morris in *The Thermodynamics of Defect Formation in Self-Assembled Systems, Thermodynamics - Systems in Equilibrium and Non-Equilibrium*. 2011, Chapter 13.
66. C. Tang, E.M. Lennon, G.H. Fredrickson, E.J. Kramer, C.J. Hawker. *Science*. 2008, **322**, 429.
67. T. Thurn-Albrecht, J. Schotter, G.A. Kästle, N. Emley, T. Shibauchi, L. Krusin-Elbaum, K. Guarini, C.T. Black, M.T. Tuominen, T.P. Russell. *Science*. 2000, **290**, 2126.
68. S.O. Kim, H.H. Solak, M.P. Stoykovich, N.J. Ferrier, J.J. de Pablo, P.F. Nealey. *Nature*. 2003, **424**, 411.
69. K.W. Gotrik, C.A. Ross. *Nano Lett*. 2013, **13**, 5117.
70. P. Mokarain. Directed self-assembly of block copolymers: An alternative tool for sub020 nm lithography. *Intel ERIC Conference*. 2012.
71. F. S. Bates and G. H. Fredrickson. *Phys. Today*. 1999, **52**, 32.

72. M.C. Orilall, U. Wiesner. *Chem. Soc. Rev.* 2011, **40**, 520.
73. S.-J. Jeong, J.Y. Kim, B.H. Kim, H.-S. Moon, S.O. Kim. *Mater. Today.* 2013, **16**, 468.
74. S.-M. Park, X. Liang, B.D. Harteneck, T.E. Pick, N. Hiroshiba, Y. Wu, B.A. Helms, D.L. Olynick. *ACS Nano.* 2011, **5**, 8523.
75. I. Bitá, J.K.W. Yang, Y.S. Jung, C.A. Ross, E.L. Thomas, K.K. Berggren. *Science.* 2008, **321**, 939.
76. Y.S. Jung, C.A. Ross. *Nano Lett.* 2007, **7**, 2046.
77. R. Ruiz, H. Kang, F.A. Detcheverry, E. Dobisz, D.S. Kercher, T.R. Albrecht, J.J. de Pablo, P.F. Nealey. *Science.* 2008, **321**, 936
78. C. T. Black, R. Ruiz, G. Breyta, J.Y. Cheng, M.E. Colburn, K.W. Guarini, H.-C Kim, Y. Zhang. *IBM J. Res. Develop.* 2007, **51**, 605.
79. C. T. Black. *ACS Nano.* 2007, **1**, 147.
80. S.K. Thanawala, M.K. Chaudhury. *Langmuir.* 2000, **16**, 1256.
81. A. Nunns, J. Gwyther, I. Manners. *Polymer.* 2013, **54**, 1269.
82. G. von Freymann, A. Lidermann, M. Thiel, I. Staude, S. Essig, K. Busch, M. Wegener. *Adv. Funct. Mater.* 2010, **20**, 1038.
83. E. Buitrago, M. F.-B. Badia, Y.M. Georgiev, R. Yu, O. Lotty, J.D. Holmes, A.M. Nightingale, H.M. Gueria, A.M. Ionescu. *Sensors Actuat. B Chem.* 2014, **199**, 291.
84. C.M. Soukoulis, M. Wegener. *Nat. Photonics.* 2011, **5**, 523.
85. J. Vila-Comamala, S. Gorelick, V.A. Guzenko, C. David. *J. Vac. Sci. Technol. B.* 2011, **29**, 06F301.
86. L.T. Varghese, L. Fan, J. Wang, Y. Xuan, M. Qi. *Small.* 2013, **9**, 4237.
87. D.M. Tanenbaum, A. Olkhovets, L. Sekaric. *J. Vac. Sci. Technol. B.* 2001,

**19**, 2829.

88. T. Osipowicz, J.A van Kan, T.C Sum, J.L Sanchez, F. Watt. *Nucl. Instr. Meth. Phys. Res.* 2000, **161-163**, 83.

89. F. Watt, A.A. Bettiol, J.A. Van Kan, E.J. Teo, M.B.H. Breese. *Int. J. Nanosci.* 2005, **04**, 269.

90. W.-D. Li, W. Wu, R.S. Williams. *J. Vac. Sci. Technol. B.* 2012, **30**, 06F304.

91. M. Isaacson, A. Muray, M. Scheinfein, A. Adesida, E. Kratschmer. *Microelectron. Eng.* 1984, **2**, 58.

92. M. Angelopoulos, N. Patel, J.M. Shaw, N.C. Labianca, S.A. Rishton. *J. Vac. Sci. Technol. B.* 1993, **11**, 2794.

## CHAPTER 2

---

# EQUIPMENT AND EXPERIMENTAL

## **2. EQUIPMENT AND EXPERIMENTAL**

This chapter describes the tools and the experimental techniques employed to undertake the research defined in this thesis. To begin with, all the equipment utilised will briefly be defined. Most of these tools are common to all the experiments that were carried out in this research, unless stated. It is followed by a discussion of the experiments performed to analyse the work. Firstly, the processing of positive electron beam lithography (EBL) resists SML, ZEP and polymethyl methacrylate (PMMA) will be discussed. Subsequently, patterning of Ge with the negative hydrogen silsesquioxane (HSQ) resist is outlined, followed by the methodology employed for the directed self-assembly (DSA) of block copolymers (BCPs) on Si and Ge surfaces.

### **2.1. PHYSICAL TOOLS**

In this Section, all the major tools such as the EBL, etchers and other characterisation tools are discussed in details. The use of these electronic equipment recurrently appear in all the works described in this thesis.

#### **2.1.1. Electron Beam Lithography System**

EBL is a widely used top-down nanofabrication tool, which permits the creation of high-resolution features of arbitrary layout. The EBL technique involves directly exposing an electron-sensitive resist to a beam of high energy electrons without the requirement for a mask, it is therefore a mask-less lithography. As highlighted in Chapter 1, the lithographic resolution of any resist is extensively governed by various resist, development and tool related factors. An EBL system contains an electron gun which sources the electrons through a high vacuum electron column,

which further shapes the emitted electrons into a highly focused beam. The column contains electromagnetic lenses, which can reduce the beam size up to  $1/10^{\text{th}}$  of the original beam size and align the beam with the centre of an optical axis.<sup>1</sup> In the research described in this thesis, EBL exposures were performed on a Raith e-Line Plus EBL system, which is equipped with a thermal field emission (TFE) filament gun and has a maximum voltage of 30 kV. The voltage typically employed in the work described in this thesis was 10 kV. For certain resolution requirements voltages of 1 and 30 kV were also used. High-resolution structures were at all times written with a beam spot size of 2 nm within a 100  $\mu\text{m}$  write-field size. In order to determine the contrast curves of the positive resists, 50 kV exposures were carried out on a JOEL JBX 6000FS system. This EBL tool is equipped with a TFE electron gun with a ZrO/W emitter and operated at a maximum voltage of 50 kV. This system was particularly used for obtaining contrast curves of SML resist, which is analysed in Chapter 3 of this thesis.

### 2.1.2. Pattern Transfer Tools

To create nanostructures on a substrate, the EBL exposed surfaces are subjected to pattern transfer processes such as etching and metallisation.<sup>2,3</sup> A schematic representation of both the pattern transfer processes, i.e. (a) etching and (b) metallisation, after EBL procedure (and any lithographic procedure) is outlined in Figure 2.1.



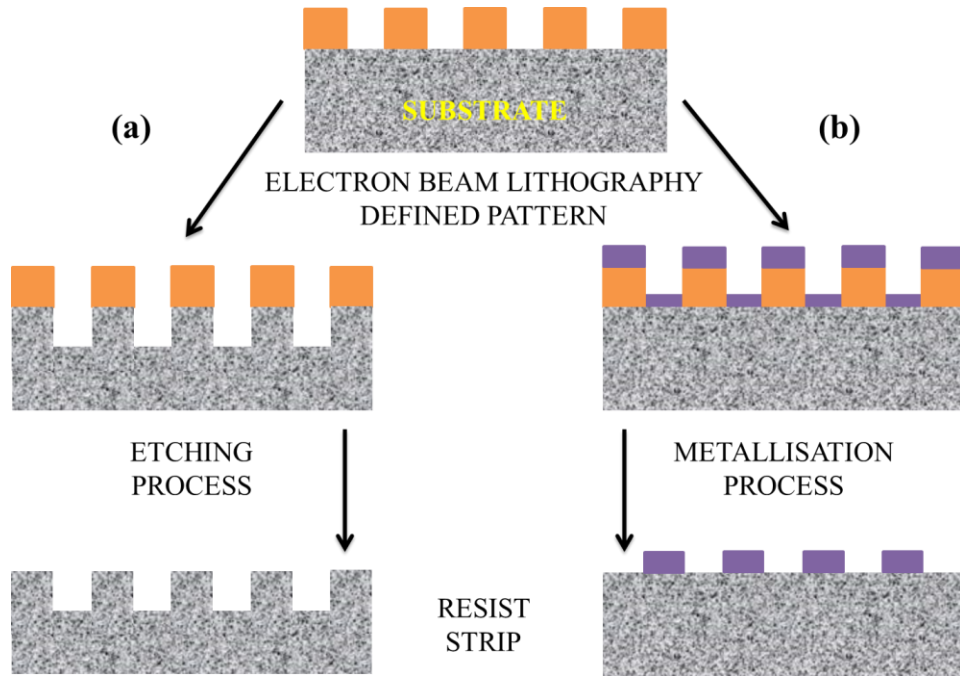


**Figure 2.1.** Schematic representation of two pattern transfer processes, etching and metallisation, that follow the EBL process

#### 2.1.2.1. Pattern Transfer with Etching Technique

Figure 2.1 typically summaries a lithography process achieved with a positive resist. Trenches or depths, after exposure and development, are created in the resist. Process (a) illustrates the etching technique, which can be described as a pattern transfer process realized by chemical/physical removal of the substrate material—often in a pattern defined by a protective resist layer.<sup>3</sup> In this case, lithographic resists must display a high etch resistance to the etchants, as this process involves the use of ions (dry etch) or chemicals (wet etch) to consume non-resist protected areas. The etch tools used in this study were a Surface Technology Systems (STS) Inductively Coupled Plasma (ICP) Etcher (Multiplex ICP) and an Oxford Instruments Plasmalab 100 ICP etching system. The STS system was used to etch through positive resists using a sulphur hexafluoride ( $\text{SF}_6$ ) and octafluorocyclobutane ( $\text{C}_4\text{F}_8$ ) gas mixture. The system has two different RF

generators: one to generate and control the plasma density by direct connection to the antenna coil and another to adjust and control the energy of the ions by connecting it to the substrate holder. The deposition of the passivation ( $C_4F_8$ ) layer and etching, ( $SF_6$ ) are alternated in the silicon etch process, as shown in Figure 2.2.<sup>4</sup> The  $C_4F_8$  gas deposits a  $(C_xF_y)_n$  polymeric layer on the surface protecting it except on the base of a pattern (Figure 2.2). Whereas, the  $SF_6$  gas can selectively etch only Si or Ge surface and will not heavily affect SML, ZEP or PMMA resists.

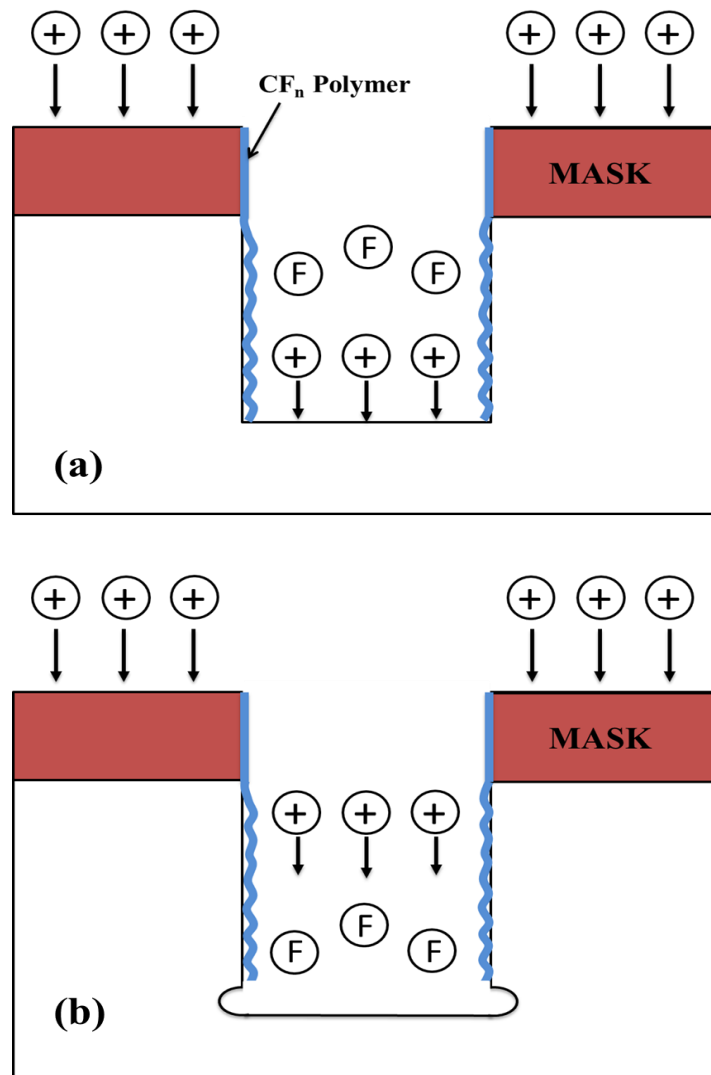


**Figure 2.2.** A schematic representation of the etching sequence by  $C_4F_8$  and  $SF_6$  where alternative (a) deposition of passivation layer and (b) etching process takes

*place in Si etch.*<sup>4</sup>

Thus when the SF<sub>6</sub> gas is passed it etches away the ‘unprotected’ resist areas.<sup>5</sup> This etch chemistry was predominantly used in the study carried out in Chapter 3 and Chapter 5. The Oxford Instrument etcher was used in reactive ion etching (RIE) mode with a chlorine (Cl<sub>2</sub>)-based etch recipe for samples processed with the HSQ resist, which is used in study described in Chapter 4 and Chapter 5. The Cl ions etch away only ‘resist-unprotected’ areas of a substrate, *e.g.* Si or Ge, since HSQ is reported to be resistant to Cl based etch chemistry.<sup>6</sup> The process parameters used for the RIE were: Cl<sub>2</sub> flow rate of 30.0 SCCM, 10 mTorr working pressure, 20 °C temperature with different etch times.

### **2.1.2.2. Pattern Transfer with Metal Lift-Off Technique**

Metallisation followed by metal ‘lift-off’, is an additive process as opposed to etching, which is a subtractive process. The metallisation process consists of depositing a metal film, *e.g.* Al, Ni, Cu or Cr, on EBL defined substrates by methods such as thermal evaporation or sputtering deposition. As seen in Figure 2.3, an inverse pattern is firstly created by EBL in a positive resist. After the resist development, a desired metal material is deposited on all the areas of the lithography defined substrates including the areas free of the resist material, as shown in Figure 2.3. The substrate is then submerged in solvents that can dissolve the resist materials, such as Microposit 1165 or acetone solvents used to perform a Cr metal lift-off on SML or ZEP resists nano-patterns in Chapter 3. The resist is thus lifted-off from the substrate by the solvents, leaving the metal in the targeted areas. Consequently, an inverse pattern of the one defined by EBL is obtained on the substrate. Metallisation

can be used to situate metal contacts for nanodevices or to produce a metal hard mask for further substrate etching.<sup>7</sup> The metallisation tool used for the research described in this thesis was a Temscale FC2000 electron beam evaporation system.

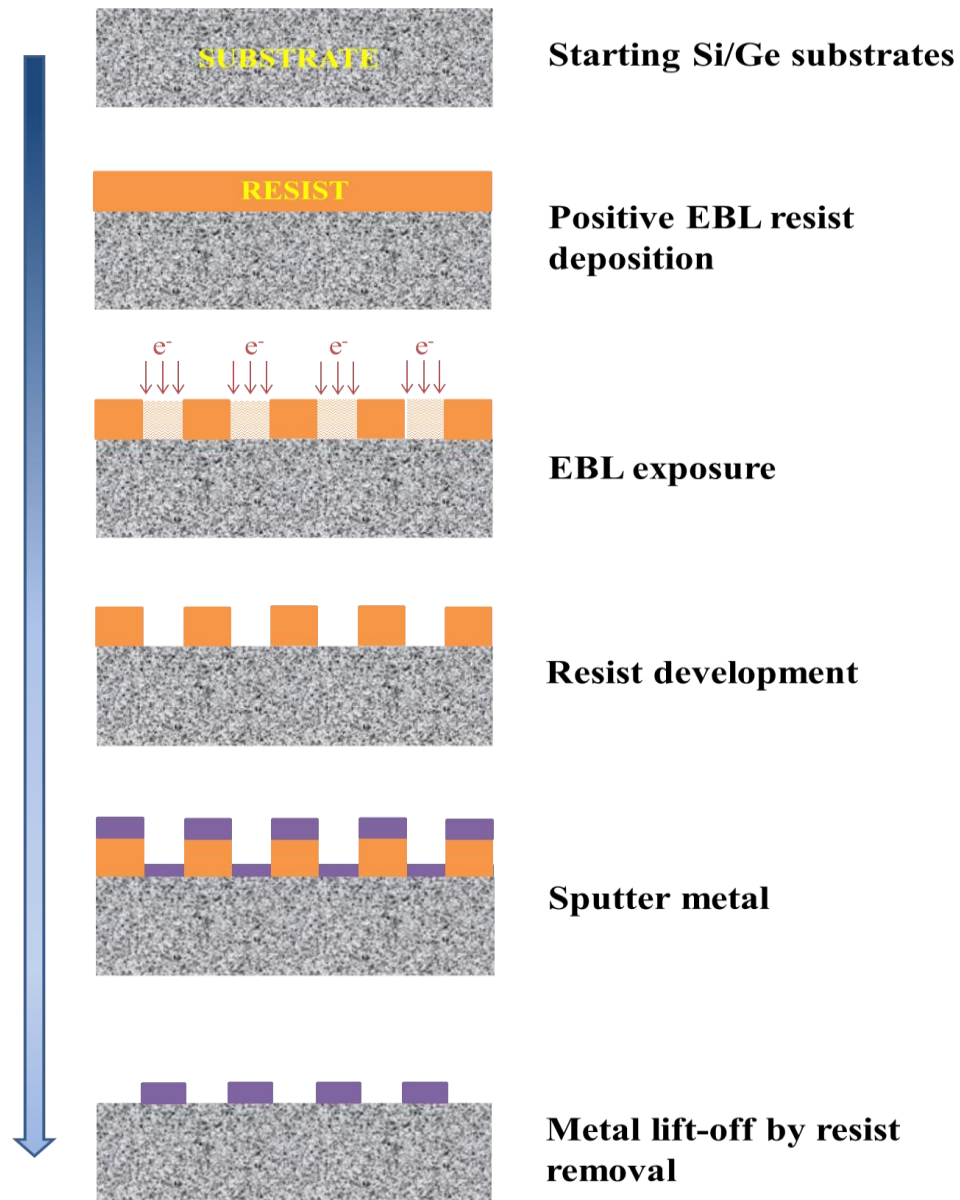


**Figure 2.3.** Process flow describing the EBL exposure of a positive resist followed by metal deposition and subsequent metal lift-off by resist removal.

### 2.1.3. Scanning Electron Microscope

Scanning electron microscopes are capable of imaging nanoscale structures, typically

down to 5-10 nm, by rastering a highly focused electron beam over a substrate of interest. A surface image is generated due to the interaction of the electrons with the substrate. The signals from the back-scattered primary electrons, or the generated secondary electrons, after interacting with the surface are collected by an electron detector, which generates the scanning electron microscopy (SEM) image. The intensity of the back-scattered or secondary electrons depends on the topology and chemical composition of the substrate, generating both topological and material contrasts of the image. In the research described in this thesis, standard SEM imaging was carried out on a Raith e-Line Plus tool at a characteristic voltage of 10 kV. For higher resolution structures, a FEI Helios NanoLab 600 system with a high resolution Elstar™ Schottky field-emission scanning electron microscope and a Sidewinder focused ion beam (FIB) column was employed at a typical voltage of 5 kV. Both the imaging tools were used throughout the research accounted in this thesis.

### 2.1.4. Surface Profiler

A Veeco DEKTAK surface profilometer was used to measure the step height and film thicknesses for contrast curve measurements of all the resists, which are assessed in Chapter 3. This tool uses a diamond-tipped stylus which is placed at a 90° angle on the substrate. The stylus then scans the surface in a line and a 1-dimension topographical plot is obtained. The highest vertical resolution of the DEKTAK tool was about 2-5 nm. The step height for contrast curves as small as 2-3 nm was also determined by this tool. Due to its contact profiling application, the stylus can only be used over firm surfaces as softer materials can be damaged by the

stylus. The use of the Profilometer is sketched in Section 2.2.1 of this Chapter.

### 2.1.5. Fourier Transform Infrared (FTIR) Spectroscopy

Fourier transform infrared (FTIR) spectroscopy is a routine tool used in most chemistry laboratories to investigate the composition and quality of materials. An IR spectrum obtained of a compound represents the molecular fingerprint of the sample.<sup>7,8</sup> FTIR spectroscopy is a non-destructive analysis method where an infra-red beam of light is passed through a material. Absorption of the light depends on the vibrational and rotational transitions within the different functional groups. An FTIR spectrum for a material can therefore be readily obtained. The FTIR tool used in this study was a Thermo Scientific Nicolet 6700 FTIR spectrometer equipped with an attenuated total reflectance (ATR) accessory (Harrick Scientific). The FTIR spectra collected for the positive resists detailed in Chapter 3 were obtained between a wavenumber range of 650 - 4000  $\text{cm}^{-1}$  and in Chapter 4 between a wavelength range of 650 - 3500  $\text{cm}^{-1}$ . FTIR spectra obtained in Chapter 4 of this thesis were obtained by passivating the ATR crystal with acid solutions.

## 2.2. EXPERIMENTAL

The following Sections will detail the experimental work performed in each Chapter of the thesis. All the experiments were carried out using the physical tools mentioned in the previous Section 2.1. Firstly, in Section 2.2.1, the laboratory procedures of the evaluation of SML resist as an able EBL resist will be comprehended. Subsequently, the experiments performed to assess the competency of acids treatment on the

adhesion of HSQ resist to Ge surface are detailed in Section 2.2.2. In the Section 2.2.3, experiments pertaining directed self-assembly of BCPs within HSQ guided patterns are described.

### 2.2.1. Resists Characterisation

SML resists of three concentrations, *i.e.* SML 50, 100 and 300 used in this study were provided by EM Resist Ltd. The concentrations numbers define the film thickness of the resist achieved after spinning the resist at 4000 rpm for 60 s. The ZEP520A resist was purchased from Nippon ZEON Corporation and 950 K PMMA A7 from MicroChem Corporation. <100> oriented silicon pieces, 10 mm × 10 mm, were used throughout the experiments.

The three SML resists, 50, 100 and 300, were spin-coated onto the substrates at 4000 rpm for 60 s, to give films with a mean thickness of 50, 100 and 300 nm, respectively. The substrates were then soft-baked on a hot plate at 180 °C for 180 s prior to the exposure. PMMA substrates were processed in the same fashion. ZEP resist was also spin-coated at 4000 rpm, onto the substrates but soft-baked at 120 °C. All of the exposures were either performed using the Raith system, between the voltages of 10-30 kV, or the JEOL system at a voltage of 50 kV. Substrates coated with PMMA or SML resist were developed in a 7:3 isopropyl alcohol (IPA):water developer. ZEP was intentionally developed using ZED-N50 (n-amyl acetate), since attempts to employ the 7:3 IPA:water developer lowered its sensitivity up to 10 times.<sup>9</sup> All developments were 15 s long in the respective solvents, followed by a 15 s IPA rinse.

For generating resist contrast curves, an array of  $50\text{ }\mu\text{m} \times 100\text{ }\mu\text{m}$  rectangles was exposed on the substrates, with dose increments of  $1.75\text{ }\mu\text{C}/\text{cm}^2$  from  $0\text{ }\mu\text{C}/\text{cm}^2$  to  $300\text{ }\mu\text{C}/\text{cm}^2$ . Post exposure, the resist-coated substrates were developed using their appropriate developers. For cold temperature developments, all the developers and rinsing solvents were submerged in an ice-bath in a freezer until the temperature obtained was  $0\text{ }^{\circ}\text{C}$ . The step height in the resist was then measured using the Profilometer referred to above.

Gratings of single pixel lines spaced with pitch sizes of 30, 40, 60, 80, 100 and 200 nm were generated using SML, ZEP and PMMA resist having a film thickness of about 50 nm. The exposures were carried out at a 30 kV with a step size of 2 nm and a  $10\text{ }\mu\text{m}$  aperture size. The substrates were imaged on Raith or FEI Helios instruments at 10 kV or 5 kV, respectively. Prior to SEM inspection all of the substrates were coated with Au/Pd for smooth imaging.

For metal lift-off, 5 and 10 nm thick Cr films were deposited on SML and ZEP resists with high resolution gratings by electron beam evaporation, using the Temescal instrument. The lift-off was performed by immersing a substrate in a Microposit 1165 remover (Shipley) for 5 to 10 min at  $60\text{ }^{\circ}\text{C}$ . Each substrate was then washed under flowing deionised (DI) water and nitrogen dried prior to SEM imaging.

Etching tests were carried out using a STS etching system with a  $\text{SF}_6$  and  $\text{C}_4\text{F}_8$  gas mixture (Gas flow of  $\text{SF}_6 = 30\text{ sccm}$  and  $\text{C}_4\text{F}_8 = 90\text{ sccm}$ , Pressure = 15 mTorr, ICP = 600 W, RF = 15 W at  $10\text{ }^{\circ}\text{C}$ ).<sup>10</sup> In order to determine the etch rates of the SML,



ZEP and PMMA resists, ~300 nm thick films were spin-coated onto Si and etched for time intervals of 1, 3, 5 and 7 min; film thicknesses were measured by ellipsometer (M2000-Wollam). Identical high resolution gratings in SML and ZEP were etched using the same recipe for 1 min, since the gratings were written on 50 nm thick resists.

The line edge roughness (LER) of gratings (standard deviation of  $3\sigma$  for single lines) was determined by SEM analysis using *ImageJ* software. Process latitudes were acquired by exposing single pixel lines (60 nm pitch) on SML and ZEP resists within specific electron beam dose ranges and the linewidth was measured as a function of the dose. The surface roughness of the exposed and unexposed resists was measured by atomic force microscope (AFM) in tapping mode (Park systems, XE-100) under ambient conditions. To obtain infra-red spectra of SML, ZEP and PMMA resists, FTIR instrument was used.

### 2.2.2. Patterning Germanium with HSQ Resist

In order to quantify the patterning of Ge surface with HSQ resist, substrates of  $10 \times 10$  mm were diced from a p-doped Ge <100> and Ge-on-insulator (GeOI) wafers, purchased from Umicore and Soitec, respectively. The GeOI wafer consisted of a ~60 nm top Ge layer, a 150 nm of SiO<sub>2</sub> buried oxide (BOX) layer on a Si substrate. Each substrate was degreased by ultra-sonication in acetone and isopropyl alcohol (IPA) for 2 min each, followed by N<sub>2</sub> drying. Subsequently, the chips were rinsed under flowing DI water for approximately 10 s and immediately immersed in different acid solutions for various time intervals.

**Table 2.1.** Preparation of dilute acids by ratio proportions in DI water with their corresponding molarities and pH.

Concentration Ratio with 1 g/ml of citric acid/acetic acid	Citric acid		Acetic acid	
	Molarity (M)	pH	Molarity (M)	pH
1:1	5.20	1.37	16.52	1.77
1:3	1.73	1.45	5.55	2.01
1:7	0.74	1.64	2.35	2.19
1:12	0.43	1.76	1.387	2.31

Citric acid (Sigma) or acetic acid (Sigma) was dissolved in DI water to give various molar concentrations. As citric acid was available in solid form, whereas the acetic acid is in liquid form, the citric acid solutions were prepared by weight (w/v) and those of acetic acid by volume (v/v). Table 2.1 shows the molar concentrations and the pH of acid solutions prepared by dissolving in DI water in their particular ratios. The chips were then submerged in the appropriate solutions for time intervals of 3, 5 and 10 min. On removal of the chips from the solutions, they were dried with a N<sub>2</sub> gun and the HSQ resist was immediately spin-coated onto them. Ge chips immersed

in 1:1 and 1:2 concentrations of either acid were rinsed with DI water for 3-5 s to remove excess acids residue that was observed on the chips. A 2.4 wt. % solution of HSQ in methyl isobutyl ketone (MIBK) was spin-coated for 33 s at 2000 rpm on the chips, which resulted in the deposition of films about 50 nm thick. They were subsequently baked at 120 °C for 3 min in an ambient atmosphere. The baking step ensures removal of any excess MIBK solvent and increases the HSQ polymer size making it more sensitive to the electron-beam dose.<sup>11</sup>

All EBL exposures of the HSQ of Ge were carried out on Raith tool at 10 kV. 20 and 50 nm gratings with varied pitch sizes were exposed on the chips with a base dose of 700  $\mu\text{C}/\text{cm}^2$  and incrementing the dose by a factor of 0.15 in the successive patterns. Single pixel gratings were also exposed with pitch sizes ranging from 40 to 200 nm with varied doses in one set. All the sets of gratings were exposed with various electron beam doses, starting from 1000  $\mu\text{C}/\text{cm}^2$  at 10 kV and increased by a dose of 500  $\mu\text{C}/\text{cm}^2$  for the successive set; up to 3000  $\mu\text{C}/\text{cm}^2$ . After the exposures, the chips were developed in salty developer, *i.e.* by immersing them in a mixture of 0.25 M NaOH and 0.7 M NaCl for 15 s, followed by a 60 s rinse in DI water. They were lastly dipped in pure IPA for 15 s and dried with  $\text{N}_2$ . HSQ is a negative resist and therefore when developed, the unexposed resist will dissolve in the solvent. HSQ is known to develop in strong aqueous base solvents like tetramethylammonium hydroxide (TMAH) and NaOH/NaCl mixture.<sup>12</sup>

The reaction mechanism proposed in a study by J. Kim *et. al.* for development of HSQ in salty developers is outlined in Figure 2.3.<sup>13</sup> The Si-H bonds in the HSQ

network is attacked by the nucleophilic  $\text{OH}^-$  from the water molecules resulting into the formation of  $\text{Si-OH}$  bonds and the release of hydrogen gas. The release of hydrogen gas is noticeable while developing HSQ films in the developer solution. The resultant formation of  $\text{Si-O}$  linkages can be deprotonated to form sodium silicon oxide. The cations from the salt can co-ordinate with the lone pair of electrons on oxygen and weaken the  $\text{Si-O}$  bond, enhancing the solubility of HSQ in the developer.

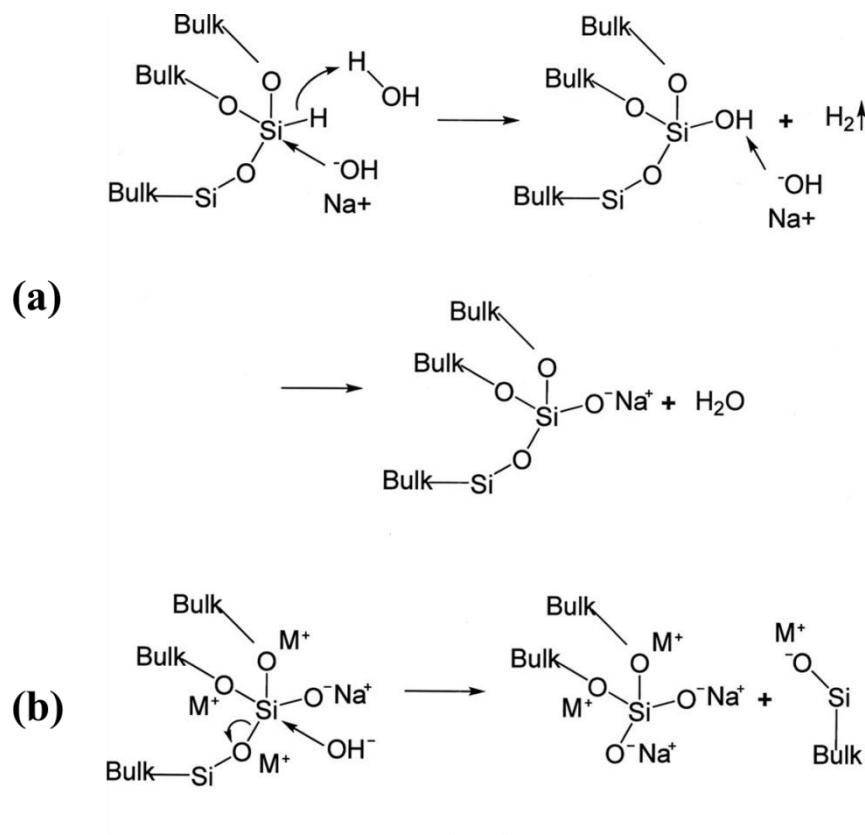


**Figure 2.3.** (a) Proposed mechanism for  $\text{H}_2$  evolution from HSQ after development in salty developer. (b) Proposed dissolution mechanism of HSQ in base with salts.  $\text{M}^+$  is a salt cation.<sup>13</sup>

The substrates designated for etching were placed in Oxford Instruments Plasmalab 100 for  $\text{Cl}_2$  RIE to transfer the HSQ structures into the underlying Ge substrate. The

process parameters used for the RIE are as described in Section 2.1.2 with an etch time of 25 s. SEM imaging of all the resulting chips was performed on the EBL instrument. ATR-FTIR of acid passivated Ge was carried out on the FTIR spectrometer. XPS spectra were collected on a Thermo Electron K-Alpha spectrometer using a monochromatic Al K $\alpha$  X-ray source (1486.6 eV). Spectra were referenced to the C 1s at 284.8 eV.<sup>14</sup> The XPS spectra were processed using a Shirley background correction followed by peak fitting to Voigt profiles.<sup>14</sup> The Ge 3d doublets were fit to Gaussian-Lorentzian profiles with an intensity ratio of 3:2 and a spin-orbit splitting of 0.585 eV.<sup>14</sup> The S 2p components from 100 scans were fitted to a doublet with a branching ratio of 0.5 and spin-orbit splitting of 1.2 eV.<sup>14</sup>

### 2.2.3. Directed Self-Assembly Of Block Copolymers on Si and Ge Surfaces

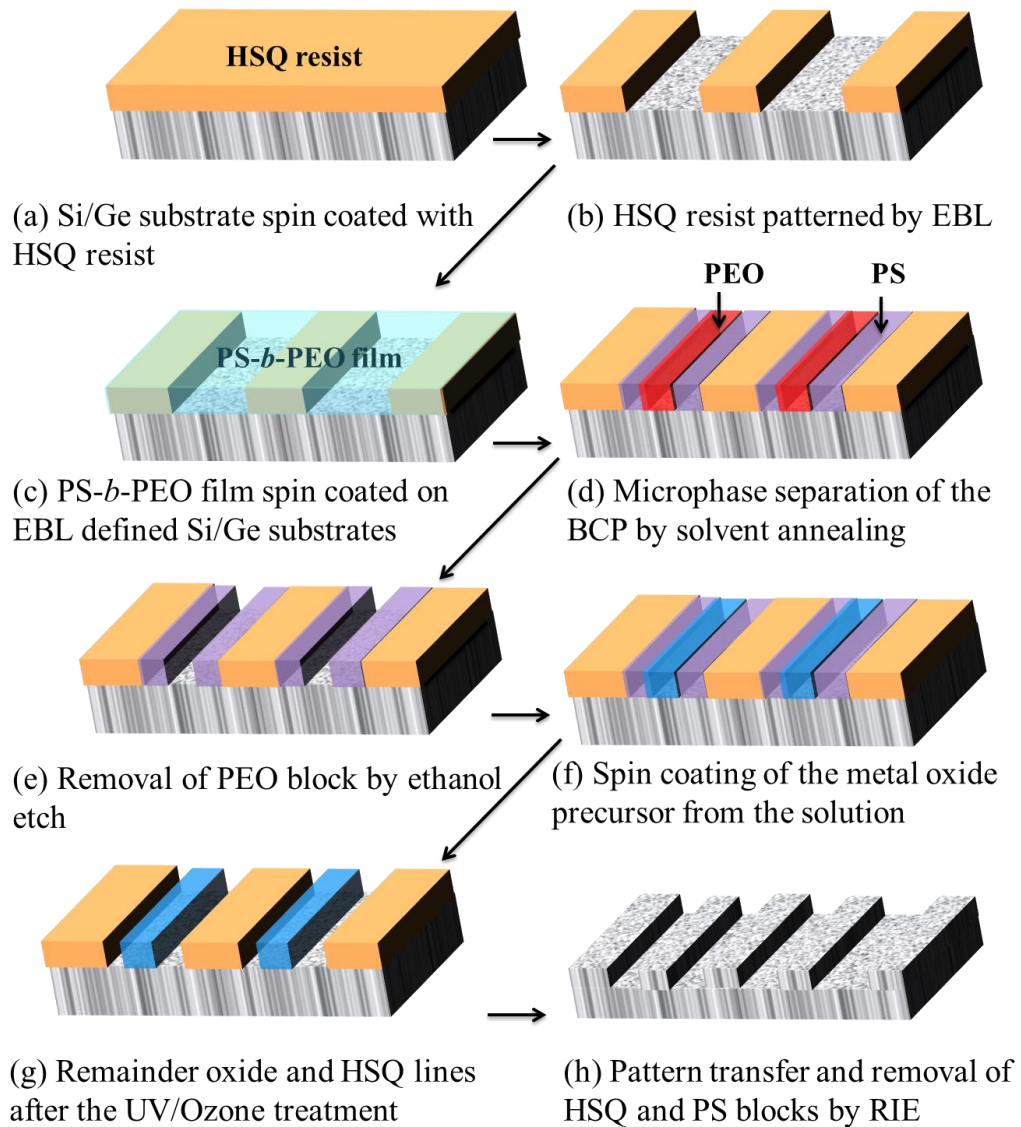


**Figure 2.4.** Schematic representation of the process-flow graphoeptaxy using the diblock copolymer PS-b-PEO. (a) Si or Ge substrates, (b) Template formation by EBL, (c) BCP deposition, (d) Solvent annealing of the BCP film, (e) Ethanol etch of PEO block. (f) Iron inclusion, (g) UV/Ozone treatment for forming iron hardmask, (h) RIE of Si/Ge through the iron hardmask and HSQ template.

Figure 2.4 represents a schematic of the graphoeptaxy process in which the diblock copolymer polystyrene-*block*-polyethylene dioxide (PS-*b*-PEO) is processed on a

substrate surface. Si or Ge substrates of 10 ×10 mm were diced from a <100> orientation Si or Ge wafer, respectively and used throughout the experiment. The substrates were firstly degreased by ultra-sonication in acetone and subsequently in isopropyl alcohol (IPA) for 120 s. The Si substrates were dried with a N<sub>2</sub> gun and then by baking at a temperature of 120 °C for 180 s. They were then patterned using the HSQ high-resolution EBL resist. A 2.4 wt % solution of HSQ in MIBK was spin-coated onto a Si substrate a 2000 rpm for 33 s to give a thin film resist thickness of approximately 50 nm (see Figure 2.4(a)). After spin coating, the substrate was baked at a temperature of 120 °C for 180 s on a hotplate prior to EBL (Raith e-Line Plus) exposure. Arrays of 50 nm wide lines were exposed at 10 kV having pitch sizes of (45n+50) where 0 < n <7. After the EBL exposure, the substrates were developed by immersion in an aqueous mixture of 0.25 M NaOH, 0.7 M NaCl for 15 s, followed by a 60 s rinse in DI water and then 15 s dip in IPA solution. Subsequently, the substrates were blown dry in flowing N<sub>2</sub> gas. Thus, high-resolution HSQ gratings were achieved (see Figure 2.4(b)). In the case of Ge substrates, after the IPA and acetone cleaning they were processed in a different way prior to EBL patterning. Due to the presence of the native oxides on the Ge surface, each substrate was passivated using the method described in Section 2.2 of this Chapter. HSQ resist was spin-coated on the Ge substrates and administered in the same manner as detailed above.

PS-*b*-PEO powder (Polymer Source) was dissolved in toluene at room temperature and aged for 12 h to prepare a 0.4 % solution. The molecular weight ( $M_n$ ) of the BCP was PS = 42 kg/mol, and PEO = 11.5 kg/mol,  $M_w/M_n = 1.07$ , where  $M_w$  is the weight-average molecular weight. Thin films of BCP were deposited on the Si chips

by spin-coating the polymer solution with 3000 rpm for 30 s (Figure 2.4(c)). The chips were then placed in a jar and exposed to toluene vapour. The films were annealed for various time periods at 50 or 60 °C to induce mobility and commence microphase separation (see Figure 2.4(d)). After the solvent annealing, the Si chips were immersed in ethanol solution for 15 h at 40 °C, resulting in partial modification of one of the BCP blocks, *i.e.* the PEO block (Figure 2.4(e)). For the fabrication of the metal oxide hardmask, different concentrations of iron (III) nitrate nonahydrate ( $\text{Fe}(\text{NO}_3)_3 \cdot 9\text{H}_2\text{O}$ ) were dissolved in anhydrous ethanol and was spin-coated onto the patterned substrates (Figure 2.4(f)). The substrates were subsequently subjected to uv/ozone oxidation (PSD Pro Series Digital UV Ozone System; Novascan Technologies, Inc., USA) to oxidise the metal and form an iron oxide hard ( $\text{Fe}_2\text{O}_3$  (majorly) and  $\text{Fe}_3\text{O}_4$ ) mask on the substrates (see Figure 2.4(g)).

These iron oxide nanopattern arrays were used as a hard mask for pattern transfer to the substrate using the STS system (Figure 2.4(h)).<sup>15,16</sup> A double etching process was used to, firstly, etch the native silica layer and, secondly, the Si itself, in the case of Si substrates. During etching, the sample was thermally bonded to a cooled chuck (10 °C) with a pressure of 9.5 mTorr. For the oxide layer etch, the process parameters were optimised to a  $\text{C}_4\text{F}_8/\text{H}_2$  gas mixture (21 sccm/30 sccm). The silica etch time was kept constant (5 s) for all the samples. For Si etching, the process used a controlled gas mixture of  $\text{C}_4\text{F}_8/\text{SF}_6$  at flow rates of 90 sccm/30 sccm respectively and the ICP and RIE powers were set to 600 and 15 W respectively, at a chamber pressure of 15 mTorr. Likewise, in the case of Ge, STS etcher was used to transfer the metal oxide nanowire mask pattern to the underlying GeOI/Ge substrate.



CF<sub>4</sub> was used for etching Ge with the metal oxide nanowires as etch masks. Samples were etched for 9 s in total with CF<sub>4</sub> gas only using a flow rate of 40 sccm, pressure of 10 mTorr, and ICP power of 400 W. SEM imaging of the substrates at various steps was carried out at 10 kV and 5 kV. TEM samples were sectioned in the FEI Helios Nanolab 600i system. TEM imaging was carried out on JOEL 2100 TEM with EDX.

### 2.3. BIBLIOGRAPHY

1. C.S. Wu, Y. Makiuchi, C. Chen, in *Lithography*, ed. M. Wang, Intech, Vukovar, 2010, pp. 241-266.
2. A. Gangnaik, Y.M. Georgiev, J.D. Holmes. *Microelectron. Eng.* 2014, **123**,126.
3. Mark J. Madou in *Fundamentals of Microfabrication: The Science of Miniaturization*. 2001, pp 77-118.
4. J. Bhardwaj, H. Ashraf, A. McQuarrie. Presented at the *The Symposium on Microstructures and Microfabricated Systems at the Annual Meeting of the Electrochemical Society*, Montreal, Quebec, Canada. May 4-9, 1997.
5. J.K. Bhardwaj, H. Ashraf. *Proc. SPIE Micromachining and Microfabrication Process Technology*, 1995, **2639**, 224.
6. D. Park, T.H. Stievater, W.S. Rabinovich, N. Green, S. Kanakaraju, L.C. Calhoun. *J. Vac. Sci. Technol. B*. 2006, **24**, 3152.
7. D.W. Widmann. *IEEE J. Solid-State Circuits*. 1976, **11**, 466.
8. Z. Movasaghi, S. Rehman, I. Rehman. *Appl. Spectrosc.* 2002, **43**, 134.

Thermo Nicolet - Introduction to Fourier Transformation Infrared Spectrometry. <http://mmrc.caltech.edu/FTIR/FTIRintro.pdf>

9. M.A. Mohammad, S.K. Dew, M. Stepanova. *Res. Lett.* 2013, **8**, 139.
10. R.A. Farrell, N. Petkov, M.T. Shaw, V. Djara, J.D. Holmes, M.A. Morris, *Macromolecules*. 2010, **43**, 8651.
11. W. Henschel, Y.M. Georgiev, H. Kurz. *J. Vac. Sci. Technol. B.* 2003, **21**, 2018.
12. R.G. Hobbs, M. Schmidt, C.T. Bolger, Y.M. Georgiev, P. Fleming, M.A. Morris, N. Petkov, J.D. Holmes. *J. Vac. Sci. Technol. B*, 2012, **30**, 041602.
13. J. Kim, W. Chao, B. Griedel, X. Liang, M. Lewis, D. Hilken, D. Olynick. *J. Vac. Sci. Technol. B*, 2009, **27**, 2628.
14. G. Collins, D. Aureau, J.D. Holmes, A. Etcheberry, C. O'Dwyer. *Langmuir*. 2014, **30**, 14123.
15. T. Ghoshal, M.T. Shaw, C.T. Bolger, J.D. Holmes, M.A. Morris. *J. Mater. Chem.* 2012, **22**, 12083.
16. T. Ghoshal, T. Maity, R. Senthamaraikannan, M.T. Shaw, P. Carolan, J.D. Holmes, S. Roy, M.A. Morris, *Sci. Rep.* 2013, **3**, 2772.

## CHAPTER 3

---

# SML RESIST CHARACTERISATION

### 3. SML RESIST CHARACTERISATION

Advances in top-down nanofabrication have been a continual effort to generate high-resolution circuit elements, which are typical of today's integrated circuits.<sup>1</sup> To achieve extremely small feature sizes, nanolithography techniques like electron beam lithography (EBL), nanoimprint lithography (NIL) and ion beam lithography (IBL) are currently the most common choices in research and development, as highlighted in Chapter 1, Section 1.2 of this thesis. EBL is undoubtedly the favourite tool for lithography as it is a direct write method, more flexible as compared to NIL and much more mature than IBL, and has a very high resolution as the electron beam can stay well focused below a 10 nm beam size.<sup>2</sup> Continuous advances are being made to improve the resolution of the EBL technique and the main inclination is also towards developing ultra-high resolution resists. Poly methyl methacrylate (PMMA) is a simple, positive tone and still a dominant EBL resist. However, chiefly under special conditions PMMA is able to produce extremely high resolution structures. Sub-5 nm wide lines have been reported using PMMA with EBL voltages of 80-100 kV.<sup>3,4</sup> Such resolution is however, unobtainable at lower voltages like 10-30 kV. Another positive tone resist that has gained popularity due to its superiority over PMMA, in terms of sensitivity, is ZEP resist. This resist is structurally similar to PMMA except the side group which is substituted with a chlorine atom and phenyl group.<sup>5</sup> In addition to a superior sensitivity and resolution, ZEP resist has been reported to have higher plasma etch durability for C<sub>2</sub>F<sub>6</sub> and SF<sub>6</sub> gases.<sup>5</sup> The widespread use of ZEP lags behind PMMA because it is more expensive than PMMA.

Besides the properties of the resist material itself, the lithographic performance of any electron beam resist is affected by various factors such as electron energy, resist thickness, substrate material, developers, development time and temperature, as described in Chapter 1, Section 1.3 of this thesis. To extract prime performance from any resist, various resolution enhancement practices are constantly being employed. The line edge roughness (LER) of patterns is recognised as a non-tool related limiting factor of a resist's resolution.<sup>6</sup> LER arises mainly due to the initial coarseness of the resist materials and the effects become dominant below 50 nm; hindering the sharpness and stability of the nanostructures produced. At such a small scale the surface (side wall) roughness arises due to the size of the resist polymer molecules (molecular weight) and molecule aggregates. These granular aggregates eventually determine the quality of structures and the resolution of the resists.<sup>6,7</sup> During electron beam exposure, the proximity effect (see Chapter 1, Section 1.3.4 of this thesis) will cause the close regions to receive a small dose. These regions will be only partially developed and thus give rise to the LER. At a narrow spacing, such as 5-10 nm in positive resists, short-range intermolecular forces between the exposed and unexposed polymer may obstruct the exposed molecules in this region from dissolving in the developer solution<sup>8</sup> accounting for irregularities in the edges of fine structures. Many previous experiments and simulations have shown that roughness also arises during the development process of the resist features.<sup>9,10</sup> Use of ultra- or mega-sonication during development assists the polymer molecules to overcome the intermolecular forces and dissolve in the developer solution.<sup>8,11</sup> The use of a 7:3 isopropyl alcohol (IPA):water developer over the conventional 1:3 methyl isobutyl ketone (MIBK):IPA developer has shown to reduce the LER of polymethyl methacrylate (PMMA) greatly.<sup>12</sup> High-resolution

HSQ resist also suffers LER issues. Being a negative resist, HSQ forms aggregates of polymer molecules, which governs the roughness of structures produced.<sup>6,7</sup>

In this chapter, various properties of a new EBL resist produced by EM Resist Ltd. (Macclesfield, UK), named SML, are reported. SML is a positive tone organic resist that has been formulated to have similar processing properties as PMMA, but with enhanced performance.

As described in Chapter 1, Section 1.3.1 of this thesis, in order to characterise a resist, contrast curves have to first be analysed to obtain the optimum working conditions for any resist. Thus, for the current study the contrast curves were obtained for different thicknesses of SML that were developed at room temperature and 0 °C. The temperature dependence of lithographic resolution was also highlighted in Chapter 1, Section 1.3.3 of this thesis: for a positive resist, lowering the temperature of a developer significantly affects the sensitivity and contrast of the resist. An initial study on SML has shown that the 7:3 IPA:water co-solvent developer provides the highest contrast-to-sensitivity ratio compared to other resist developers.<sup>14</sup> Hence, the developer employed in this study was 7:3 IPA:water. A comparison of the sensitivity, contrast, resolution, etch resistance and lift-off proficiency between the widely used positive resists, ZEP 520A and PMMA, and SML is detailed in this Chapter. The study was extended on the surface roughness of the new resist and its effect on the lithographic resolution of SML. Firstly, the variation in surface roughness of SML and ZEP with respect to electron dose was determined. The LER of SML and ZEP were obtained from SEM images of high-

resolution gratings exposed in the two resists. This Chapter also details the chemical structure of SML, as well as the changes occurring in the SML structure after electron beam irradiation, in an attempt to correlate these changes to the lithographic performance of the resist. Fourier transform infrared (FTIR) methods were employed to determine the chemical composition of SML and compared to ZEP and PMMA resists. Since, ZEP and PMMA are widely studied this comparison helps to better understand the lithographic behaviour of the new resist. Hence, this Chapter brings to the forefront the characterisation of SML as a positive tone electron resist and compares its quality to that of ZEP and PMMA resists for nanofabrication.

### 3.1 RESULTS AND DISCUSSION

#### 3.1.1 Contrast Curves

Table 3.1 illustrates the sensitivity and contrast values of the SML resist of three different thicknesses, 50, 100 and 300 nm exposed with 10, 15, 25, 30 and 50 kV voltage beams at room and low temperature (0 °C) (SML 50). The contrast ( $\gamma$ ) values were calculated from the dose values using equation 3.1 below:

$$\gamma = \left[ \log \left( \frac{D_1}{D_0} \right) \right]^{-1} \quad (3.1)$$

where  $D_0$  and  $D_1$  represent the dose values at which the resist thickness is full and zero, respectively (see Chapter 1, Section 1.3.1).<sup>15</sup> The dose values shown in Table 3.1 are equal to the dose at which the irradiated resist completely developed ( $D_1$ ). Considering the sensitivity-contrast values shown in Table 3.1 in ambient

development, it can be interpreted that the contrast values of all of the thicknesses appear in the range of 9-10, regardless of increased voltage or thickness. Nevertheless, it is well established that a rise in the voltage typically results in a reduction in sensitivity, a trend that can be seen in Table 3.1. Generally, with higher voltages up to 100 kV, higher contrast and lower sensitivity can be expected. Surprisingly, the contrast values observed at 50 kV are slightly lower than those at the lower voltages. This could be due to the fact that these exposures were carried out on a JEOL EBL system as well as with a minimum increment of  $5 \mu\text{C}/\text{cm}^2$  in the exposure dose ( $1.75 \mu\text{C}/\text{cm}^2$  for exposures on Raith tool). This might have affected the steepness of the curve giving contrast values slightly different than the trend. Cold development has previously shown resolution enhancement in other positive resists like PMMA and ZEP.<sup>15,16</sup> In order to better understand the influence of cold temperatures on the development of SML resist, contrast curves were generated at voltages of 10, 15, 20 and 25 kV using the SML 50 resist that was developed at  $0^\circ\text{C}$  with the 7:3 IPA:water developer. A comparison between the contrast curves of the SML 50 resist developed at different temperatures can be seen in Figure 3.1(a). The values shown in Table 3.1 suggest a decrease in the sensitivity by 4 times compared to room temperature values and a moderate increase in the contrast (by approximately 1.6 times), due to the use of low temperature developers. Figures 3.1(b) and (c) illustrate the contrast curves for SML 100 and SML 300, respectively; as can be seen the sensitivity decreases with resist thickness. From the contrast figures in Table 3.1, the change in contrast is not immense with respect to the thickness. Next, the contrast curve of SML 300 was compared with those of the standard positive resists ZEP and PMMA, having a similar thickness and exposed at



the same voltage of 10 kV (Figure 3.1(d)). From the values in Table 3.2, the ZEP resist shows the highest sensitivity ( $21 \mu\text{C}/\text{cm}^2$ ) amongst all of the resists. The sensitivity of PMMA ( $79 \mu\text{C}/\text{cm}^2$ ), as expected, lagged behind the ZEP resist by a factor of 3.5, while the sensitivity of SML ( $107 \mu\text{C}/\text{cm}^2$ ) resist developed in 7:3 IPA:water was almost 5 times lower than that of the ZEP resist. The contrast values, on the other hand, showed that the SML contrast was equal to that of PMMA, *i.e.* 12, and was higher than that of ZEP resist (11). From this data it could be established that the SML resist showed poorer sensitivity than the standard PMMA and ZEP resists; the contrast was, however, appreciably high.

**Table 3.1.** Sensitivity and contrast values of three thicknesses of SML developed at room temperature and of SML50 developed at cold temperature <sup>17</sup>

E-beam Voltage (kV)	SML 50		SML 100		SML 300		Cold temperature development	
	<b>D<sub>1</sub></b>	<b>γ</b>	<b>D<sub>1</sub></b>	<b>γ</b>	<b>D<sub>1</sub></b>	<b>γ</b>	<b>D<sub>1</sub></b>	<b>γ</b>
<b>10</b>	63	9.2	72	7.0	102	10.4	280	7.7
<b>15</b>	84	9.0	108	9.0	143	9.8	369	9.2
<b>20</b>	103	9.0	129	10.4	194	8.2	397	11.3

<b>25</b>	111	8.8	156	8.9	218	7.0	563	14.8
<b>50</b>	398	8.6	378	6.7	480	7.9	-	-

**Table 3.2.** Sensitivity and contrast values of SML, PMMA (developed in 7:3 IPA:DI water) and ZEP (developed in ZED N50) resists having 300 nm thickness and exposed with 10 kV electron beam voltage<sup>17</sup>

Resists	Clearance Dose ( $\mu\text{C}/\text{cm}^2$ )	Contrast ( $\gamma$ )
<b>SML</b>	107	12
<b>PMMA</b>	79	12
<b>ZEP</b>	21	11

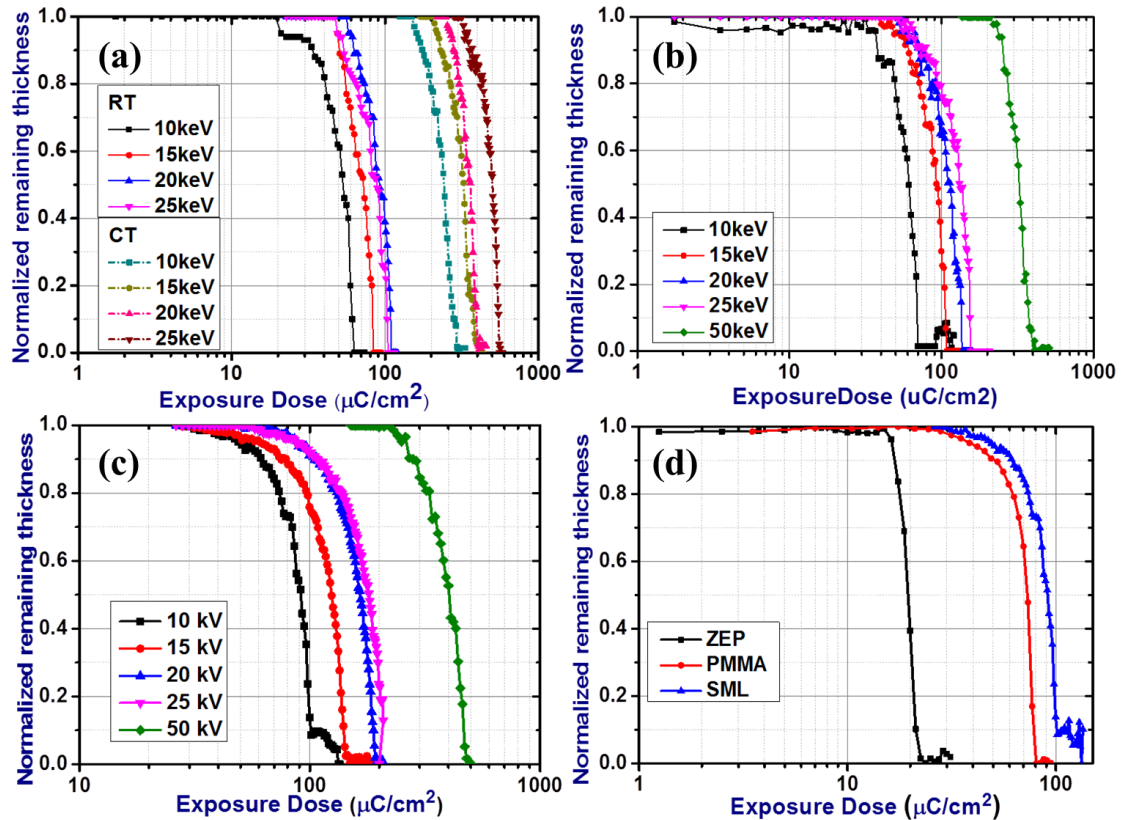


**Figure 3.1.** Contrast curves of (a) SML 50 developed at cold temperature (0 °C) and at room temperature; (b) SML 100, (c) SML 300 and (d) SML 300 compared to ZEP and PMMA resists of similar thickness.<sup>17</sup>

### 3.1.2 Lithographic Quality

In order to investigate the quality of the new resist, high resolution gratings were written on SML and ZEP films, 50 nm thick. The patterned substrates were developed in their respective cold developers. Since, the contrast curves values shown in Table 3.1 suggest a greater contrast at high voltages and cold development, a 30 kV voltage (the maximum voltage offered by the Raith system) was used to expose the high resolution gratings, together with low temperature development.

Figure 3.2 shows SEM images of gratings written as single pixel lines with a 30 nm pitch size in SML (Figure 3.2(a)), ZEP (Figure 3.2(b)) and PMMA (Figure 3.2(c)) resists. Figures 3.2(d) and 3.2(e) illustrate SEM images of ultrahigh resolution structures created by the SML and ZEP resists. As observed in Figure 3.2(a), 14-16 nm wide lines were readily written with a spacing of 15 nm in SML. The arrays of lines were continuous, straight and neat throughout, with very few dwellings where nano-bridging was observed. Moreover, resist clearance from the bottom of the trenches was visibly observed, as shown in Figure 3.2(a). Trivial widening of linewidths from 18 to 20 nm was seen in pitches greater than 30 nm (not shown). However, there was no bridging noticed at larger pitches and the gratings appeared more uniform, sharp, with clean trenches and unceasing lengths than observed in the 30 nm pitch gratings. Furthermore, it was observed that below the

optimum dose the linewidth did not reduce, but the resist residue remained in the trenches (not shown). Identical high resolution gratings exposed on ZEP resist of similar thickness are presented in Figure 3.2(b). The linewidth observed throughout the gratings and in all the pitches was on average 15 nm, without any widening or evidence of nano-bridging observed. Based on Figures 3.2(a) and (b), the quality of the gratings in the two resists were comparable. The line edge roughness, however, appeared faintly higher in the ZEP resist. Thus, it can be established that dense and sub 20 nm lines are easily achievable with the SML resist and the mild 7:3 IPA:water developer. Additionally, the line edge roughness was appreciably lower than in the standard ZEP resist. Figure 3.3(c) shows the same gratings exposed on PMMA with identical working conditions. Poor quality gratings are observed in this image, with high line edge roughness is visible, poor resist clearance from the trenches (poor contrast) and large linewidths from 22 up to 30 nm at higher pitches. The SML resist, thus, exhibited unrivalled gratings in comparison to PMMA. Fig. 3.2(d) shows that 5 nm wide lines were obtained in SML, which are the smallest lines reported to date with this resist. Sub-10 nm lines were also achieved in the ZEP resist as shown in Figure 3.3(e). These data demonstrate that both resists are capable of very high resolution patterning.

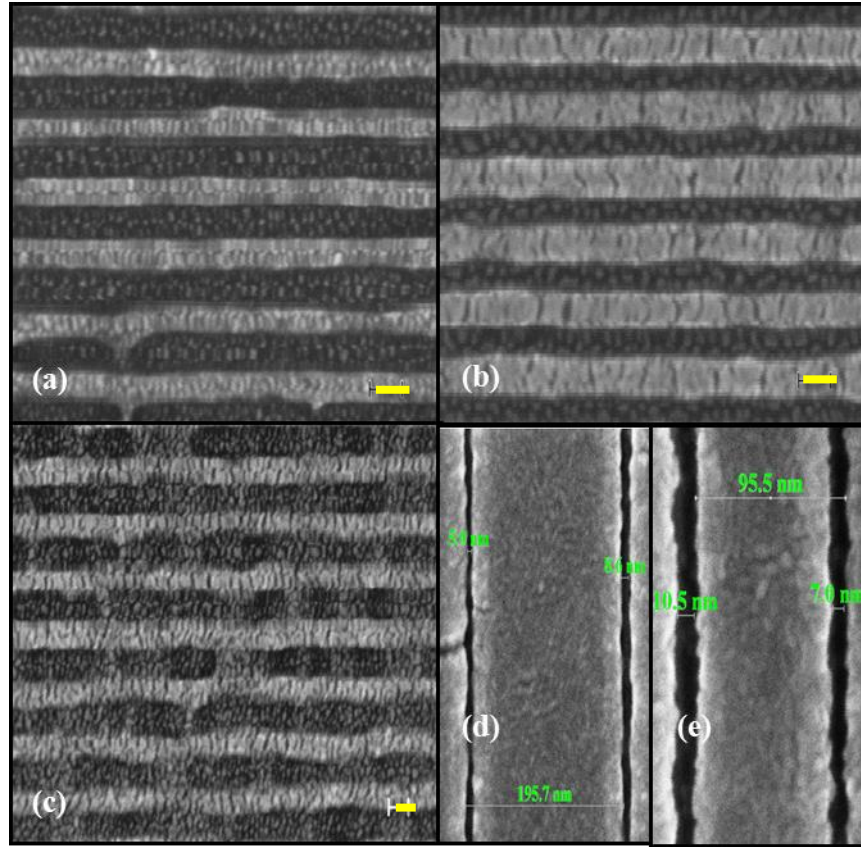


**Figure 3.2.** High resolution gratings with 30 nm pitch size on (a) SML 50, developed in 7:3 IPA:water, (b) ZEP developed in ZED-N50 and (c) PMMA developed in 7:3 IPA:water (20 nm scale bar). Images (d) and (e) show the smallest linewidths achieved in SML 50 and ZEP, respectively (100 nm scale bar).<sup>17</sup>

### 3.1.3 Pattern Transfer Capabilities

In order to inspect the pattern transfer capabilities of the new resist, high resolution gratings on 50 nm thick SML and ZEP resists were subjected to basic etching and metal lift-off techniques. As mentioned in Chapter 2, Section 2.2 of this thesis, Cr metal (5 or 10 nm thick) was evaporated onto patterned Si substrates. During Cr lift-off, it was observed that at a pitch size 80 nm and above, the metal was removed easily within 60 s in acetone at room temperature, whereas for smaller pitch sizes

lift-off was poor even after prolonged immersion in acetone (>8 h) and at an elevated temperature of 60 °C. Therefore, to completely clear the resist from sub-80 nm pitch gratings, the substrates were immersed overnight in Microposit 1165 remover, which is a stronger solvent than acetone. Figures 3.3(a) and (b) show metal lines resolved from a 5 nm thick Cr layer deposited on SML and ZEP resists, respectively. Denser lines (40 nm pitch) with 15 nm linewidths were achieved in SML compared to ZEP.<sup>17</sup> Metal lines as small as 15 nm were obtained in ZEP resist, which was a good achievement from a lithographic point of view. Figures 3.3(c) and (d) show the metal lines resolved by a thicker Cr metal layer of between 10-12 nm. The dimensions of the metal lines with the two resists were similar, *i.e.* ~20 nm, however, the quality differed as ZEP produced coarser metal lines than SML.

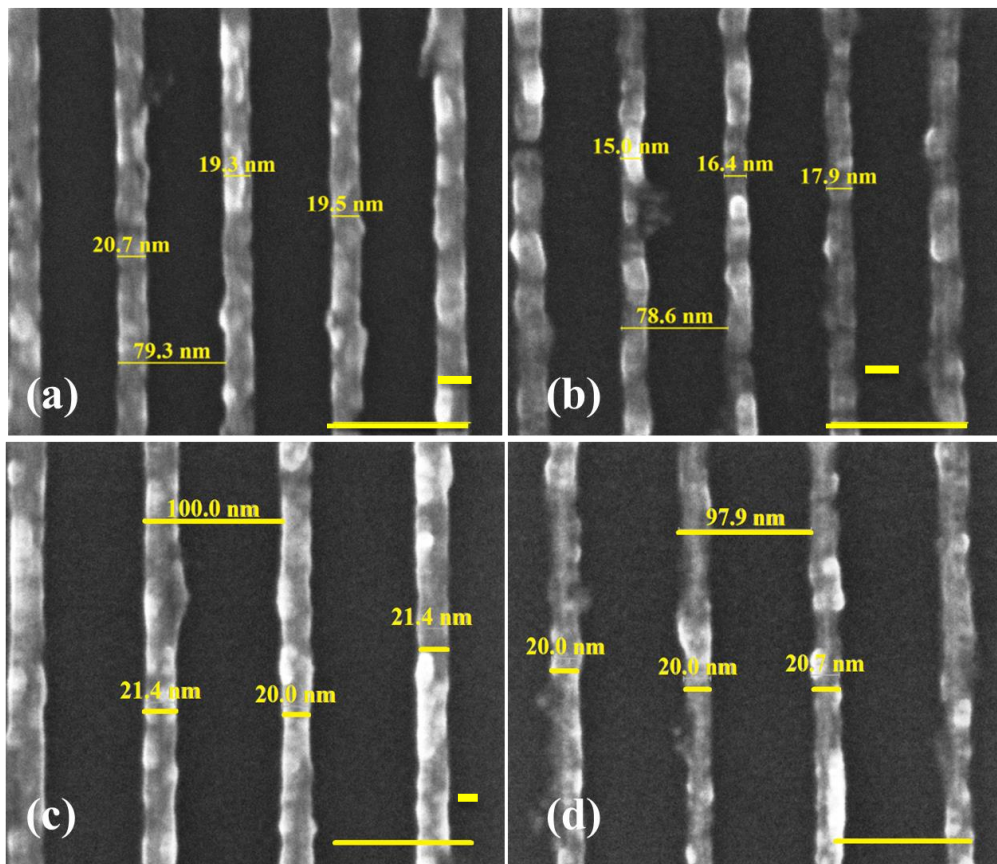




**Figure 3.3.** *Metal lift-off performed using Microposit 1196 remover with 5 nm thick Cr metal by: (a) SML 50 and (b) ZEP and with 10 nm thick Cr metal by: (c) SML and (d) ZEP.*

In the case of etching, the etch rates of the three resists were compared with 300 nm thick layers and are revealed in Figure 3.4. As seen from the plot in Figure 3.4(a), the amount of SML consumed initially is lower than that of ZEP and PMMA. Figures 3.4(a) and (b) confirm that the amount of resist etched in 60 s was 17 nm in the case of SML and ZEP for 27 nm. However, as time progresses SML consumption becomes higher than that of ZEP. As seen from Figures 3.4(a) and (b) that, although the ZEP resist had higher etch resistance than SML after 3 min, the difference between the etch rates was not large. In contrast, the difference in the etch rates at 60 s was quite notable, also suggesting that SML is a more suitable candidate for shallow etching. PMMA on the other hand appeared to have the highest etch rates compared to the other two resists at all intervals, in a good agreement with a number of previous works reporting the poorer etch resistance of PMMA as compared to ZEP.<sup>5</sup> The different etch behaviour of the three resists is obviously determined by their different molecular structure which shall be discussed later in this Chapter.

High resolution gratings were etched for 1 min using the same recipe for both ZEP and SML. Figures 3.4(c) and (d) illustrate gratings having a 60 nm pitch etched into Si using SML and ZEP, respectively. The SEM images in Figure 3.4 show that the quality of grating etched with SML resist are comparable to that of ZEP resist, which

is usually acknowledged for its superior etch performance over other positive tone resists.<sup>5</sup> Whilst etching of dense gratings in Si was possible with both the resists, in the case of ZEP eminent bridging between the trenches was observed throughout the gratings with 40 nm and larger pitches (not shown). This bridging effect was not evident with SML resist. As the pitch size was increased, the quality of the etched lines became enhanced with both resists. However, widening of the Si trenches, up to 20 nm occurred when 15 nm linewidth was achieved by the EBL in ZEP resist. Etched grating with SML showed no obvious widening of linewidth from the EBL achieved linewidths. Bridging at few dwellings even in pitch sizes larger than 60 nm was present in gratings achieved by ZEP resist. This effect was not observed in the case of SML. Therefore, it can be concluded that pattern transfer via etching delivered better results with the SML resist than with ZEP.



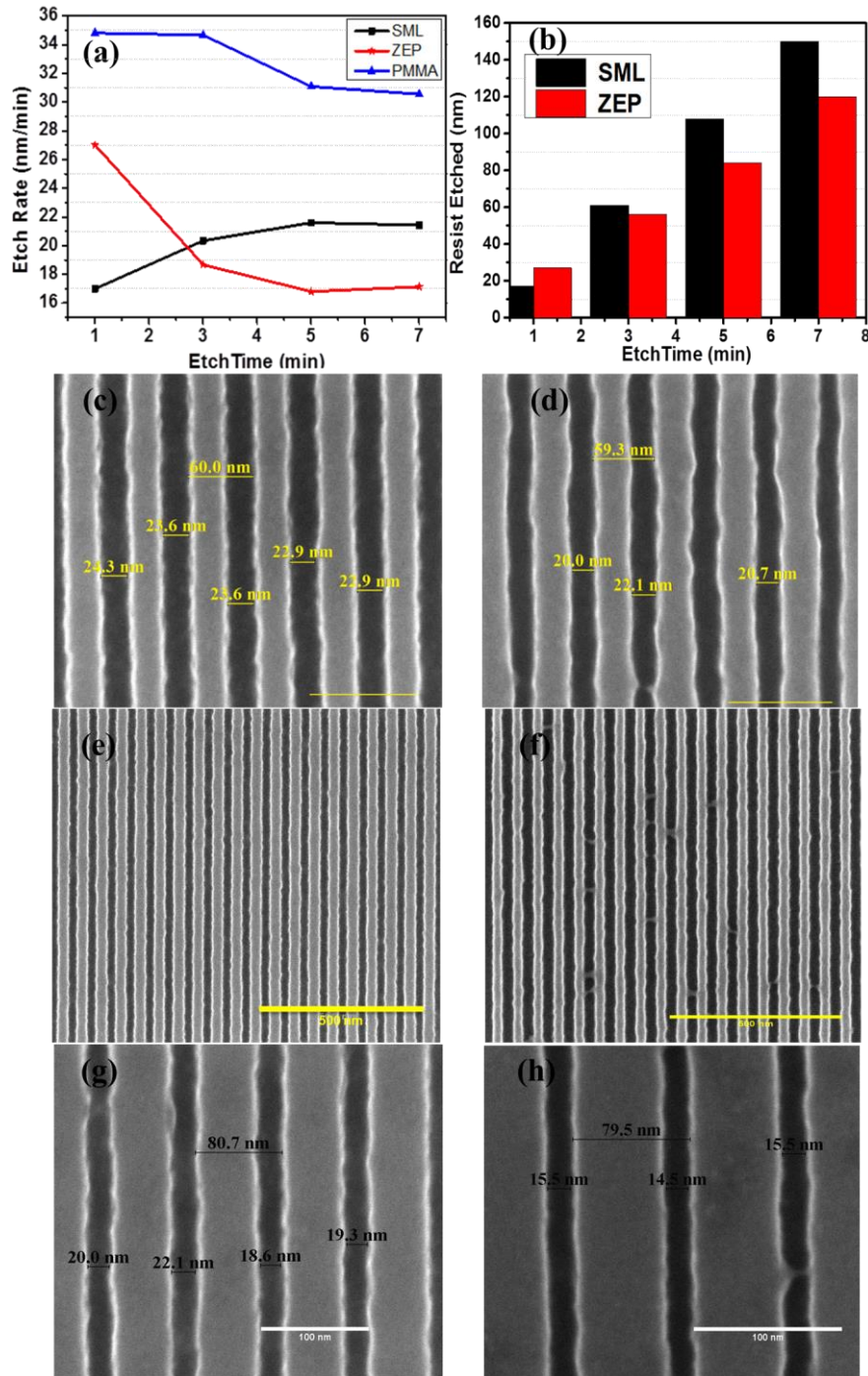


**Figure 3.4.** (a) Etch rates of SML 300 (squares), ZEP (stars) and PMMA (rectangles) at time intervals of 1, 3, 5 and 7 min, via ICP etch ( $\text{SF}_6$  and  $\text{C}_4\text{F}_8$  gas mixture), (b) amount of each resist etched over the same time interval; dense gratings, 60 nm pitch etched into Si with SML 50 (c) and (e) and with ZEP resists (d) and (f) as etch masks (100 nm scale bar); 200 nm pitched gratings etched through

(g) SML 50 and (h) ZEP.<sup>17, 18</sup>

The plot shown in Figure 3.5 illustrates the dose windows for fabricating lines with 60 nm pitch size on Si substrate for SML and ZEP resists developed at 0 °C. Although smaller linewidths were obtained with the ZEP resist in ZED-N50 developer, the process window for SML resists with a 7:3 IPA:water developer were slightly larger, as seen in Figure 3.5. This means that SML offers the broader range exposure doses for obtaining a certain linewidth.

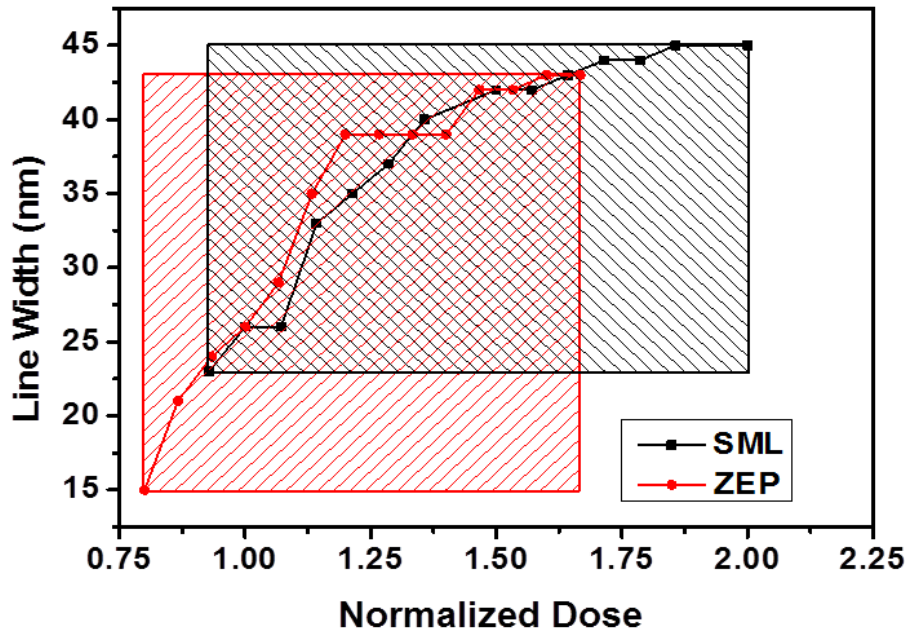


**Figure 3.5.** A comparison of the dose windows for fabricating 60 nm pitch gratings in Si showing the change in linewidth with respect to dose for SML (squares) and ZEP (circles) resists.<sup>17</sup>

### 3.1.4 Roughness Measurements

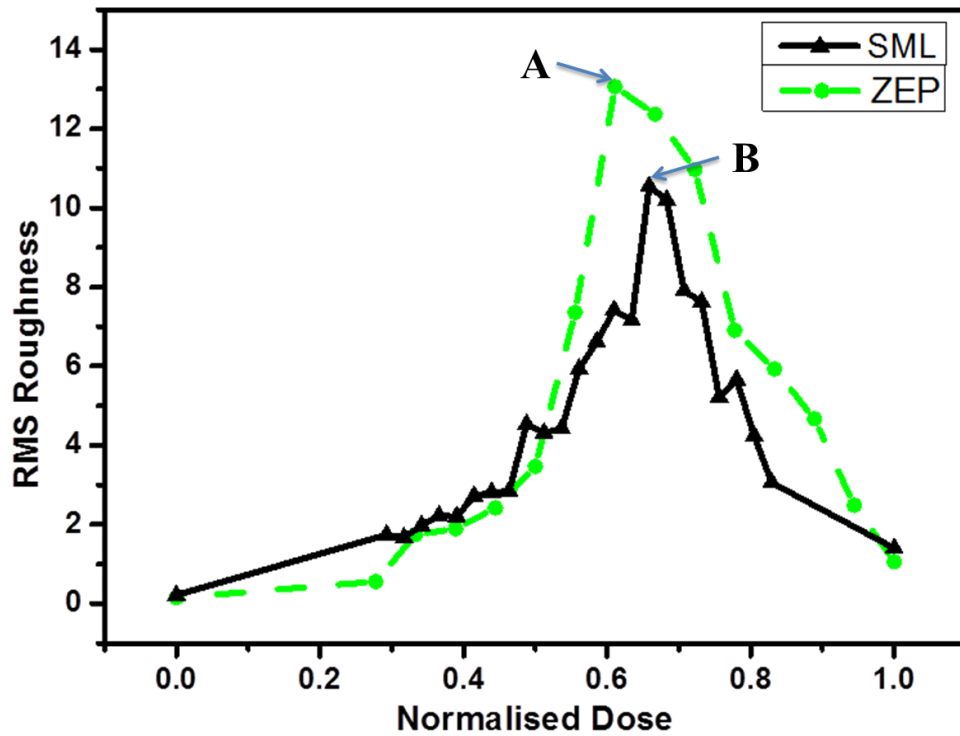


**Figure 3.6.** Root mean square (RMS) surface roughness of SML and ZEP.<sup>18</sup>

The surface roughness of a resist is an important parameter that can influence the lithographic outcome and even the stability of the lithographic structures; the surface roughness of the side walls of exposed structures determines their line edge roughness (LER). The change in surface roughness of SML and ZEP resist lines with respect to increasing electron beam dose was determined by referring to the contrast curves shown in Figure 3.1(d). The root mean square (RMS) values of surface roughness for the two resists at different electron beam doses are presented in Figure 3.6. Surface roughness values were obtained with AFM by scanning on the same boxes on which the contrast curves were acquired. As expected, the roughness of both resists tended to increase with increasing dose and as the electron beam dose was further increased, the roughness reduced equivalent to the initial

value. The roughness versus dose curves of both the resists were very similar to that of PMMA, which is reported S. Yasin *et al.*<sup>19</sup> The roughness of a polymer resist can arise due to various factors, including phase separation, polymer aggregation, the molecular weight of the polymer, developer solvents and development time. In the cited study, PMMA roughness originates during polymer phase separation and during development of the resist after electron beam exposure.<sup>19</sup> The bell-shaped curve of the RMS roughness versus e-beam dose arises due to the different rate of phase separation occurring at various exposure doses.<sup>20</sup> Since SML and ZEP show similar bell shaped curves, it can be suggested that the phase separation processes in both resists taking place during development are similar to that of PMMA, however the mechanism of the main-chain cleaving may differ because of the different developers used.

Although the roughness of both resists (SML and ZEP) commenced with similar values, as the dose increased the roughness intensities tended to differ, as shown in Figure 3.6. On reaching the maximum roughness, ZEP displayed a rougher surface with an RMS value of 13.2 nm, whereas SML had an RMS value 10.5 nm. The lower surface roughness of SML compared to ZEP is beneficial from a lithographic perspective since surface roughness of the side walls of exposed structures eventually determines their LER. This difference in the roughness is due to the dissimilarity in the molecular weights of the two resist polymers. The size of the radius of gyration of a polymer also contributes to the roughness. Thus, the smaller the radius of gyration, the lower surface roughness observed and this is the second possible reasoning for the roughness behaviour of the resists observed in Figure 3.6.<sup>20</sup>

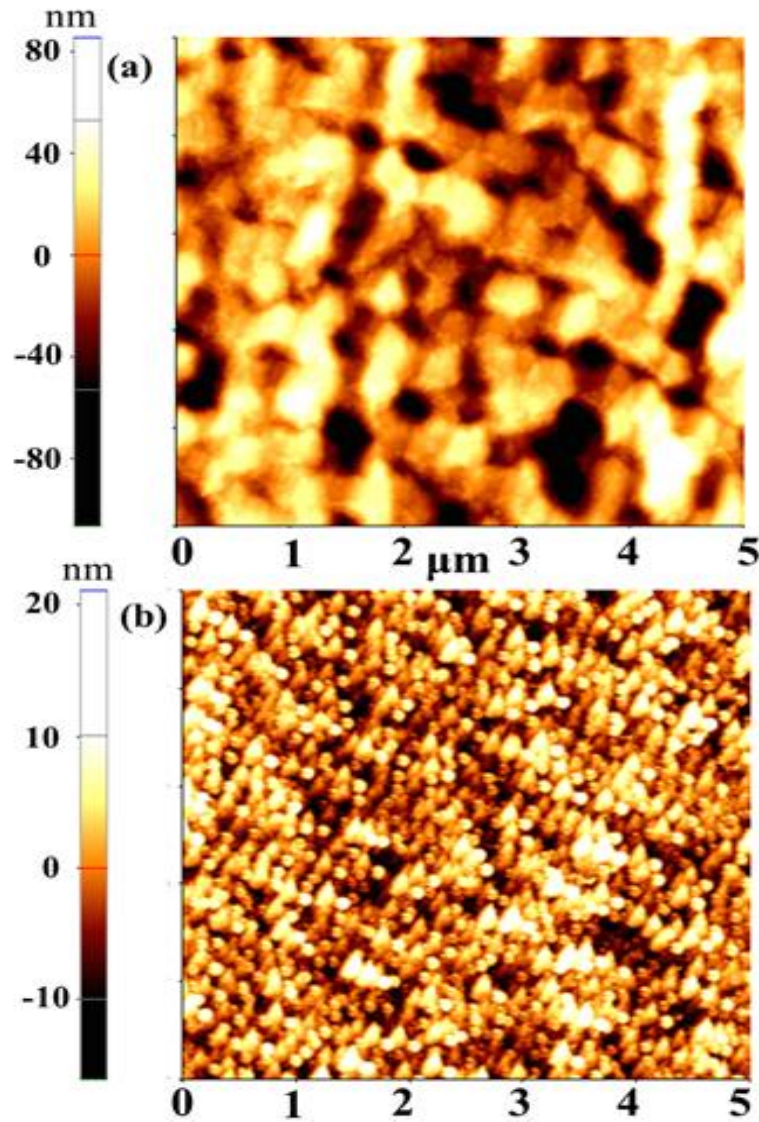


**Figure 3.7.** AFM images of (a) ZEP and (b) SML surfaces at points A and B as shown in Figure 3.6, respectively;  $5\mu\text{m}$  scan size.<sup>18</sup>

To visualise this, two points, A and B, on the roughness versus dose curves shown in Figure 3.6 were chosen for a comparison. The AFM image shown in Figure 3.7(a) illustrates the topography of ZEP resist at point A, whereas Figure 3.7(b) shows the topography of SML resist at point B. Points A and B are the doses at which the maximum surface roughness was observed for the two resists. By comparing both

images, the topography of the ZEP resist was observed to be more uneven and blotchy than that of SML, possibly due to bigger aggregates of ZEP molecules forming on the surface during development. The extent of surface roughness is also determined by the radius of gyration, suggesting that SML has a smaller radius of gyration than ZEP and hence a lower surface roughness.<sup>19</sup>

The surface roughness is manifested in the LER, which is evident in the images shown in Figure 3.8. The sidewall roughness is the surface roughness of the sidewalls of the resist structures that is projected into the LER. Figure 3.8 shows processed SEM images of SML (Figure 3.8(a)) and ZEP (Figure 3.8(b)) to obtain the LER values. The processed images were created by (i) initially converting the SEM data into binary images and subsequently the edges of the lines were extracted, (ii) single lines were then isolated and line graphs were plotted and (iii) the standard deviation ( $\sigma$ ) of the line edge values were obtained.



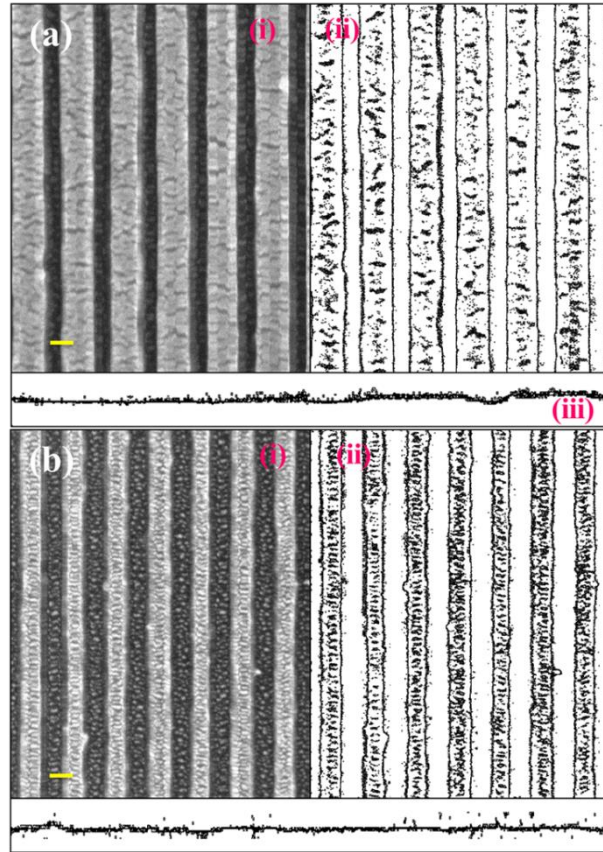


**Figure 3.8.** LHS: Image processing used to obtain LER values from SEM images of (a) ZEP and (b) SML resists. (i) Original SEM images (20 nm scale bar). (ii) SEM data converted to binary images and edges of lines extracted. (iii) Edges of single lines extracted and plotted as a line graph to determine the standard deviation of the line edge values.<sup>18</sup>

The mean  $\sigma$  values for 4 lines were obtained and multiplied by 3 to get the  $3\sigma$  values for both resists, which was 0.227 and 0.354 nm for SML and ZEP respectively. The lower  $3\sigma$  for SML was expected, as the surface roughness of ZEP near the clearance dose was approximately 25 % higher than that for SML. Thus the surface roughness slightly hinders the quality of structures that are obtained from the ZEP resist compared to SML. The pattern transfer images shown in Figures 3.3(a) to (d) also

depict the effect of surface (sidewall) roughness on the Cr metal lines obtained after lift-off and on the trenches etched into Si using both the resists.

Considering the SEM images displayed in Figures 3.3(a) and (b), of the 5 nm thick metal lines resolved by SML and ZEP respectively and Figures 3.4(c) and (d), of the gratings transferred via etching, both pattern transfer processes show that the structures obtained using the ZEP resist are rougher than those obtained from SML. Although metal lines as narrow as 15 nm were achievable with the ZEP resist (Figure 3.3(b)), they were coarse and appeared lumpy in places; this effect did not decrease with increasing pitch size or by increasing the metal thickness to 10 nm (Figure 3.3(d)). The gratings etched into the Si substrates also showed similar results. Even though relatively smooth lines were obtained after EBL exposure with ZEP (Figure 3.4(f)), the LER of the gratings seemed to degenerate after etching, possibly due to the higher surface roughness of ZEP as compared to SML. Thus, a higher LER was observed in patterns transferred using ZEP resist in comparison to SML.



### 3.1.5 FTIR Measurements

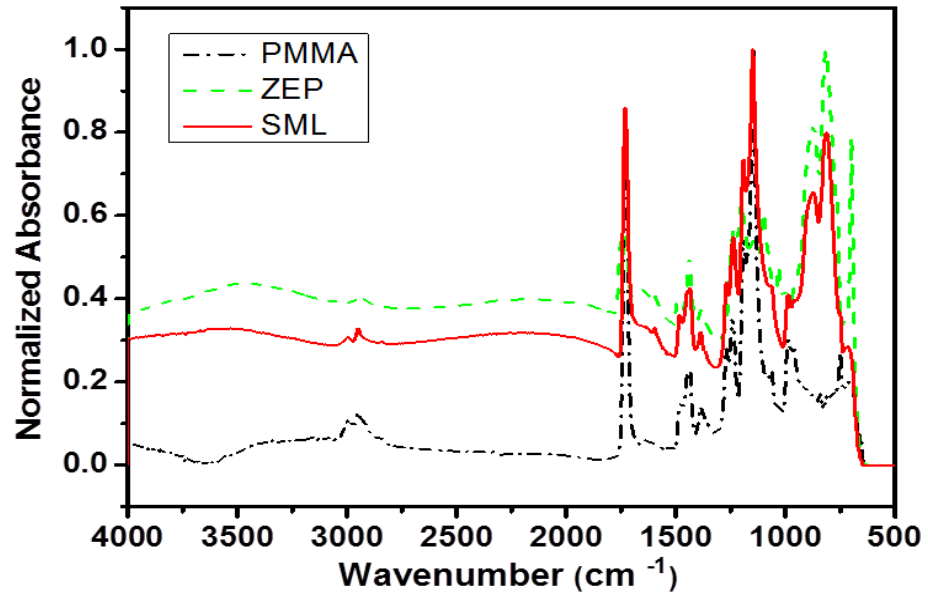


**Figure 3.9.** FTIR spectra of 50-60 nm thick films of SML (red), ZEP (green) and PMMA (black) resists coated on Si substrates.<sup>18</sup>

Details about the composition of a certain substance can be extracted from its infrared spectra. In the case of resists, the functional groups, backbone chains and bonding within the polymer can be determined. Figure 3.9 illustrates FTIR measurements taken of 50-60 nm thick films of SML, ZEP and PMMA coated on Si substrates. Measurements were carried out on  $1\text{ cm} \times 1\text{ cm}$  Si chips. ZEP is a modification of the PMMA polymer,<sup>5</sup> hence to understand the similarities of the new resists to ZEP, PMMA was also included in the FTIR study. As seen from three spectra shown in Figure 3.9, the resists have similar chemical structures.

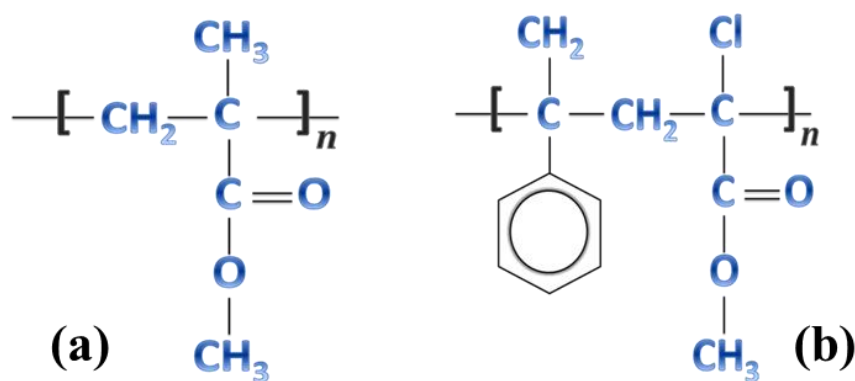


**Figure 3.10.** Chemical structure of (a) PMMA and (b) ZEP resist polymers.<sup>18</sup>

Figure 3.10 shows the chemical structures of PMMA and ZEP resists. The methacrylate group is common in both the structures, with ZEP having two additional groups, *i.e.* the Cl-group and the phenyl group ( $\alpha$ -methyl styrene). Figure 3.11(a) illustrates the IR spectra of the fingerprint regions of SML and PMMA, whereas Figure 3.11(b) shows IR data of SML and ZEP resists for comparison. The peaks observed at 870 and 699 cm<sup>-1</sup> in Figure 3.11(b) are due to the phenyl rings and the Cl groups of ZEP, respectively. These peaks are missing in the PMMA spectrum shown in Figure 3.11(a). The doublet peaks at 1725 and 1750 cm<sup>-1</sup> in the ZEP spectrum represent the C–O bond in the ester group. A shift of the C–O peak to a higher wavenumber is seen when the Cl atom is closer to the carbonyl group.<sup>21</sup>

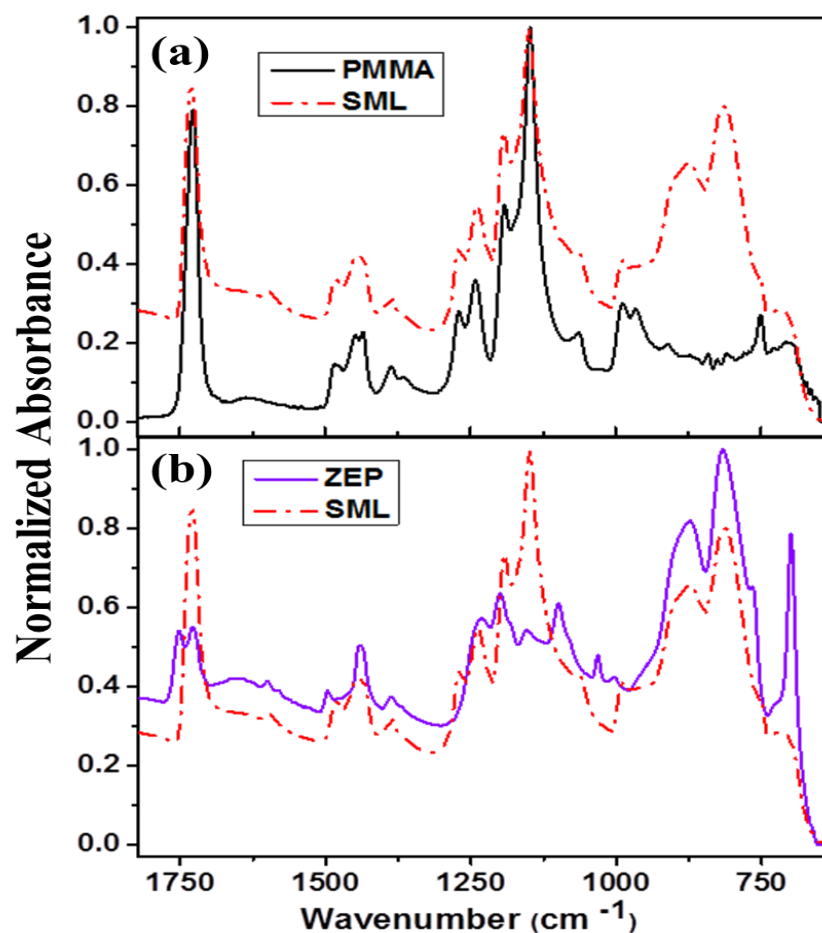


**Figure 3.11.** Comparison of the FTIR finger-print regions of SML (red dashed plots) with (a) PMMA (black solid) and (b) ZEP resists (violet solid).<sup>18</sup>

When SML was compared with both resists it was found to be more analogous to PMMA, except for the two intense peaks at 813 and 873  $\text{cm}^{-1}$ , which corresponds to the aromatic rings. Nevertheless, a peak for the Cl-groups was absent in SML, unlike ZEP. Moreover, in the SML spectrum, peaks observed at 1149  $\text{cm}^{-1}$  suggest the presence of a C–O–C stretch from an ester group, alike in the other two resists. The peak at 1732  $\text{cm}^{-1}$ , a characteristic peak of the PMMA resist,<sup>22</sup> was also seen in SML, representing the C=O stretch of the acrylate group. Peaks at 1388 and 750  $\text{cm}^{-1}$

<sup>1</sup> in the PMMA spectrum can be attributed to the  $\alpha$ -methyl vibrational groups which are present in SML as well. Thus, it could be established from the three spectra that the SML resist has a backbone of methyl acrylate like the other two resists. However, SML does differ from PMMA with respect to the occurrence of an aromatic peak and from ZEP due to the absence of a Cl group.

The very high sensitivity of the ZEP resist has been associated with the presence of the Cl group in its polymer chain.<sup>5</sup> The electron beam sensitivity of poly methylstyrene is low and it is understood that chlorine induces additional scattering events, which results in a scission in the main backbone of ZEP. Thus, due to the lack of such a scission-initiation group, SML demonstrates reduced sensitivity. On the other hand, on comparing with PMMA, the FTIR spectra suggest that SML has an additional methylstyrene group in its main polymer chain. Hence, the electron dose required to break the extra molecules in the SML polymer chain is higher than that for PMMA. These reasons could account for the reduced sensitivity of SML compared to ZEP and PMMA. Moreover, when ZEP and PMMA were compared, the higher etch resistance of ZEP observed was attributed to the  $\alpha$ -methylstyrene moiety.<sup>23</sup> As reported in Chapter 3, Section 3.2.3 of this thesis, the etch durability of SML is very similar to that of the ZEP resist and can be attributed to the presence of the  $\alpha$ -methylstyrene group, as revealed by the FTIR analysis of SML, and its effect on the lithographic performance.<sup>17</sup>

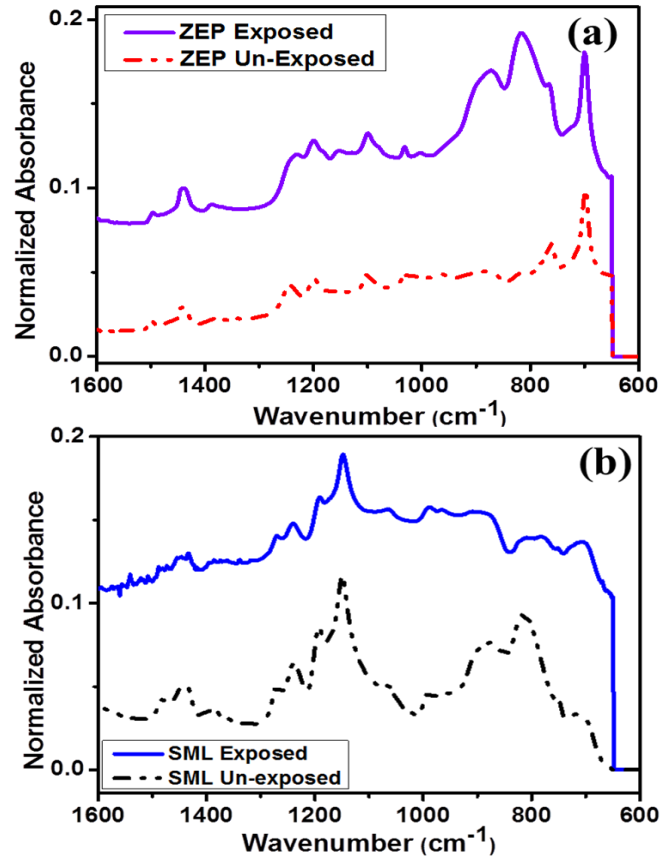


**Figure 3.12.** Comparison of the FTIR spectra of exposed (solid plots) and unexposed (dotted plots) (of ) SML and (b) ZEP resists.<sup>18</sup>

Figures 3.12(a) and (b) show the FTIR spectra of exposed and unexposed ZEP and SML, respectively. In Figure 3.13(a) the most obvious difference noticed was the peak at  $817\text{ cm}^{-1}$ , which increased significantly after irradiation of the ZEP resist by the electron beam. The IR peak in this region can be accredited to a  $>\text{C}=\text{C}<$  stretch. The increase in the peak at  $817\text{ cm}^{-1}$  suggests that there is an increase in unsaturation ( $\text{C}=\text{C}$ ) within the polymer chain upon exposure. The major known chemical change that occurs after irradiation of any polymer is main chain-scission, the formation of new bonds ( $\text{C}=\text{C}$ ) and the evolution of gases such as  $\text{CO}_2$ . Another peak shown in Figure 3.11(a) at  $1230\text{ cm}^{-1}$  reduced after electron beam exposure; this peak can be

attributed to a C–O–C asymmetric stretch. The reduction in this peak suggests the breaking of C–O bonds in the acrylate group of ZEP. In the case of SML, similar results were observed. The most obvious peak enlargement shown in Figure 3.12(b) was around  $700\text{--}800\text{ cm}^{-1}$  which also suggests an increase in unsaturation, *i.e.* the formation of  $>\text{C}=\text{C}<$  groups by breaking of the main polymer chain. A reduction in the peak at  $1192\text{ cm}^{-1}$  for exposed SML was also observed. This peak can be attributed to an ester C–O stretch that is reduced after radiation, indicating the dissociation of the acrylate group in the SML polymer chain. In a recent FTIR study of PMMA, to understand the reaction mechanism after electron beam irradiation, it was found that an increase in the C=C bonds along with the increase in the e-beam dose led to the main chain scission of the PMMA polymer chains.<sup>24</sup> Breaking of the carbonyl group in the polymer was also reported after electron beam radiation. Since the spectra in Figure 3.9 suggest that all three resists have similar structures, they may also undergo similar scission in the main chain during exposure. Moreover, an increase in unsaturation was also observed in SML and ZEP resists, along with the indications of a reduction of the carbonyl peak after irradiation. The course of the reaction for ZEP resist after irradiation is, however, reported to be different due to the presence of the Cl and phenyl groups.<sup>5</sup> Similarly, SML may not have the same course of main-chain scission as PMMA since a phenyl group is present in SML's structure as well. Additionally, the SML polymer molecule may be larger (due to the additional groups present) than that of PMMA, which would take a greater electron dose to cleave the chain and hence the sensitivity observed is lower for SML.

### 3.2 CONCLUSION

To conclude, this Chapter described for the first time the characterisation of the new resist, SML entirely from a lithographic perspective. A comparison of SML to PMMA and ZEP resists aided to determine its proficiency as an EBL resist for semiconductor nanofabrication. The contrast curves revealed that although the sensitivity of SML was lower than that of ZEP and PMMA, its contrast value was similar or even higher than the other two resist, which is desirable for fabrication by the EBL. Lithographic resolution of SML was also found to be commendable in comparison to that of ZEP and PMMA. An assessment of SML's etching and metal lift-off ability showed that SML was a good candidate for both processes. Data showed that etching was more uniform with SML since no feature widening and bridging was observed in contrast to ZEP. Using SML, dense (40 nm pitch) metal lines of ~15 nm linewidth were readily achievable with a basic lift-off technique. The larger process window and low LER values confirmed that SML was more commendable for EBL patterning than ZEP and PMMA resists.

A link between the chemical properties of SML and ZEP resists and their lithographic rendition was also demonstrated. The roughness of SML and ZEP resists, along with incrementing e-beam doses, showed the effect of surface irregularity on the lithographic performance of the two resists. SML exhibited a lower surface roughness as a function of exposure dose when compared to ZEP, which was also reflected in the LER of the EBL patterned structures. Thus, the effect of the surface roughness of a resist eventually determines the quality of the patterned lithographic structures.

Lastly, the strong resemblance of the three FTIR spectra of SML, ZEP and PMMA,

confirmed the analogous chemical composition of the three polymers. The lower sensitivity of SML compared to ZEP can be attributed to the absence of a Cl group in the SML polymer, while the lower SML sensitivity in regard to PMMA is due to the presence of additional methylstyrene groups in SML. The good etch durability of SML can also be determined from the structural data acquired from the spectra and is due to the same  $\alpha$ -methylstyrene moiety, which is also present in ZEP, but is absent in PMMA. A substantial amount of data could not be extracted from the FTIR spectra of the irradiated resists, however major changes such as an increase in unsaturation and alteration in acrylate groups in SML and ZEP were revealed.

### 3.3 BIBLIOGRAPHY

1. E. Reichmanis, F.M. Houlihan, O. Nalamasu, T.X. Neenan. *Chem. Mater.* 1991, **3**, 394.
2. S. Ma, C. Con, M. Yavuz, B. Cui. *Nanoscale Res. Lett.* 2011, **6**, 446.
3. D. Küpper, D. Küpper, T. Wahlbrink, J. Bolten, M.C. Lemme, Y.M. Georgiev H. Kurz. *J. Vac. Sci. Technol. B.* 2006, **24**, 1827.
4. S. Yasin, D.G. Hasko, H. Ahmed. *Appl. Phys. Lett.* 2001, **78**, 2760.
5. K. Koshelev, M.A. Mohammad, T. Fito, K.L. Westra, S.K. Dew, M. Stepanova. *J. Vac. Sci. Technol. B.* 2011, **29**, 306.
6. D. Küpper, D. Küpper, T. Wahlbrink, W. Henschel, J. Bolten, M.C. Lemme, Y.M. Georgiev H. Kurz. *J. Vac. Sci. Technol. B.* 2006, **24**, 570.
7. Y.M. Georgiev, W. Henschel, A. Fuchs, H. Kurz. *Vacuum.* 2005, **77**, 117.
8. W. Chen and H. Ahmed. *Appl. Phys. Lett.* 1993, **62**, 1499.
9. K. Kanzaki, T. Yamaguchi, M. Nagase, K. Yamazaki, H. Namatsu. *Jpn. J.*



- Appl. Phys.* 2002, **41**, L1342.
10. H. Namatsu, M. Nagase, T. Yamaguchi, K. Yamazaki, K. Kurihara. *J. Vac. Sci. Technol. B.* 1998, **16**, 3315.
11. D. Küpper, D. Küpper, Y.M. Georgiev, T. Wahlbrink, W. Henschel, G. Bell, H. Kurz. *Appl. Phys. Lett.* 2004, **85**, 5055.
12. S. Yasin, D.G. Hasko, H. Ahmed. *Microelectron. Eng.* 2002, **745**, 61.
13. S. Lewis, D. Jeanmaire, L. Piccirillo. *High Acceleration Voltage Characterization of SML Electron Beam Resist for Ultra High Aspect Ratio Nano-Lithographic Applications*. Proceedings of EIPBN, Las Vegas, 2011.
14. M.A. Mohammad, S.K. Dew, M. Stepanova. *Res. Lett.* 2013, **8**, 139.
15. M.A. Mohammad, K. Koshelev, T. Fito, D.A. Zhi Zheng, M. Stepanova, S. Dew. *Jpn. J. Appl. Phys.* 2012, **51**, 06FC05-1.
16. B. Cord, J. Lukenhaus, K.K. Berggren. *J. Vac. Sci. Technol. B.* 2007, **25**, 2013.
17. A. Gangnaik, Y.M. Georgiev, B. McCarthy, N. Petkov, V. Djara, J.D. Holmes. *Microelectron. Eng.* 2014, **123**, 126.
18. A. Gangnaik, Y.M. Georgiev, J.D. Holmes. *J. Vac. Sci. Technol. B.* 2015, **33**, 041601.
19. S. Yasin, M.N. Khalid, D.G. Hasko, H. Ahmed. *Microelectron. Eng.* 2004, **259**, 73.
20. S. Yasin, D.G. Hasko, M.N. Khalid, D.J. Weaver, H. Ahmed. *J. Vac. Sci. Technol. B.* 2004, **22**, 574.
21. R.M. Silverstein, G.C. Bassler. *J. Chem. Educ.* 1962, **39**, 546.
22. L.S. Acosta-Torres, L.M. López-Marín, R.E. Núñez-Anita, G. Hernández-Padrón, V.M. Castaño. *J. Nanomater.* 2011, Article ID 941561.

23. T. Nishida, M. Notomi, R. Iga, T. Tamamura. *Jpn. J. Appl. Phys.* 1992, **31**, 4508.
24. P. Tiwari, A.K. Srivastava, B.Q. Khattak, S. Verma, A. Upadhyay, A.K. Sinha, T. Ganguli, G.S. Lodha, S.K. Deb. *Measurement*. 2014, **51**, 1.

## CHAPTER 4

---

# **PATTERNING OF GERMANIUM SURFACE WITH HSQ RESIST**

#### 4. PATTERNING OF GERMANIUM SURFACE WITH HSQ RESIST

Continual scaling down of semiconductor devices has led to an upsurge of sophisticated nanofabrication tools. Amongst the few extensively used techniques, electron beam lithography (EBL) is certainly the preferred tool for high-resolution patterning in research and development (R&D) and small volume production. EBL is a direct-write method that requires a resist and is capable of nanopatterning even below 10 nm. The EBL radiation brings about structural changes of the resist material, such as cross-linking or chain-scission; in most cases a combination of both with one of the processes significantly prevailing over the other. To achieve a successful fabrication process, parameters like exposure voltage and dose, resist and substrate materials, developer solution, development time and temperature have to be taken into account. These parameters are interdependent and work together to give the best possible results. Hydrogen silsesquioxane (HSQ) is an inorganic high resolution, negative tone EBL resist<sup>1</sup>, which offers critical dimensions below 10 nm with ease. Due to physical and chemical similarity of HSQ to SiO<sub>2</sub>, it is highly compatible with microelectronic processing.<sup>2</sup> HSQ is commonly used to pattern Si surfaces, however its application on other materials is fairly limited.<sup>3,4</sup>

Currently, most semiconductor processes involve the use of Si platforms and only a fraction employ Ge. However, Ge is becoming a highly desirable material due to various superior qualities over Si. Ge is a carbon group (Group IV) semiconductor with a lower effective charge carrier mass than Si<sup>5</sup>, resulting in a higher electron and hole mobility (effective mass of Si = 1.06 and Ge = 0.55).<sup>6</sup> Therefore, Ge-based

nanoelectronic devices could offer improved performance at reduced power consumption compared to the Si electronics. However, handling Ge is more complicated than well-established Si processing. Ge surfaces are always covered by native Ge oxides consisting of GeO and GeO<sub>2</sub>, which form in ambient atmosphere. The latter oxide is readily soluble in water and aqueous based solvents.<sup>7</sup> Development of exposed HSQ resist in tetramethylammonium hydroxide (TMAH) or aqueous NaOH solvents can dissolve the Ge native oxides. Thus, if a Ge oxide is present between a Ge substrate and EBL exposed HSQ, the mask will rinse off during development and so will the desired high-resolution pattern. Removal of native oxides on Ge prior to EBL exposure, or the use of non-aqueous based solvents during development, is obligatory. However, after removing the oxides new GeO<sub>x</sub> layers have been reported to form on the surface of Ge substrates within 2 min.<sup>8</sup> Moreover, non-aqueous developers of HSQ do not have the potential to yield extremely high-resolution structures and alcohols promote gelation of HSQ.<sup>9</sup>

To date very few successful methods of patterning Ge with HSQ have been reported.<sup>10,11</sup> One procedure involves treating the Ge surface with halogen acids (Cl typically) which is reported to eliminate the interfacial oxides and terminate the surface with the corresponding halogen.<sup>12</sup> In the study, Ge substrates are first immersed in de-ionised water (DI) followed by 4.5 M HNO<sub>3</sub>, to ensure removal of water soluble and uneven layers of Ge oxides. Subsequently, HNO<sub>3</sub> leads to the reforming of an even layer of the oxides. The substrates were then immersed in 10 wt% HCl solution for 10 min to certify the elimination of oxides and the termination of the Ge surface with Cl group. After this process, HSQ was spun onto the substrates and exposed by EBL. This technique yielded high resolution

structures that were well adhered to the substrate after developing with aqueous solvent. However, the process described involves several steps and is therefore, time consuming. Another reported procedure is based on the deposition of a buffer layer, such as  $\text{SiO}_2$ ,  $\text{Al}_2\text{O}_3$ , or  $\text{Si}_3\text{N}_4$ , between the oxidised Ge surface and the HSQ resist. The buffer layer prevents lifting off of the high resolution HSQ pattern during development and can be used as a hard mask during the subsequent pattern transfer.<sup>11,13</sup> In one of these studies, a 20 nm  $\text{Si}_3\text{N}_4$  layer was deposited onto the surface of a Ge substrate by plasma-enhanced chemical vapour deposition (PECVD).<sup>13</sup> Next, the HSQ film was spun on the buffer layer, exposed by the EBL and developed. Subsequently, the hard mask (the  $\text{Si}_3\text{N}_4$  layer) was first etched, followed by Ge etching to transfer the pattern into the Ge substrate. Again, although high-resolution structures were produced, this approach involves additional processing steps and overcomplicating the patterning of Ge.

This Chapter details a novel, simple, cheap and safe method to pattern Ge with HSQ resist. The method developed has a single step, short uptime and involves using simple “household” acids, such as citric and acetic acid. The acids not only create oxide-free Ge surfaces but also help in the adhesion of HSQ resist on Ge substrates for EBL exposure. The process is reliable and reproducible on Ge and germanium-on-insulator (GeOI) substrates. Unlike some other acids, citric and acetic acid did not etch away the Ge substrate surface. Moreover, these acids are environment friendly, non-hazardous to humans and cheaper than acids such as hydrogen fluoride (HF). The effects of immersion time and acid concentration on Ge surfaces are described in this Chapter, with the aim of highlighting the best exposure conditions for HSQ patterning.

## 4.1 RESULTS AND DISCUSSION

### 4.1.1 Germanium Patterning With Acid Treatment

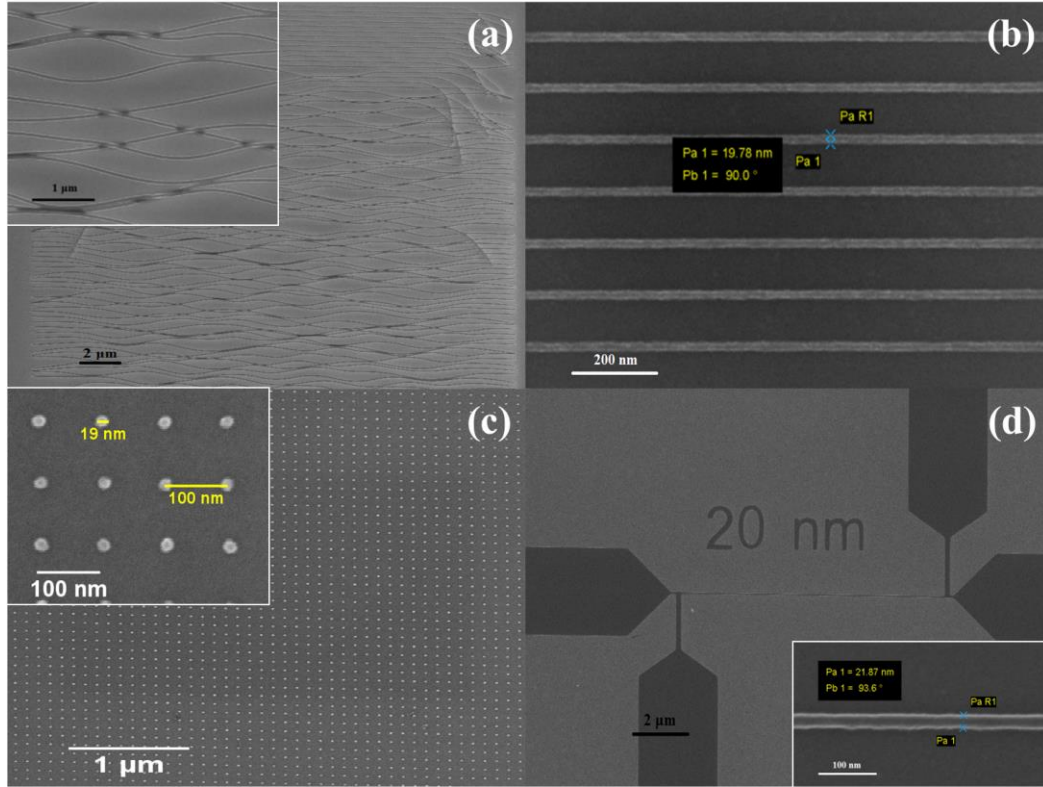


**Figure 4. 1.** SEM micrographs of (a) HSQ gratings on a Ge substrate with no prior surface treatment, (b) 20 nm wide HSQ gratings with 120 nm pitch on a Ge chip pre-treated with citric acid, (c) an array of 20 nm dots etched into acetic acid-treated GeOI through the HSQ mask and (d) four probe resistance measurement test structure with a 20 nm nanowire patterned on GeOI with HSQ resist. All insets are higher magnification images.

Figure 4.1(a) shows an SEM image of an untreated Ge substrate after HSQ deposition and subsequent EBL exposure. Although the HSQ lines were resolved with the desired linewidth of 50 nm (inset), the adhesion of the HSQ to the Ge substrate was immensely poor. This Ge substrate was not treated with any acids and

was only degreased with acetone and IPA and rinsed with DI water prior to HSQ resist deposition. The native oxides on the Ge surface were therefore not removed and hence during the development with the aqueous solvents they were washed away, resulting in the lifting of the overlaying HSQ lines. Figure 4.1(b) displays the SEM image of HSQ gratings on Ge substrate treated with citric acid. The Ge chip was immersed in 1.73 M citric acid in DI water for approximately 5 min, rinsed with DI water for 2-3 min and then blown dried thoroughly before spin-coating the HSQ resist. Figure 4.1(b) shows that HSQ lines as narrow as 20 nm adhered very well to the Ge surface. The quality of the structure was not compromised even though the EBL exposure dose was kept the same as that for the untreated Ge surface. Moreover, the size of the pitch (the distance between the edges of two lines) did not affect the adhesion to the Ge surface. This observation shows that citric acid efficaciously removed the Ge native oxides prior to the HSQ resist deposition. Hence, a strong aqueous base, such as NaOH, could also be used for the development of high-resolution HSQ structures. Figure 4.1(c) shows an array of nanodots patterned on a GeOI substrate treated with 2.35 M concentration acetic acid. The inset in Figure 4.1(c) shows the critical dimension of the nanodots, which are as small as 20 nm that are spaced ~80 nm apart (100 nm pitch). Additionally, the image contrast observed for the substrate was higher than that for untreated GeOI surfaces, which could be due to the acids passivating the substrate with functional groups that will be discussed later in this Chapter. Similar results of good adherence of HSQ structures to Ge surfaces were observed with diluted solutions of both citric and acetic acids, i.e. 0.43 for citric acid and 1.38 for acetic acid. Figure 4.1(d) illustrates a Ge nanowire with a width of 20 nm and a length of 10  $\mu\text{m}$  length



between two Ge contacts. The inset of Figure 4.1(d) shows the critical dimension of the nanowire which is 21 nm. Nanowires ranging from 1000 to 20 nm were fabricated using 1.7 M citric acid on GeOI substrates and subsequently etched into the top Ge layer by reactive ion etch (RIE). All images shown in Figure 4.1 prove that the novel acid treatment of Ge surface is capable of competently producing high-resolution HSQ structures.

#### 4.1.2 XPS Analysis

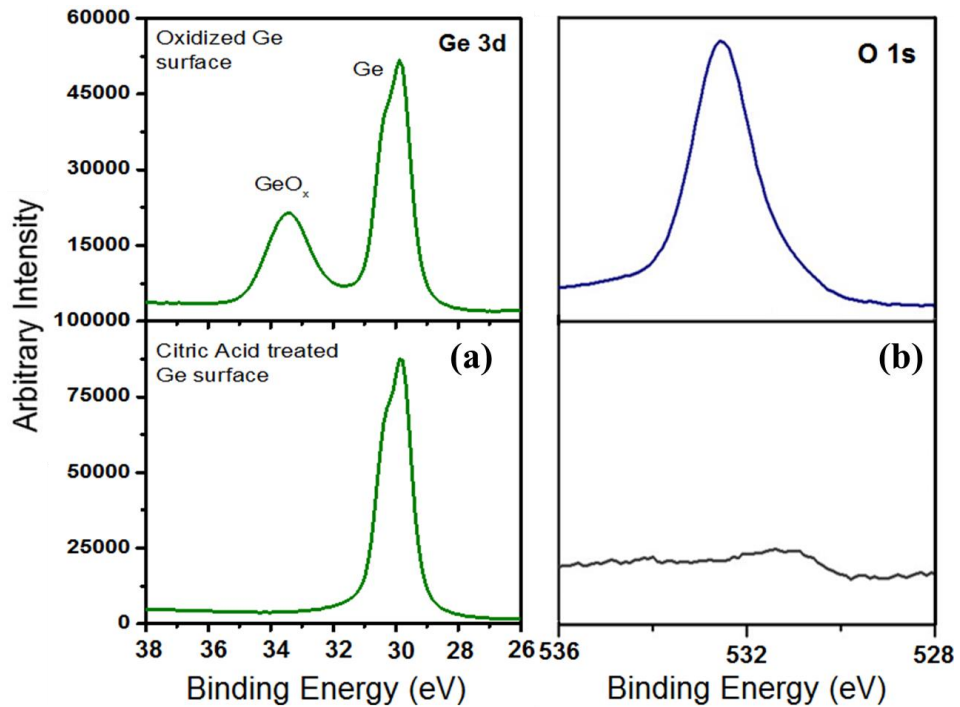


**Figure 4. 2.** XPS spectra of (a) Ge 3d core-level and (b) O 1s of a Ge surface before (upper spectra) and after (lower spectra) treated with 0.74 M citric acid for 60 s. The GeO, GeO<sub>2</sub> and O 1s peaks are eliminated after citric acid treatment.

Figure 4.2 illustrates the X-ray photoelectron spectroscopy (XPS) spectra from a Ge surface before and after treatment with citric acid for 60 s. The upper plots in

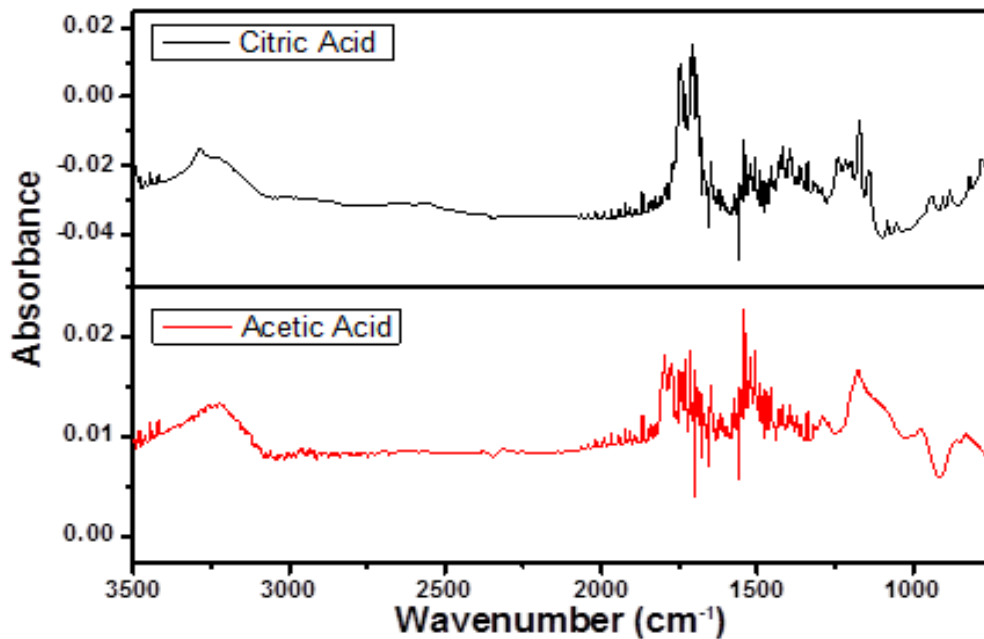
Figure 4.2 highlight the Ge surface before any treatment, whereas the lower plots are representative of the surface after treating the Ge surface with 0.74 M citric acid for 60 s. Figure 4.2(a) shows the Ge 3d core-level and Figure 4.2(b) shows the O 1s spectra under both conditions. The obvious observation from Figure 4.2(a) is the elimination of peaks denoting the presence of oxides. In Figure 4.2(a), prior to the citric acid treatment, wide peaks are observed at 33.75 and at 33 eV due to contributions from GeO and GeO<sub>2</sub>, respectively. These two peaks were completely absent on the XPS spectra after treatment with citric acid for 60 s. Similarly, in the O 1s spectrum of an untreated sample (Figure 4.2(b)), a clear peak is observed at 532 eV, which was completely eradicated post citric acid treatment. Thus, the given data supports the fact that native oxides on the Ge surface are successfully removed after acid treatment. Due to the exclusion of the interfacial oxides between Ge and HSQ, it was possible to fabricate high-resolution structures on Ge with the HSQ resist after acid treatment, as shown in Figure 4.1.

### 4.1.3 FTIR Analysis

Fourier transform infra-red (FTIR) spectroscopy was employed to detect changes on surface of Ge substrates after treating with citric and acetic acid. Due to the nature of the attenuated total reflectance (ATR) crystal (a pure Ge crystal globe), it was not feasible to obtain any measurements from the Ge chips. Therefore, the flat arc of the ATR crystal in the FTIR instrument, itself, was passivated with the acids to obtain IR data. A drop of the required acid was placed on the ATR crystal for approximately 60 s. Excess acid was absorbed onto a blotting paper until the crystal was almost dry before being left at air for another 3 to 5 min for the remaining moisture to completely dry out. The crystal was then carefully placed in the FTIR

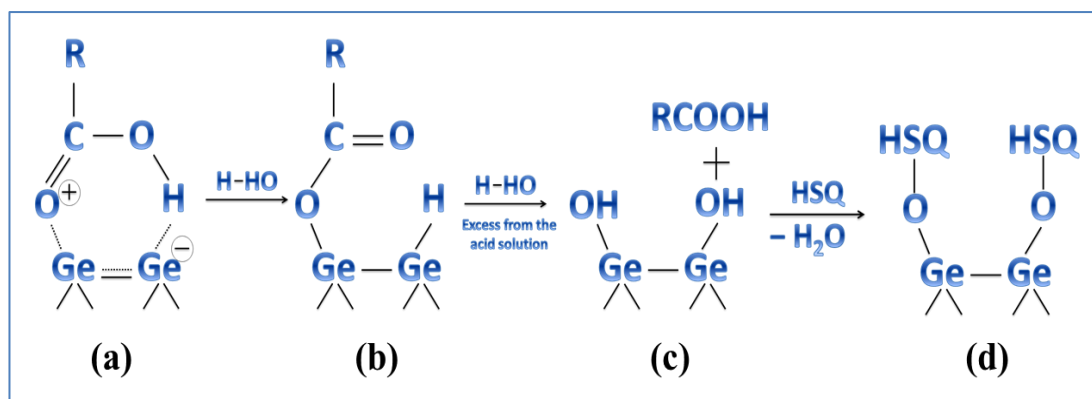
instrument and measurements taken.

Figure 4.3 shows FTIR spectra obtained from a Ge ATR crystal passivated with citric and acetic acids. The spectra obtained were generally noisy due to contributing IR signals from water molecules, since the measurements were undertaken in an ambient atmosphere. The wide peaks in both plots at  $3200\text{ cm}^{-1}$  denote the high availability of OH groups from the acids as well as moisture. Strong C=O peaks, a characteristic stretch of a carboxylic group, were also revealed around  $1700\text{ cm}^{-1}$  in both the spectra. Peaks positioned at  $1250\text{--}1150\text{ cm}^{-1}$  can be assigned to C-(OH) stretching and C-O-H bending modes from the acids.<sup>14</sup> The IR spectra suggested that the Ge surface is functionalised by citric acid and acetic acid.



**Figure 4.3.** FTIR spectra of a Ge composed ATR crystal treated with citric acid and acetic acid for 60s each. The presence of characteristic peaks shows the passivation of the Ge by the acids.

This result correlates with a study of reactions of carboxylic acids on Ge surfaces, where it was reported that on treating Ge with various acids, these acids can be adsorbed onto a Ge surface.<sup>15</sup> This adsorption was confirmed by the dissociation of O–H groups of the carboxylic acid. A stable intermediate carbonyl oxygen dative-bonded state was formed, which is a phenomenon also reported in other studies of organic reactions on Ge surface.<sup>16</sup> The final product reported in the cited study, which formed by O–H dissociation, is Ge–O–COR on the Ge surface. However, it should be noted that in the referenced work the acids used were undiluted with DI water. In the present work the acids were diluted with DI water to obtain different acid concentrations. However, the absence of a Ge–O bond in the Ge 3d XPS spectra (Figure 4.2(a)) suggests that citric acid was not attached to Ge surfaces with a Ge–O–C linkage. This kind of behaviour was also reported in a study on the passivation of Ge surfaces for thiol functionalisation.<sup>17</sup> Moreover, a Ge–H bond is also not present in the FTIR spectra which should have been observed at around  $2070\text{ cm}^{-1}$ .<sup>18</sup> The most plausible explanation could be that since the acids used were dilute, the product formed after OH dissociation of the carboxylic acid may further undergo hydrolysis in the solution to give Ge–OH linkage on the Ge surface. This process must be rapid and hence the Ge–O–C bond was undetected by both FTIR and XPS analysis. When HSQ resist is deposited on the passivated Ge surface, the Ge–OH group can readily react with the silanol groups present in the HSQ to give Ge–O–Si bonding. The silanol groups from the HSQ were previously reported to react with Ge–OH via a condensation reaction during pre-bake and electron beam exposure.<sup>6</sup> The reactions could be summarised as follows:



**Scheme 4.1.** Proposed reaction pathway of Ge surface functionalisation with carboxylic acids and subsequent bonding with HSQ resist.

Of note, the presence of water was necessary for the process to work. When Ge substrates were treated with pure acetic acid solution, the HSQ structures did not remain on the surface. Scheme 4.1 shows that water is necessary to form the Ge–OH linkage on the surface which forms the strong linkage site with HSQ.

Ge surfaces terminated with Cl groups are hydrophilic in nature.<sup>19</sup> Cl termination of Ge substrates, as mentioned previously, has been successful for patterning HSQ on Ge by EBL.<sup>10</sup> Similarly, from our results the removal of oxides and then carboxylic passivation makes the Ge surface hydrophilic and suitable for adhesion of HSQ. The contact angle measured on citric acid treated GeOI substrate was 54.7°/57.2° (left/right angle) and that measured for acetic acid treated GeOI was 50.3°/52.1°, depicting that acetic acid makes the surface slightly more hydrophilic than citric acid (1:3 concentrations) (contact angle of untreated GeOI is 59.6°/60.3°). As reported previously, the age of HSQ resist plays an important role in its adhesion to any surface,<sup>6</sup> as also noticed in our study. When the resist was used beyond its shelf-life on acid passivated substrates, the exposed structures did not adhere to Ge surfaces

after development. A possible explanation for this is that when the HSQ polymer ages, the Si–H bonds start to cross-link instead forming a network within the resist. This process releases hydrogen gas, reducing the Si–H sites in the HSQ to bond with a surface. This consideration indicates that Si–H groups in HSQ are the sites of cross-linking to acid-treated surfaces as uprooting of exposed structures was observed when aged HSQ resist were used.

#### 4.1.4 Lithographic Quality

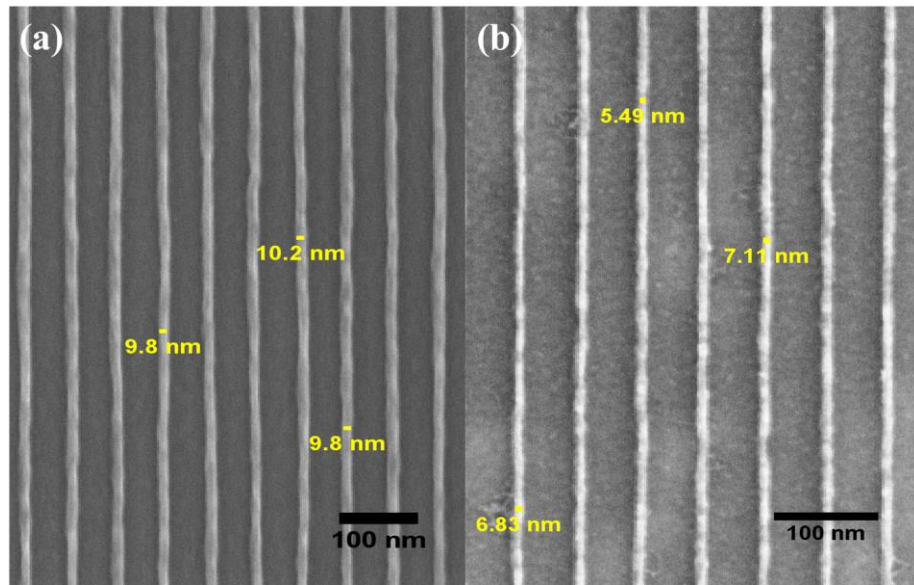


**Figure 4.4.** Sub-10 nm HSQ lines with 60 nm pitch size on GeOI treated with (a) 0.86 M citric acid and (b) 2.75 M acetic acid.

A pattern of 50 nm gratings was exposed on GeOI substrates treated with the concentrations mentioned in Table 4.1. Acid concentrations as low as 0.43 M for citric acid and 1.38 M for acetic acid were able to successfully bind HSQ structures

onto Ge surfaces, efficaciously removing germanium oxides. In order to test the effectiveness of the acids in removing surface oxides on critical patterning, single pixel lines (SPLs) were exposed on GeOI substrates treated with 1:6 concentrations of both acids. The SPLs were exposed at 10 kV and 1000 pC/cm by varying the dose factor of the pattern. The gratings exposed had pitch sizes of 40, 60, 80, 100 and 200 nm. Nanodots of 30, 50 and 100 nm were also exposed with a basic dose of 1000  $\mu\text{C}/\text{cm}^2$  and varying dose factors. The SEM images of high resolution gratings are shown in Figure 4.4. Sub-10 nm lines, down to as low as 5 nm, could be fabricated very conveniently with HSQ on both acid treated Ge surfaces. Figure 4.4(a) illustrates the critical resolution attainable with citric acid, which was 9 nm with 60 nm pitch sizes, whereas Figure 4.4(b) shows the critical dimension of ~5 nm width achievable with acetic acid. The smallest linewidth resolved on citric acid treated GeOI substrates was slightly wider, *i.e.* 9 nm, as lower doses resulted in under-exposed features. To the best of my knowledge, this is the first time that ~5 nm top-down fabricated structures have been presented on a Ge surface. Moreover, the thickness of the resist used was 50 nm, so a good aspect ratio of 1:10, with respect to the linewidth, was obtained with the resist. Previously reported smallest features, 4.5 nm, achieved with HSQ resist were on Si surface and with ultrathin resist films of 10 nm.<sup>20</sup> 7 nm HSQ lines have also been reported on Si using, yet again, a 10 nm thin resist film, exposed at 100 kV and developed with TMAH developer.<sup>21</sup> Thus acid treatments developed in this study not only creates an oxide free Ge surface but also positively passivates the Ge surface, resulting in strong adhesion of HSQ resist to a Ge substrate during EBL exposure and development, irrespective of dimensions.



The high resolution structures were then etched into the top Ge layer of the substrates to quantify the pattern transfer process as well as the stability of acid treatment under chlorine reactive ion etching (RIE). The acid treatment did not interfere with the etch process which can be seen in the SEM images in Figure 4.5.

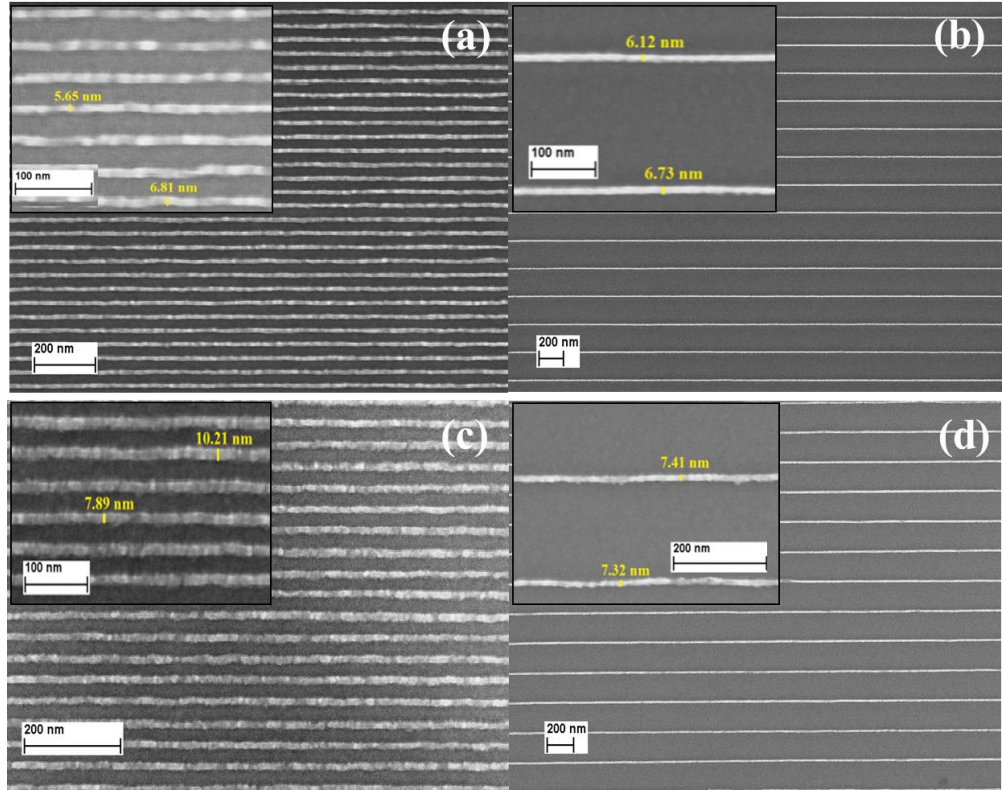


**Figure 4. 5.** SEM images of Ge nanowires etched to a depth of  $\sim 50$  nm into GeOI substrates by RIE with  $\text{Cl}_2$  chemistry: (a) and (b) are generated on acetic acid treated surfaces having 40 and 200 nm pitch sizes, respectively; (c) and (d) are generated on surfaces treated with citric acid having 40 and 200 nm pitch sizes, respectively. All insets show the critical dimension values.

Figure 4.5 shows that patterns were successfully transferred into 50 nm thick Ge layers. The inset of Figure 4.5(a) shows the highest resolution Ge nanowire of 5.7 nm width. All of the Figure 4.5 insets show sub-10 nm wide, and about 50 nm



high, Ge nanowires that were transferred successfully without causing collapse of the nanostructures. The aspect ratios (ratios between height and width) of all the nanowires produced were between 6 and 10.

## 4.2 APPLICATIONS

The simple passivation methods described above were employed to pattern Ge and GeOI substrates for varied applications, such as (i) the fabrication of four-probe test device structure (Figure 4.1(d)), (ii) suspended Ge nanowires for studying strain induced changes in the properties of Ge and (iii) HSQ guides for the directed self-assembly of block copolymers.

### 4.2.1 Four probe nanowire device fabrication

Patterned Ge substrates were used to investigate resistance changes in top-down fabricated Ge FinFETs and substrates by a non-destructive dopant in-diffusion process. This study was undertaken in collaboration with Dr. Ray Duffy at the Tyndall National Institute, UCC. The dopant infusion of phosphine and arsine in Ge was performed by metal organic vapour phase epitaxy (MOVPE). The novelty of the work firstly lies in the fabrication method for forming the Ge Fins and secondly in the in-diffusion approach for doping non-planar Ge devices; to-date Ge FinFETs were doped by ion-implantation. A schematic representation of the entire process flow used to process the Ge nanowires on GeOI substrates can be seen in Figure 4.6(a). The device structure consisted of nanowires of widths varying from 1000 to 20 nm, which were connected to the four probes (Figure 4.6(b)) or to the contact pads by two outer electrodes and two inner electrodes as seen in Figure 4.6(c). The current was forced into the nanowires from the outer electrode and the voltage drop

across the nanowires was measured by the inner two electrodes. The GeOI substrates were firstly degreased, as explained in Chapter 2, Section 2.2.2 of this thesis. The substrates were treated with 0.74 M citric acid for 5 min and subsequently the resist was processed as described in Chapter 2, Section 2.2.2 of this thesis. The fabrication process was a two-step patterning procedure. As mentioned in Chapter 1, Section 1.3.4 of this thesis, to reduce the EBL writing time, the high-resolution structures, *e.g.* nanowires, and the electrodes were patterned using a 10 kV beam, 30  $\mu\text{m}$  aperture size, beam spot size of 2 nm and a 100  $\mu\text{m}$  size write-field. The base electron beam dose employed was  $1000\text{ }\mu\text{C}/\text{cm}^2$  and different dose factors were assigned to different nanowires widths. These settings ensured a good beam size and lower deflection of the beam to avoid unwanted widening of the critical structures. The resist was then developed using the salty developer described in Chapter 2, Section 2.2.2 of this thesis and imaged. To pattern the low-resolution contact pads, the pre-patterned substrates were again immersed in 0.74 M citric acid for 5 min and the resist was spin-coated on. The citric acid did not affect the patterned HSQ structures in any case. Since the size of the structures in the second lithography step were not critical, the following parameters were used: a 1 kV beam, a 120  $\mu\text{m}$  aperture, 12 nm beam size, a 400  $\mu\text{m}$  write-field and an electron dose of  $200\text{ }\mu\text{C}/\text{cm}^2$ . The EBL writing time was reduced immensely due to the lower electron dose, larger aperture size and larger write-field. In this manner, the four-probe test structures were fabricated. To transfer the HSQ pattern into the top Ge layer of the GeOI substrates, they were subjected to RIE using  $\text{Cl}_2$  chemistry for 25 s (Chapter 2, Section 2.1.2 of this thesis).<sup>22</sup>

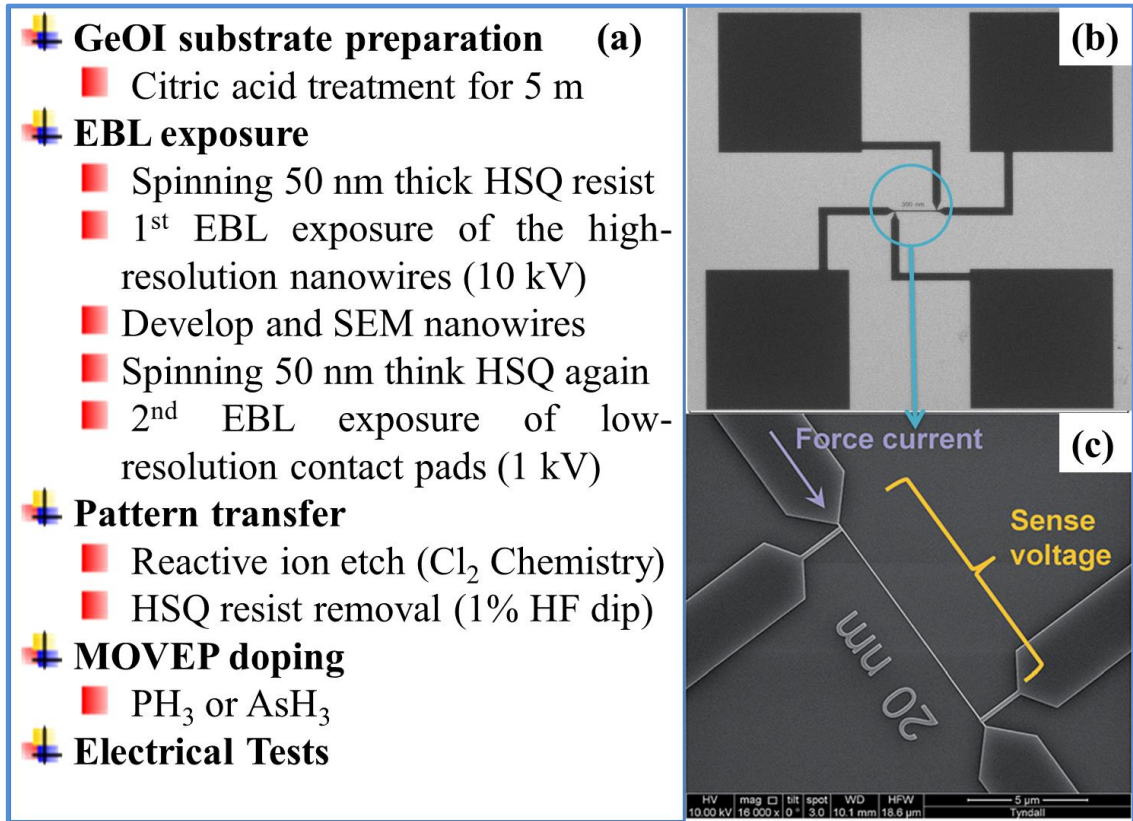


**Figure 4.6.** (a) Schematic representation of the process flow used to process the Ge nanowires on GeOI substrates. (b) 4 point probe HSQ test structure were patterned by acetic acid or citric acid treatment of GeOI substrates, (c) representative top view SEM image of the Ge test structure. In the test structure current was forced through the outer electrodes and the voltage drop across the nanowire was sensed by the inner 2 electrodes. From this current–voltage relationship the resistance was extracted. In this image a 20 nm wide structure is shown.

After stripping the remaining resist and immersing the GeOI chips in 1% HF solution, the nanowires were exposed to  $\text{PH}_3$  or  $\text{AsH}_3$  at a temperature of 650 or 700 °C in a MOVPE chamber. Current-voltage curves were analysed for the doped and undoped Ge nanowires, which depended on assuming current flow within the

nanowires cross-sections. Current could primarily flow along the edges of the nanowires, valid for a condition where active doping is the highest. In this case the electrical width ( $W_{electrical}$ ) of the device was then calculated according to the equation (4.1):

$$W_{electrical} = 2H_{fin} + W_{fin} \quad (4.1)$$

where  $H_{fin}$  is the height of the fin, and corresponds to the thickness of the Ge on the GeOI wafer.  $W_{fin}$  is the width of the fin. The resistance of the fin ( $R_{fin}$ ) is calculated according to equation 4.2:

$$R_{fin} = \frac{V}{I/W_{electrical}} = \frac{V}{I} (2H_{fin} + W_{fin}) \quad (4.2)$$

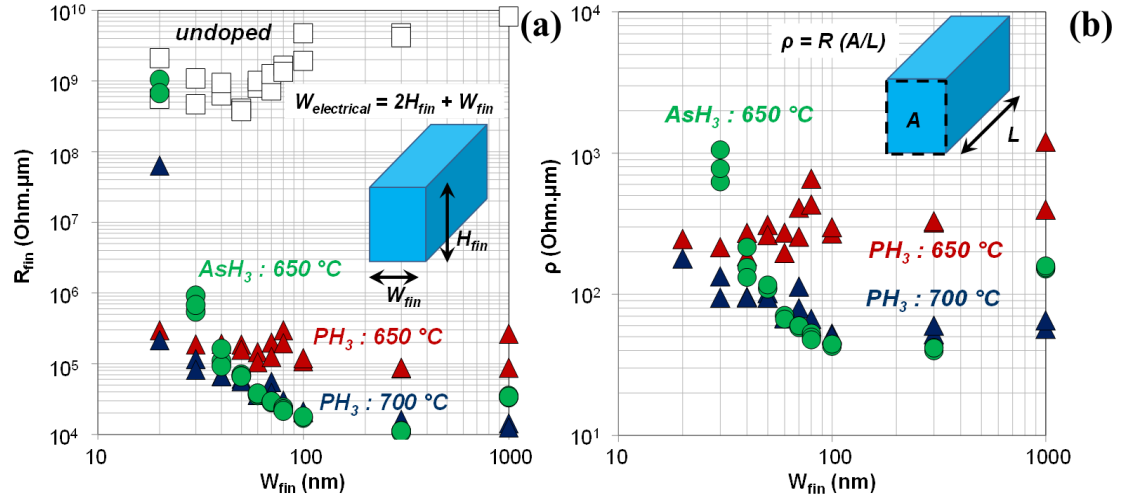


**Figure 4.7.** (a)  $R_{fin}$  vs.  $W_{fin}$  plot for Ge nanowires doped at 650 or 700 °C using  $\text{PH}_3$ , or doped at 650 °C using  $\text{AsH}_3$ . (b)  $\rho$  vs.  $W_{fin}$  for Ge nanowires doped at 650 or 700 °C using  $\text{PH}_3$ , or doped at 650 °C using  $\text{AsH}_3$ .

Figure 4.7(a) illustrates the resistance across the nanowires extracted from equation 4.2, prior to and after doping by MOVPE. The access resistance of the doped nanowires drops by 4-5 orders of magnitude compared to the undoped nanowires. For both dopants, as the width of the nanowires decreased their resistance gradually increased. Both the P and As-based dopants gave similar resistances for nanowires with widths larger than 50 nm. A MOVPE temperature of 650 °C was not high enough temperature for the P-based process, as the resistance was significantly lowered upon increasing the process temperature to 700 °C. As the widths of the Ge nanowires were scaled down, their resistance was expected to rise, as has been shown many times for Si nanowires and FinFETs. In this regard, the AsH<sub>3</sub>-based MOVPE process gave unexpected results, as the resistance of the Fins increased sharply around  $W_{fin} = 40$  nm. In contrast, the PH<sub>3</sub> doped nanowires could be scaled below 40 nm.

A second way to analyse the electrical parameters of the nanowires (fins) is to assume that the current flows uniformly throughout the cross-section of the nanowire. From theory on metal interconnects (Ref), equation 4.3 can be deduced:

$$\rho = R \frac{A}{L} \quad (4.3)$$

where  $\rho$  is the resistivity of the material,  $A$  is the area of cross section and  $L$  is the length of the nanowires. The resistivity vs fin width plot is illustrated in Figure 4.7(b) where  $\rho$  is extracted using equation 4.3. The trends in resistivity for the

doped nanowires are similar to the previous analysis shown in Figure 4.7(a), where surface conduction was assumed. MOVPE at 700 °C was confirmed to be better for the P doping process, the two dopant species produce similar results for wide devices, and the P-based process was a better choice for downscaled features.

Thus, this section highlighted a non-destructive dopant infusion method demonstrated on Ge test structures patterned successfully by citric acid treatment. The acid treatment not only allowed the fabrication of good high-resolution structures but also did not interfere with further processing. The dopant infusion successfully reduced the access resistance to the nanowires as compared to the undoped nanowires.

### 4.2.2 Suspended Germanium Nanowires

This study involved fabricating Ge nanowires by EBL to study their strain induced properties in collaboration with Prof. Jean-Pierre Raskin from Université catholique de Louvain, Belgium. Ge nanowires, approximately 50 nm wide, were firstly fabricated on GeOI substrates. Figure 4.8(a) is an illustration of a single test *nanomachine* where the Ge stem (blue) was the anchor for Ge nanowires, 10 µm in length, on one end, that were suspended by metal connects (purple), on the other end.

The lithography process involved two exposures wherein the Ge bulk stem and the nanowires were exposed first with HSQ to transfer the pattern into the top Ge layer of the GeOI substrate. In order to deposit the metal contacts, the second lithography step was performed using SML resist for the metal lift-off procedure. The Ge

nanowires were fabricated by passivating the surface with either 2.35 M acetic acid or 0.74 M citric acid. Figure 4.8(b) illustrates nanowires fabricated using acetic acid.

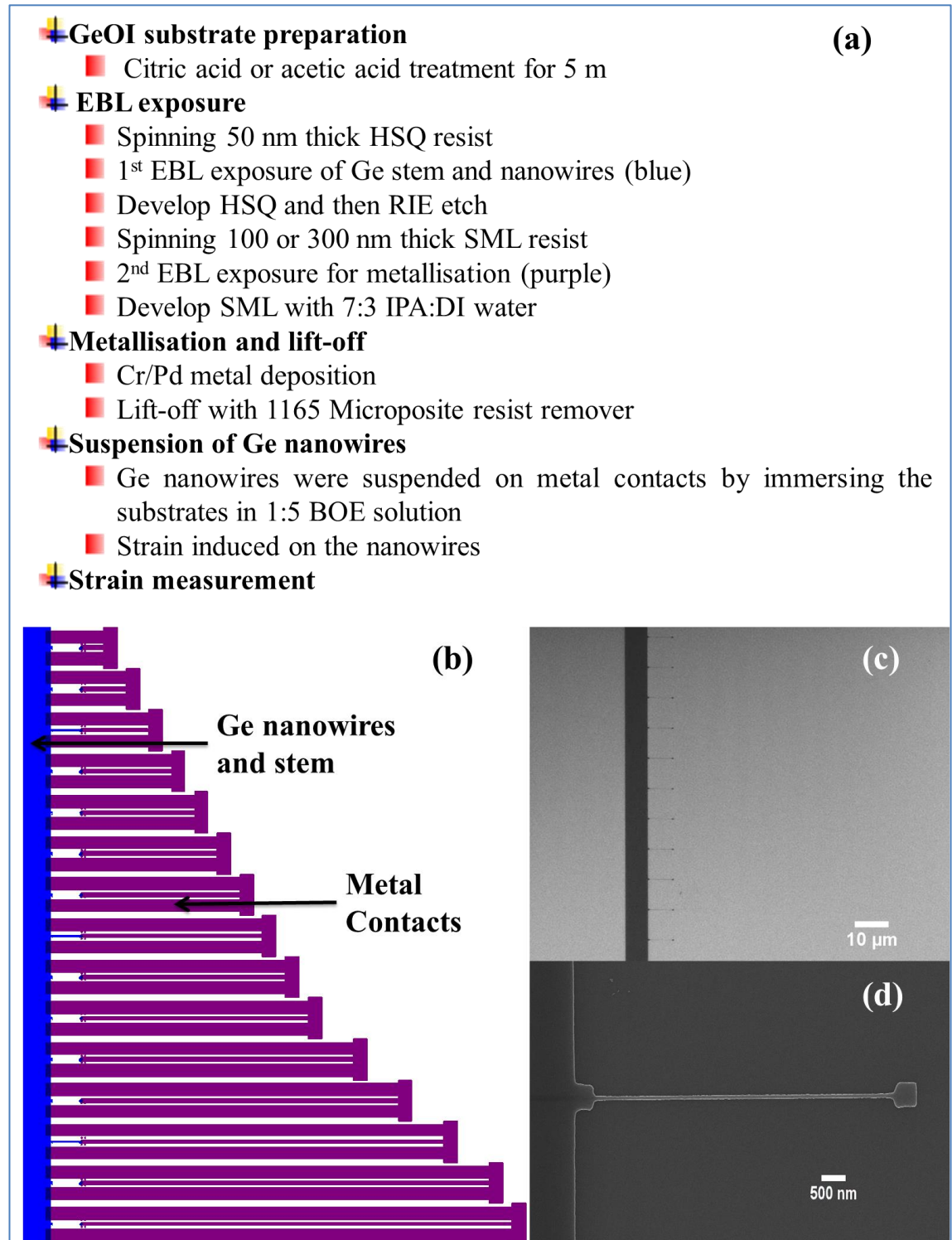


**Figure 4.8.** (a) Process flow of the nanofabrication process of the Ge nanomachines  
(b) Graphic illustration of a nanostructure showing the bulk Ge (blue) anchoring Ge



*nanowires, (c) HSQ nanowires patterned after 2.35 M acetic acid treatment of a GeOI substrate and (d) a Ge nanowire obtained after a RIE etch process.*

The high brightness of the unpatterned area can be seen in Figure 4.8(b), which is due to the surface adsorption of acetic acid. The nanowires were then etched into the top Ge layer by a  $\text{Cl}_2$  RIE for 25 s, as mentioned in Chapter 2, Section 2.1.2 of this thesis. A sample nanowire after etching is illustrated in Figure 4.8(c), showing that the etch process was not affected by the presence of acetic acid adsorbed onto the substrate surface. In the next fabrication step, SML 100 or SML 300 was spin-coated onto the pre-patterned substrates as described in Chapter 2, Section 2.2.1 of this thesis. The second layer was aligned carefully to the first layer as the overlay of the head of the nanowires needed to be precise under the metal connects. Figure 4.9(a) shows the SEM images of a whole nanomachine taken after developing the SML resist. SML 100 (Figure 4.9(b)) gave a better resist clearance from the surface compared to SML 300 (Figure 4.9(c)), where resist residues were clearly visible. Patterned substrates were then subjected to metal evaporation of Cr/Pd layers. On a few substrates Cr/Pd (5 nm/80 nm) was deposited and on others, Cr/Pd (5 nm/25 nm) was deposited. The metal was lifted-off by submerging the substrates into 1165 Microposit resist remover. The metal strip would thus lay on the head of the Ge nanowires. The next step was to release the Ge nanowires, with the help of mild buffered oxide etch (BOE) in a 1:5 ratio with DI water. The mild BOE can etch the  $\text{SiO}_2$  laying underneath the nanowires in a controlled manner. When the structures were released by wet etching of the underlying  $\text{SiO}_2$ , the metal stripes pulled on the Ge nanowires and induce strain within them. This induced strain was dependent on the length of the metal stripes and influenced the mechanical properties of the Ge



nanowires, as shown in Figure 4.8(a). The next step would be to analyse the change in the nanowire properties as a function of strain, which is currently being undertaken at Belgium by Jean-Pierre Raskin.

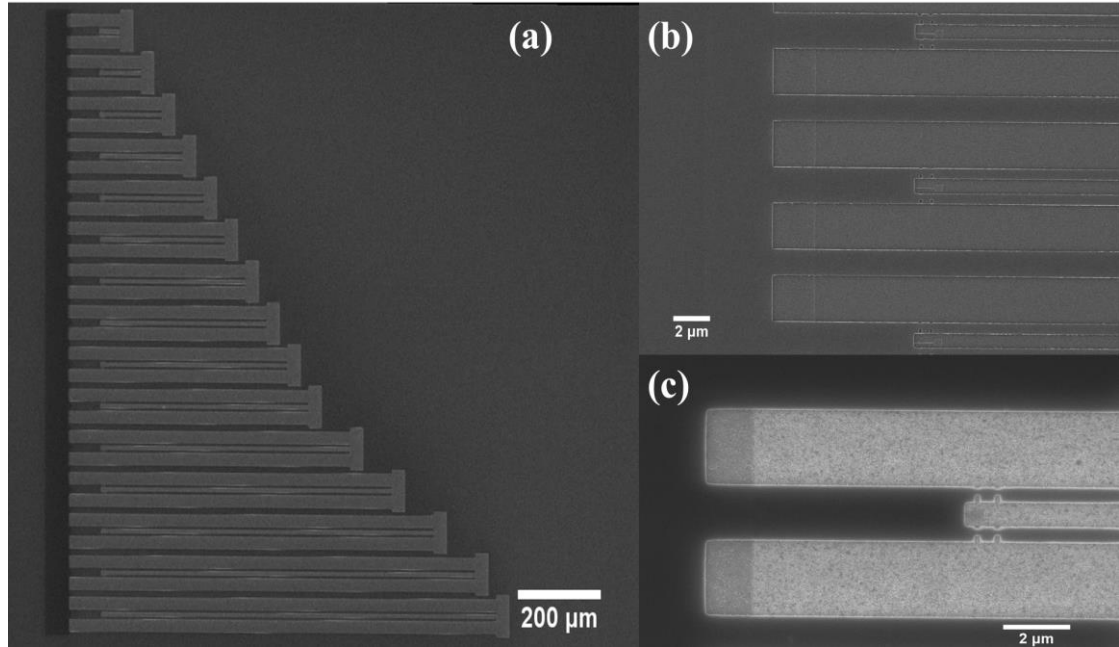


**Figure 4.9.** (a) Complete nan-structure after both lithographic processes, nanowires seen underlying in the resist opening in (b) SML 100 and (c) SML 300 resist for metal lift-off.

### 4.2.3 Patterning for directed self-assembly of block copolymers

Top-down EBL technology is extremely reliable at achieving high-resolution lithography, down to 5 nm width feature size and below. However, when it comes to increasing pattern density, the EBL suffers from intrinsic limits, such as the proximity effect and resist properties. To combat these issues, the self-assembly of block copolymers (BCP) is being utilised in nanolithography. As mentioned in Chapter 1 of this thesis, a BCP can form periodic patterns on large surface areas that can be used as etch-masks. They can self-assemble into various shapes such as

spheres, cylinders, lamella and gyroids depending on the compositions of the two polymers. However, the self-assembly of BCPs is rather random on planar surfaces and requires interference to guide the assembly. Patterning the surface with trenches or posts topologically by top-down fabrication methods can provide such guidance. This process is known as the directed self-assembly (DSA) of BCPs. DSA on Si and a few other materials have been demonstrated in the past.<sup>23,24</sup> However, DSA on Ge has very been reported in this Thesis for the first time with two BCP systems, namely poly (styrene-*b*-ethylene oxide) (PS-*b*-PEO) and poly (styrene-*b*-4 vinyl pyridine) (PS-*b*-P4VP).

HSQ trenches were patterned on Ge and GeOI substrates to act as guidance. Arrays of HSQ lines with 50 nm width were patterned with various spacing between the lines. The DSA of BCP on Ge surface is discussed in depth in Chapter 5 of this thesis. Figure 4.9 illustrates the DSA of PS-*b*-P4VP on Ge substrates. Figure 4.10(a) shows the BCP that phase-separate to form long lamellar domains, which are arranged in a “finger-print” formation. When HSQ trenches are introduced, the lamellar structures arrange parallel to the HSQ lines. It can be seen, as the trench size increases from Figure 4.10(b) to (d), the number of the BCP lines contained in the HSQ trenches have increased. Thus, increased in pattern density can be achieved by the simple DSA of BCPs within top-down lithography guided patterning. The substrates were exposed in the EBL by treating the substrates with citric acid prior to HSQ deposition. A  $\text{Fe}_3\text{O}_4$  hardmask was subsequently formed on the BCP structures, as described in Section 2.2.3 of Chapter 2. The hardmask was then used to transfer the pattern into the Ge substrate via etching. Figure 4.10 (e) shows the Ge fins achieved successively by pattern transfer. To conclude in brief, the surface

passivation with citric acid or acetic acid for the HSQ exposure was successful and did not interfere with the self-assembly of the BCP in the later processing steps.

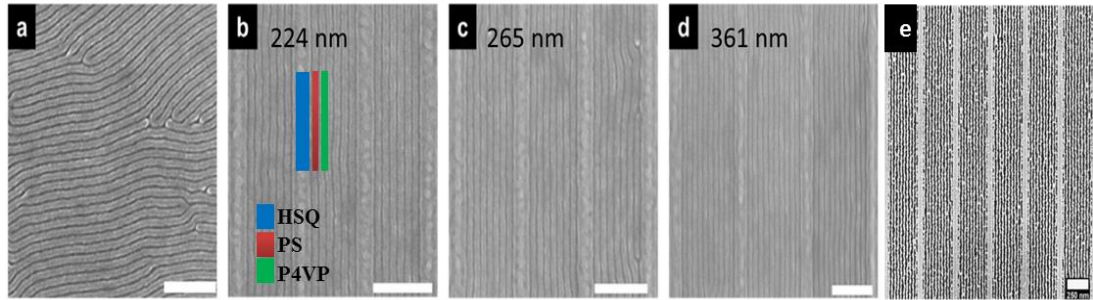


**Figure 4.10.** Graphoepitaxy with PS-*b*-P4VP BCP system on HSQ templated Ge surface. (a) Finger-print BCP structures on unpatterned Ge surface. Alignment of the BCP within HSQ trenches of sizes (b) 224 nm, (c) 265 nm and (d) 361 nm, (e) parallel arrays of pattern transferred Ge nanofins in channel widths of 361 nm (Scale bar 250 nm).<sup>25</sup>

### 4.3 CONCLUSIONS

A novel, simple, effective and safe process to fabricate nanoscaled patterns on Ge surfaces with EBL using the negative tone resist HSQ has been developed. The chemical nature of the untreated Ge surface does not allow competent EBL patterning with this high resolution resist. The use of “common” acid treatments to clean and passivate Ge surfaces makes them favourable for good adhesion of HSQ resist after EBL exposure and salty solution development processes. Two acid solutions, citric and acetic acid, have been shown to successfully remove native Ge oxides and further passivate Ge surfaces with carboxylic groups. The efficacy of this route was also validated on GeOI substrates. The proposed process is simpler and cheaper than previously used methods and is non-hazardous in all manners. Using this process, Ge nanowires with widths down to 5 nm and heights of 50 nm were

successfully been patterned on GeOI substrates. To the best of my knowledge, these are by far the smallest top-down fabricated Ge nanostructures reported to date. Moreover, the application of this Ge patterning process to fabricate nanodevices also proves its compatibility with semiconductor nanofabrication. The removal of native Ge oxides presented here can also aid other studies and processes that require working with oxide-free Ge surfaces.

### 4.4 BIBLIOGRAPHY

1. B. Kaleli, A.A.I. Aarnink, S.M. Smits, R.J.E. Hueting, R.A.M. Wolters, J. Schmitz. In *STW.ICT Conference*, 2010, 106.
2. S. Choi<sup>1</sup>, M.J. Word, V. Kumar, I. Adesida. *J. Vac. Sci. Technol. B.* 2008, **26**, 1654.
3. A.Z. Khokhar, D.S. Macintyre, F. Rahman, R.M. De La Rue, N.P. Johnson. *IEEE/LEOS Winter Topicals Meeting Series*, 2009, pp 56 – 57.
4. Z. Zhang, H. Duan, Y. Wu, W. Zhou, C. Liu, Y. Tang, Haiwen Li. *Microelectronic Eng.* 2014, **128**, 59.
5. R.G. Hobbs, S. Barth, N. Petkov, M. Zirngast, C. Marschner, M.A. Morris, J.D. Holmes. *J. Am. Chem. Soc.* 2010, **132**, 13742.
6. R.G. Hobbs, M. Schmidt, C.T. Bolger, Y.M. Georgiev, P. Fleming, M.A. Morris, N. Petkov, J.D. Holmes. *J. Vac. Sci. Technol. B*, 2012, **30**, 041602.
7. G. Collins, J.D. Holmes. *J. Mater. Chem.* 2011, **21**, 11052.
8. G. Collins, P. Fleming, C. O'Dwyer, M.A. Morris, J.D. Holmes. *Chem. Mater.* 2011, **23**, 1883.

9. G.M. Schmid, L.E. Carpenter, J. A. Liddle. *J. Vac. Sci. Technol. B.* 2004, **22**, 3497.
10. R.G. Hobbs, J.D. Holmes, N. Petkov. *Methods and materials for lithography of a high resolution HSQ resist*, Google Patents. 2012.
11. R. Yu, S. Das, R.G. Hobbs, Y.M. Georgiev, I. Ferain, P. Razavi, N.D. Akhavan, C.A. Colinge, J. Colinge. *Ultimate Integration on Silicon (ULIS)*, 2012 13th International Conference. 145 – 14.
12. H. Jagannathan, J. Kim, M. Deal, M. Kelly, Y. Nishia. *ECS Transactions.* 2006, **3**, 1175.
13. R. Yu, Y.M. Georgiev, S. Das, R.G. Hobbs, I.M. Povey, N. Petkov, M. Shayesteh, D. O'Connell, J.D. Holmes, R. Duffy. *Phys. Status Solid Rapid Research Letters.* 2014, **8**, 65.
14. I.A. Mudunkotuwa, V.H. Grassian. *J. Am. Chem. Soc.* 2010, **132**, 14986.
15. M.A. Filler, J.A. Van Deventer, A.J. Keung, S.F. Bent. *J. Am. Chem. Soc.* 2006, **128**, 770.
16. P.W. Loscutoff, S.F. Bent. *Annu. Rev. Phys. Chem.* 2006, **57**, 467.
17. G. Collins, D. Aureau, J.D. Holmes, A. Etcheberry, C. O'Dwyer. *Langmuir*, 2014, **30**, 14123.
18. <https://www2.chemistry.msu.edu/faculty/reusch/virttxtjml/Spectrpy/InfraRed/irspect1.htm>
19. S. Sun, Y. Sun, Z. Liu, D.-I. Lee, S. Peterson, P. Pianetta. *Appl. Phys. Lett.* 2006, **88**, 021903.
20. J. K.W. Yang, B. Cord, H. Duan, K.K. Berggren, J. Klingfus, S.-W. Nam, K.-B. Kim, M. J. Rooks. *J. Vac. Sci. Technol. B*, 2009, **27**, 2622.
21. A.E. Grigorescu, M. Van der Krogt, C.W. Hagen, *Proc. SPIE*, 2007, **6519**,

65194A.

22. R. Duffy, M. Shayesteh, K. Thomas, E. Pelucchia R. Yu, A. Gangnaik, Y.M. Georgiev, P. Carolan, N. Petkov, B. Long, J.D. Holmes. *J. Mater. Chem. C.* 2014, **2**, 9248.
23. S.-J. Jeong, J.Y. Kim, B.H.Kim, H.-S. Moon, S.O. Kim. *Mater. Today.* 2013, **16**, 468.
24. C. Cummins, D. Borah, S. Rasappa, A. Chaudhari, T. Ghoshal, B.M.D. O'Driscoll, P. Carolan, N. Petkov, J.D. Holmes, M.A. Morris. *J. Mater. Chem. C.* 2013, **1**, 7941.
25. C. Cummins, A. Gangnaik, R. Kelly, A. Hydes, J. O'Connell, N. Petkov, Y.M. Georgiev, D. Borah, J.D. Holmes, M.A. Morris. *J. Mater. Chem. C.* 2015, **27**, 6091.

## CHAPTER 5

---

# **DIRECTED SELF-ASSEMBLY OF BLOCK COPOLYMERS ON Si AND Ge SURFACES**

## 5. DIRECTED SELF-ASSEMBLY OF BLOCK COPOLYMERS ON Si AND Ge SURFACES

Due to the growing demand of high resolution nanolithography, researchers have been motivated to develop new, cost effective and high throughput methods, such as nanoimprint lithography, lithography with block copolymers (BCPs) or dip-pen nanolithography.<sup>1,2,3,4</sup> BCPs consist of two or more blocks of distinct monomers that are chemically different from each other. Due to this difference, the polymer segments phase separate on the nanometre scale, as briefly discussed in Chapter 1, Section 1.5 of this thesis.<sup>5</sup> By varying the molecular weights of the polymers blocks, and by playing with the interaction parameters, excellent control over the BCP domain shape and size can be achieved. Nanoscale shapes such as lamella, spherical, cylindrical or gyroidal can be acquired in this manner. Once the desired orientation is achieved, one of the blocks can be selectively removed and the remaining pattern can be transferred into a functional material.<sup>6,7,8</sup> BCP lithography therefore has the potential to be used to fabricate high density, well-ordered arrays of functional nanostructured materials on substrate surfaces, which is not only scientifically interesting but also a technologically important area; due to potential applications in nanoelectronics, optoelectronics, information storage, photonics, catalysis and sensors.<sup>6,9,10</sup>

One of the major challenges in using BCPs for nanofabrication is the lack of long range periodic ordering of the polymer segments on a substrate. Directed self-assembly (DSA) of BCPs can be achieved however by introducing guiding



structures such as trenches or pillars on the surface of a substrate. These guides have been reported to effectively monitor and improve the ordering of some of the BCP systems.<sup>11,12,13</sup> This category of lithography is known as directed self-assembly by graphoepitaxy. A considerable amount of research has been undertaken to optimise the DSA of BCPs. The DSA of lamellar forming poly (styrene-*b*-methyl methacrylate) (PS-*b*-PMMA) using electron beam lithography (EBL) to produce simple hydrogen silsesquioxane (HSQ) line patterns that act as guides for BCPs has been reported.<sup>14</sup> EBL exposed dot patterns have also been used for administrating the self-assembly of spheres forming BCP from poly (styrene-*b*-dimethylsiloxane) (PS-*b*-PDMS).<sup>15</sup> These dots structures were explored for bit-patterned media with a density of around 1.5 teradots/inch<sup>2</sup>. Other instances of using EBL-patterned HSQ for guiding BCP orientation has also been reported.<sup>16</sup> Besides graphoepitaxy, chemically pre-patterning the surface prior to BCP deposition is also another DSA approach, wherein a brush layer is deposited on the substrate prior to BCP processing.<sup>17</sup>

In this Chapter, a method to generate highly ordered Si and Ge nanopatterns, aligned with the help of simple HSQ gratings fabricated by EBL, via a simple and cost-effective *in-situ* BCP hard mask inclusion technique is demonstrated. The nanofabrication process is based on the use of solvent-induced microphase separation in poly (styrene-*block*-ethylene oxide) PS-*b*-PEO thin films; where the marked difference in the chemical functionality of the PS and PEO blocks allows selective metal ion inclusion.<sup>18</sup> The structural and morphological variation in BCP phase separated patterns can be achieved by changing the solvent annealing time and

temperature of the BCP film, the width and spacing between the gratings and pre-treatment of substrate surface. Unlike several BCP/substrate systems, the PS-*b*-PEO system requires no polymer brush layer to be deposited on a substrate surface. Moreover, this BCP system also serves as an alternative to PS-*b*-PMMA, which offers a minimum pitch size of 30 nm. Smaller molecular weight PS-*b*-PEO can offer a minimum pitch size of 15 nm because of the higher  $\chi$  value than PS-*b*-PMMA. Iron oxide nanopatterns were fabricated from the assembled PS-*b*-PEO polymer, after removal of PEO block, which were subsequently used as hardmasks to transfer nanopatterns into Si or Ge substrates. The fabrication of an iron oxide mask was based on a simple solvation process rather than a complex chemical co-ordination between metal precursors and one of the polymer blocks.<sup>19</sup>

## 5.1 RESULTS

### 5.1.1 DSA with varied conditions on Silicon Substrates

HSQ gratings that were patterned by EBL acted as guiding templates for the self-assembly of the BCP system. The BCP employed in this study was PS-*b*-PEO (42k-11.5k), with PEO as the minority cylinder forming block. The sizes of the trenches were varied in the range of multiples of 45 nm, whereas the depth was fixed at 50 nm (thickness of HSQ resist film). Figure 5.1(a) shows a high magnification SEM image of the HSQ trench prior to BCP patterning. BCP nanopatterns were created by spin-coating the polymer solution onto the trench followed by solvent annealing at different temperatures and time. Note that the concentrations of the polymer solution were calibrated to avoid overfilling of the trenches. For all the experimental conditions studied, a 0.4 wt% polymer-toluene solution was used. The arrangement

of the PS and PEO blocks for the solvent annealed films could not be determined by SEM due to the lack of contrast between the segments under an electron beam. All the films were exposed to anhydrous ethanol, which partially etched the PEO domains and studied by SEM to investigate the DSA of the BCP. An open surface area where the HSQ gratings were not present, showed periodic arrangements of the BCP with PEO cylinders oriented perpendicularly to a substrate surface after solvent annealing at a temperature of 50 °C for 2 h, as shown in Figure 5.1(b).

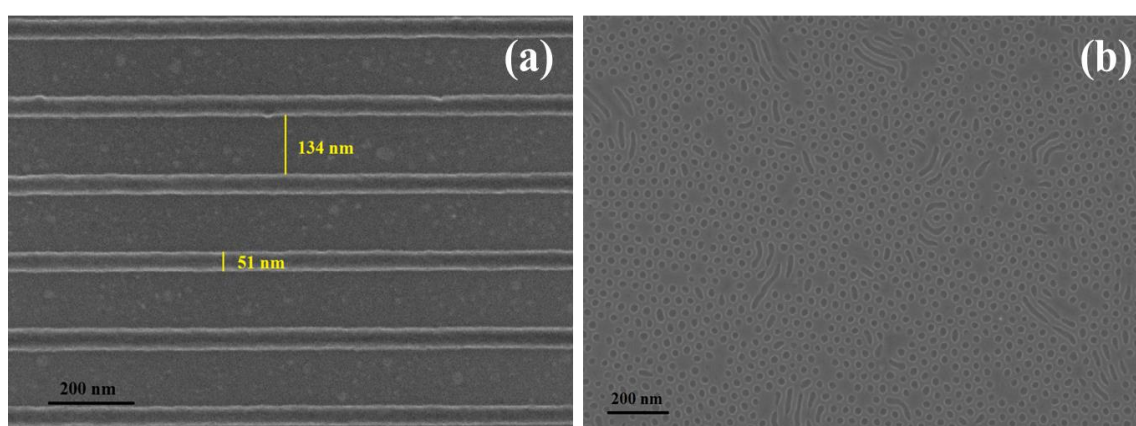


**Figure 5.1.** (a) Array of 50 nm wide HSQ lines with a 135 nm trench size prior to BCP processing and (b) BCP arrangement on an open surface area of a Si substrate.

The BCP exhibited little indication of lamellar patterning within the HSQ trenches. The solvent annealing process was used to achieve vertically oriented cylindrical PEO microdomains in the PS matrix with an annealing temperature of 50 °C and the annealing times were varied between 1.5 and 2 h. The polymer wetted the substrate surface evenly for the wider trench widths (> 135 nm), but no ordering was achieved. Figure 5.2(a) shows an SEM image of a PS-*b*-PEO system after toluene exposure at a temperature of 50 °C for 2 h between a 90 nm trench; which indicates an ordered arrangement over large areas with no or little de-wetting. Subsequently,

the annealing temperature was changed to 60 °C without changing other experimental parameters. An ordered, aligned arrangement of arrays of hexagonal dot patterns were observed within the trenches, but thickness variations and/or pattern degradation was noticed in a few places as shown in Figure 5.2(b) for a 135 nm trench width. The number of rows of PEO dots increased with increasing the trench width. The mean centre-to-centre distance between adjacent microdomains was 42 nm, whereas the PEO cylinder diameter was around 19 nm for both trenches. Thermal annealing of the BCP film at the same temperature in the absence of the solvent had no effect on the as-cast film, demonstrating that toluene was a necessary component to induce phase separation, as illustrated in Figure 5.2(c). Further increasing the annealing temperature, HSQ features seemed to deteriorate, which affects the self-assembled BCP patterns within the trenches.

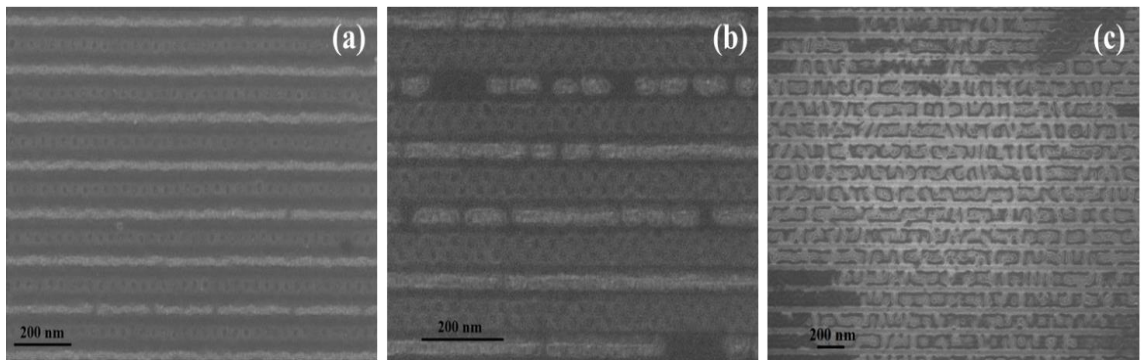


**Figure 5.2.** SEM images showing PS-*b*-PEO arrangements after toluene exposure at a temperature of (a) 50 °C for 2 h within a 90 nm HSQ trench, (b) 60 °C for 2 h within a 135 nm HSQ trench and (c) thermal annealing at 50 °C without solvent for 2 h within 90 nm HSQ trench.

To arrange the structural alignment and orientation of PEO cylinders within the

trenches, careful control of the annealing temperature and time were required. The substrate surface can also be modified to achieve well-ordered periodic features within trenches. Similar experimental conditions were applied for the HSQ etched Si trenches (50 nm depth). The HSQ etching was achieved by RIE using Cl-chemistry for 25 s, as described in Chapter 2, Section 2.1.2 of this thesis.<sup>20</sup> Well-ordered arrays of aligned dot patterns were observed for all of the trenches. Furthermore, better coverage and contrast enhancement was noticed. Figures 5.3(a) and (b) show well defined arrays of dots within 135 and 180 nm wide trenches for BCPs annealed at 60 °C for 1.5 h, respectively. The number of rows formed by the dot arrays increased with increasing trench width. The PEO cylinders were perpendicularly orientated to the substrate surface for all of the trenches studied and no parallel orientation was realised. The Si walls guided the ordering of the cylinders which were otherwise randomly arranged on plain surfaces, as seen in Figure 5.1(b). The cylinder-to-cylinder spacing and PEO cylinder diameter remained unchanged.

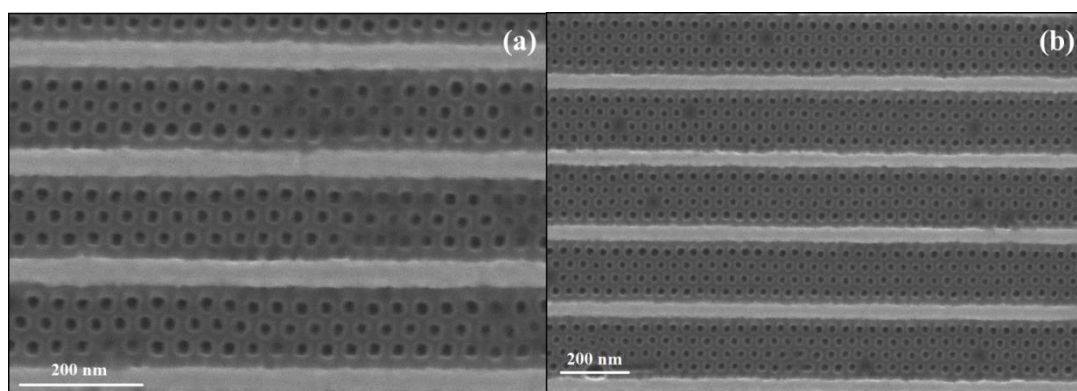


**Figure 5.3.** SEM images of BCP films annealed at 60 °C for 1.5 h within (a) 135 nm and (b) 180 nm wide HSQ etched Si trenches.

To achieve parallel orientation of the cylinders within the trenches, the annealing time was changed to 2 h. No microphase separation was achieved in the smallest trench width (45 nm) as shown in Figure 5.4(a). Increasing the trench width to 90 nm, a single array of a combination of parallel and perpendicular orientated PEO cylinders inside the PS matrix was observed. Figure 5.4(b) shows large scale area BCP nanopatterns, 2  $\mu\text{m}$  long in 90 nm wide trenches. The PEO cylinders resided almost at the middle of the trenches, whereas PS wetted the sidewalls. In the smaller width trenches, due to the limitation of space and majority of the PS block, PS takes the majority of the space and the PEO prefers to be vested between the PS matrixes. Due to crowding of the blocks, they arrange themselves in the trench depending on the mole fractions of the blocks. As the trench size is increased, the wetting preference is governed by the surface energy. Similar mixed orientations of the cylinders was realised by increasing the trench widths to 135 and 180 nm. Moreover, dewetting was not noticed. Further increases in the trench widths resulted in perpendicular orientation of the cylinders only near the edges of the trenches, as shown in Figure 5.4(c) for 270 nm wide trenches. No structures were realised in the intermediate areas of the large trenches. Additionally, frequent defects were observed.

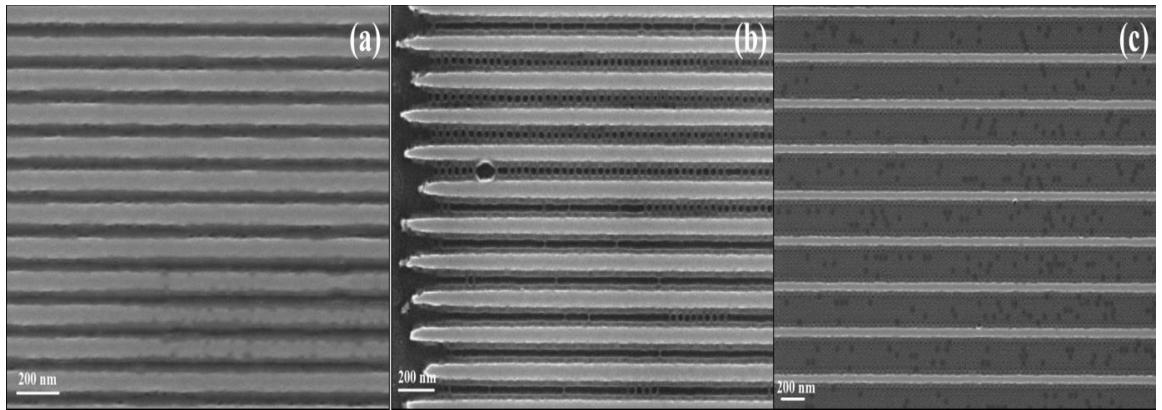


**Figure 5.4.** SEM images of BCP nanopatterns in trenches HSQ etched in the Si substrates after solvent annealing at 60 °C for 2 h with (a) 45 nm, (b) 90 and (c) 270 nm trench widths.

The complex PS-*b*-PEO system exhibits asymmetric affinities for the solid substrate and the air interface and these interfacial energies contribute to the ordering of the BCP nanostructures.<sup>21,22,23</sup> Previous works suggests that the hydrophilic PEO will preferentially wet the substrate surface (favourable PEO-substrate interactions) whilst PS will segregate to the air interface to form a PS-rich layer (PS has a lower surface energy,  $\gamma_{PS} = 33 \text{ mNm}^{-1}$ ;  $\gamma_{PEO} = 43 \text{ mNm}^{-1}$ ).<sup>23</sup> Although PEO dissolves in toluene, toluene is a selective solvent for PS since, the solubility parameter difference with PS is much smaller ( $\delta_{Tol} - \delta_{PS} = 18.3 - 18 = 0.3 \text{ MPa}^{1/2}$ ) than the one of PEO ( $\delta_{Tol} - \delta_{PEO} = 18.3 - 20.2 = 1.9 \text{ MPa}^{1/2}$ ).<sup>23</sup> The high resident time of toluene in the polymer films provides sufficient mobility to induce microphase separation.<sup>24,25</sup> Thus, the annealing time is prolonged and the temperature, 60 °C, is kept near the melting point of PEO, which is 55 °C for this BCP system.<sup>23</sup> On the other hand, shorter annealing times chiefly favour perpendicular orientation of the PEO block. During the annealing, PEO remains in a semi-molten state and



microphase separation will occur orienting PEO into hexagonal array perpendicular to the surface in the PS matrix (in unpatterned areas). Although, in the HSQ defined areas, the microphase separation of the BCP is influenced by topographical confinements.

Good contrast in the SEM images was not difficult to obtain of the HSQ etched trenches (Figure 5.4). As oppose to this, the images obtained with HSQ resist as sidewalls provide less contrast and poor focus (Figure 5.2). One of the explanations for the contrast variance other than the height differences could be attributed to the densities of the BCP components. Solvent annealing of the BCP films prevents the crystallisation of PEO and prior to ethanol treatment, the densities of PS ( $1.05 \text{ g/cm}^3$ ) and PEO ( $1.12 \text{ g/cm}^3$ ) were similar, hence a lack of contrast is observed.<sup>26</sup> PEO crystallisation occurs after ethanol treatment and its density increases to  $1.24 \text{ g/cm}^3$  and so better contrast difference between the two polymer blocks is observed. Consequently, SEM analysis was easier.

In order to modify the substrate chemistry and to achieve the parallel orientation of PEO cylinders, the HSQ trenched Si substrates were subsequently exposed to uv/ozone treatment for 30 min before spin-coating of the BCP solution. This step makes the surface more hydrophilic; the water contact angle for Si is reported to be  $21^\circ$ , whereas after UV/ozone treatment the contact angle was found to be  $0^\circ$ .<sup>27</sup> A hydrophilic Si surface promotes the formation of Si-OH bonds which have a high affinity for the PEO block in both the trenches and the HSQ sidewalls. After spin-coating the BCP films, the substrates were solvent annealed for 1.5 h and 2 h at



60 °C.

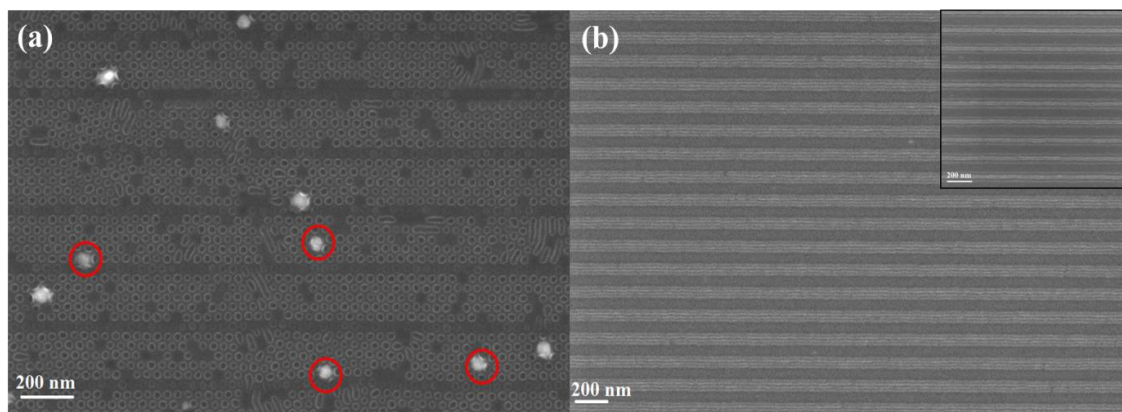


**Figure 5.5.** SEM images of BCP nanopatterns after uv/ozone treatment of HSQ-defined Si substrates by solvent annealing at 60 °C for (a) 1.5 h and (b) 2 h. Pattern degeneration or swelling is shown by the red circles.

Figures 5.5(a) and (b) show the microphase separated BCP nanopatterns in 225 and 90 nm trench width, respectively, at different annealing times on uv/ozone treated substrates. No patterns were observed for the smaller width trenches (45 nm). Figure 5.5(a) shows well-ordered arrays of dots for an annealing time of 1.5 h in 225 nm trenches. The HSQ sidewalls of the trenches were affected by the uv/ozone treatment, as observed from both the images in Figure 5.5. In a few places, pattern degradation and/or swelling was noticed with similar translational order, though dot patterns were predominant, as pointed out by the red circles in Figure 5.5(a). Disorientation of the PEO nanodots became more prominent with a further increase in the trench widths, which might be due to erosion of HSQ during or after the ozone treatment. Figure 5.5(b) shows an SEM image of the BCP patterns obtained for an annealing time of 2 h in a 90 nm pitch trenches. On comparing Figures 5.5(a) and

(b), the obvious difference is seen in the orientation of the BCP. Long range well ordered PEO cylinders parallel to the substrate in the PS matrix were observed. Two continuous arrays of BCP line patterns of more than 3-5  $\mu\text{m}$  can be seen. The arrays were continuous with the PEO cylinders residing within the trench, whereas the PS wets the sidewalls, as seen from the inset of Figure 5.5(b). There was no change in the cylinder-to-cylinder spacing observed. However, as mentioned above the HSQ lines did not abide on the substrate and it can be presumed that the ozone treatment must have initiated the HSQ removal since this effect was not observed in non-ozone treated substrates. Moreover, post ozone treatment, the HSQ lines guided the arrangement of the BCPs depicting that the HSQ structures must have eroded during ethanol etch.

### 5.1.2 Iron Inclusion

As stated before in Section 5.1.1 of this Chapter, the nanopatterns formed from PEO-*b*-PS were used to create ordered oxide nanostructures by a metal inclusion method. The precursor iron (III) nitrate nonahydrate in anhydrous ethanol solution (0.4 wt.%) was spin-coated onto HSQ-patterned Si substrates and subjected to uv/ozone treatment. The uv/ozone treatment ensured the formation of iron oxide nanopatterns, which was then used as hardmask for transferring the pattern into a Si substrate. In order to create well-ordered nanodots or nanowires arrays, the best quality BCP nanopatterns substrates were selected, *i.e.* films annealed at 60 °C for 1.5 h with HSQ-etched Si trenches for the dots and films annealed at 60 °C for 2 h with uv/ozone -treated HSQ trenched Si substrate for the wires.

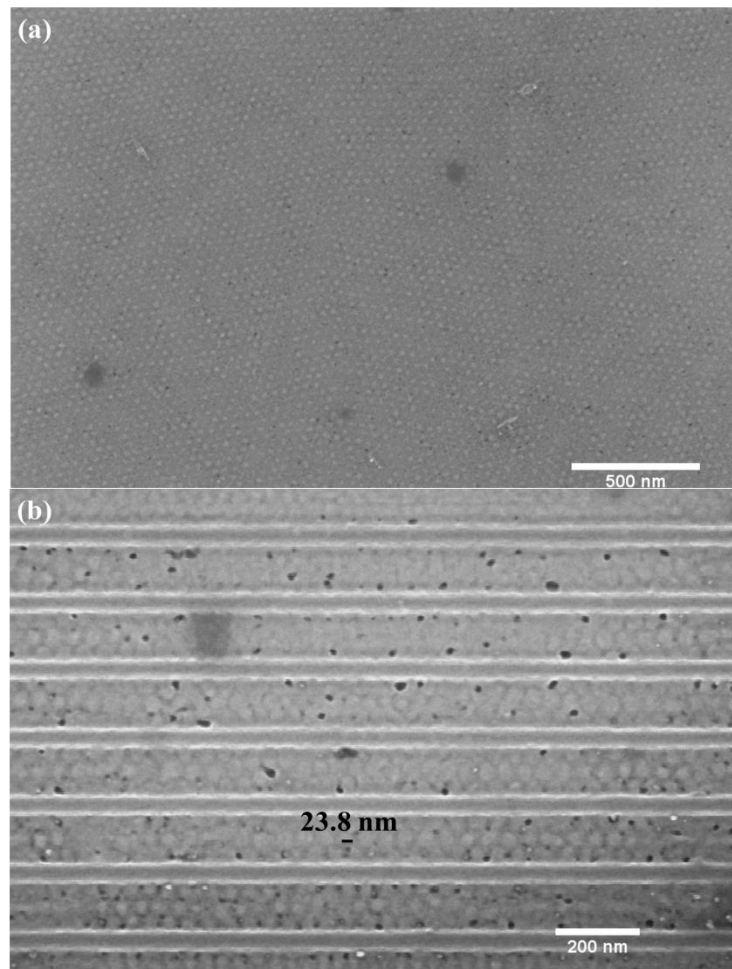


**Figure 5.6.** SEM images of hexagonal ordered oxide nanodots after uv/ozone treatment on (a) an unpatterned area and (b) in-between 135 nm HSQ trenches.

Figure 5.6(a) represents the SEM images of iron oxide nanodots prepared after uv/ozone treatment of the BCP film impregnated with iron (III) nitrate nonahydrate on an unpatterned area. Iron precursors of different concentrations were used to achieve well-ordered iron oxide arrays of nanodots and continuous defect-free nanowires within the trenches. At a precursor concentration of 0.4 wt.%, well-ordered arrays of iron oxide ( $\text{Fe}_2\text{O}_3$ ) nanodots arrays were obtained. Figure 5.6(b) shows metal oxide dots within 135 nm sized HSQ trenches, highlighting that the dimension of the iron oxide structures are equivalent to that of the BCP domain. The

mean diameter of the nanodots remained unchanged after iron inclusion, *i.e.*  $\sim 20$  nm with a spacing of 42 nm. The concentration of the iron precursor solution was critical and was carefully optimised to obtain isolated and continuous nanowires.<sup>26</sup> Due to the hydrophobic nature of PS, the probability of the metal ion inclusion in the PS area was excluded; thereby metal ions occupy PEO activated sites. The PEO-ethanol layer accelerated the metal ion inclusion process via electron donation from the PEO block to oxygen species in the ethanol molecule.<sup>26,28</sup> Also evident from the SEM images in Figure 5.6, the metal oxide was formed in the PEO sites confirming the presence of partial PEO after ethanol treatment. The uv/ozone treatment after spinning the metal precursor ensured the oxidation of metal complex and simultaneous removal of the surrounding polymer. Thusly formed iron oxide nanopatterns hardmask were then subjected to ICP etch process to transfer to DSA patterns in the Si.

### 5.1.3 Pattern Transfer

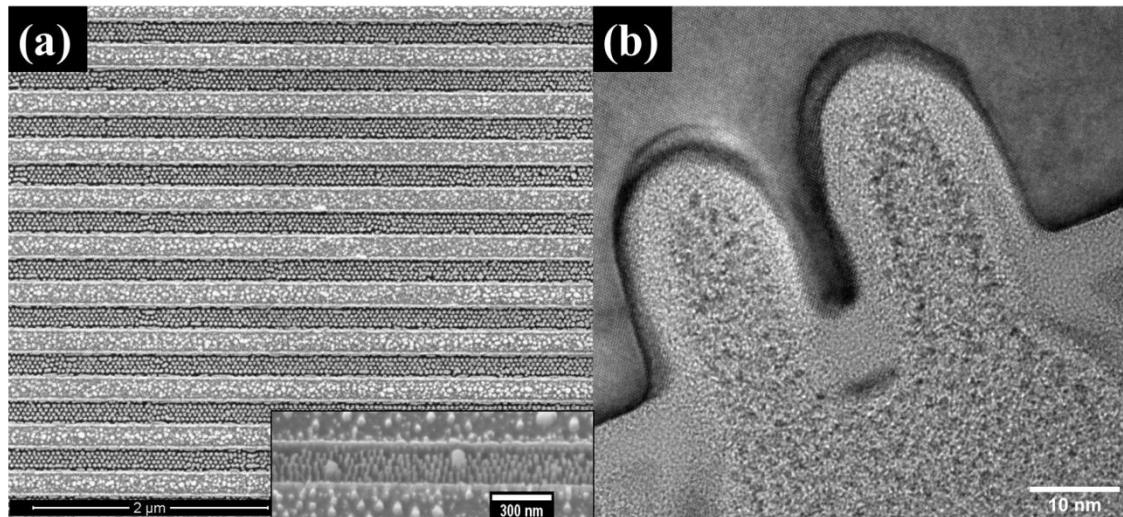


**Figure 5.7.** (a) SEM image of  $\sim 180$  nm pitch, RIE etched HSQ trenches; (inset)

*tilted SEM images showing height Si nano pillars and (b) high resolution TEM cross-sectional image of the Si nanopillars.*

Figure 5.7 illustrates an SEM image of Si nanopillars obtained by etching the iron oxide hardmask over an unpatterned area, confirming that pattern transfer via this route was successful and providing evidence of the mechanical robustness of the hardmask. The depth of the nanorods/wires could be varied by increasing the Si etch time. Figure 5.7(a) reveals well-ordered arrays of Si nanorod within 180 nm wide etched trenches etched for 2 min. A higher magnification image (inset of Figure 5.7(a)) demonstrates the equal diameter of the nanorods throughout the entire length (20 nm). The cross-sectional SEM image also confirms the uniform width and smooth sidewalls, demonstrating the mask effectiveness. The centre-to-centre spacing remained unchanged, implying that the etching did not damage the original ‘mask’ to a significant extent. The nanopatterns remained unaffected with increasing etch time, whereas nanowire discontinuity was observed in few areas for longer etch times, *i.e.* more than 2 min. However, it was not clear whether the discontinuity was due to etch degradation or mechanical weakness of the samples. Cross-sectional TEM was used to fully characterise the nanowires. Figure 5.7(b) shows TEM images of an array of Si nanopillars achieved after a 60 s etch within a 180 nm size trenched substrate, with iron oxide at the top (therefore, the bright contrast).

### 5.1.4 Discussion

Among the PS-*b*-PEO blocks, PS block is hydrophobic in nature whereas the PEO block was hydrophilic. In the etched substrates, shown in Figures 5.4(a) and (b), where the sidewalls of the trenches were bulk Si, the PS matrix was found to preferentially wet the Si walls. The PEO block was removed during ethanol treatment. Hence, the area where the PEO block was present appeared darker as compared to the grey area which was the PS matrix. The BCP solution was spun onto the etched substrates without any pre-treatment of the surface. The Si surface could be assumed to be mostly hydrophobic in nature, as could the sidewalls of the trenches. The PS block, due to its hydrophobic nature, tended to wet the Si sidewalls and to have more affinity towards the substrate material is in accordance with literature.<sup>29,30,31</sup> Moreover, it has been reported that the PEO block preferentially interacts with hydrophilic substrates.<sup>32</sup> On the other hand, as shown in Figure 5.4, on the ozone-oxidised substrate the voids, where the HSQ gratings were present, were engulfed with darker areas, suggesting that the PEO block occurred exclusively on the HSQ sidewall (prior to removal). The cylindrical PEO structures also appeared to be more inclined towards the HSQ void area. This can be explained by simple hydrophobic-hydrophilic interactions. The HSQ, after EBL exposure, formed a silica-like material which was hydrophobic in nature. When the HSQ predefined substrates were subjected to uv/ozone treatment, the HSQ reactive sites (Si-H) were easily converted into Si-OH (silanol) by ozone.<sup>33</sup> Thus, the HSQ walls will bear Si-OH (making them hydrophilic) groups that can readily bond with the oxygen in PEO. Thus the hydrophobicity of the BCP and trench sidewalls plays a pivotal role in the orientation of the BCP. Moreover, when the substrates were uv-oxidised, a



SiO<sub>2</sub> layer of ~6 nm formed the top surface layer.<sup>34</sup> Due to the difference in the surface energy between uv-oxidised and bare Si surfaces, the BCP arranged into lamellar cylinders on the latter substrate. However, it should be noted that this phenomenon was only observed in the 90 nm pitch while larger pitches exhibited PEO dots arranged in an orderly manner. Thus, the sizes of pitch along with the surface conditions were important for line structures of the BCP.

### 5.1.5 Conclusion for Silicon

In this Section, the DSA of the BCP PS-*b*-PEO on Si substrates was demonstrated. High-resolution HSQ resists were used to pattern Si substrates with trenches of different widths. The solvent annealing conditions of the BCP film were varied on the different substrates. The data showed the effects of these conditions on the DSA of the BCP. On an untreated Si surface the BCP formed an orderly arrangement of nanodots within the trenches defined by the HSQ resist. Etching of HSQ lines into the Si substrate helped to achieve commendable PEO lamellar between in the smallest pitch size of 90 nm. Uv/ozone oxidation of the Si substrate after EBL process was found to yield an excellent DSA throughout the HSQ trenches but, at the cost of HSQ structures at the end of the process. The placement of BCP within the trenches depended highly on the interaction with the sidewalls of the trenches with the individual blocks of the BCP. The pattern transfer of BCP microdomains via RIE etch was also successful by iron oxide inclusion and subsequent uv/ozone treatment.

## 5.2 Germanium Substrates

### 5.2.1 DSA on Ge with varied surface conditions

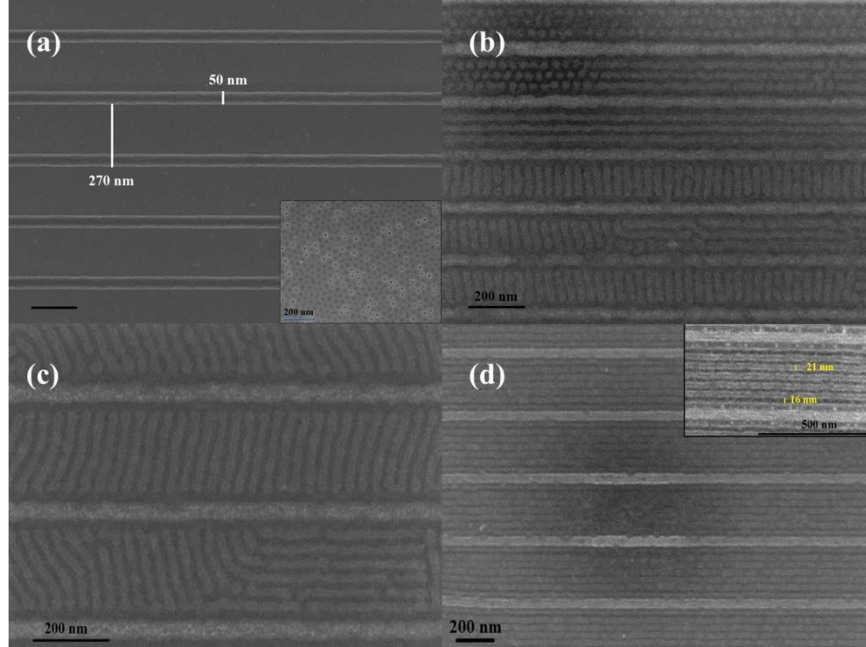


**Figure 5.8.** SEM images of (a) HSQ gratings fabricated using a novel Ge cleaning and passivating process, having a line width of 50 nm and a trench width of 270 nm (inset: PEO cylinders in unpatterned substrate area). Directed self-assembly of PS-*b*-PEO with HSQ trenches of width (b) 180 nm (c) 225 nm (d) 270 nm on Ge substrates.

50 nm wide HSQ gratings patterned by EBL on Ge substrates, using a novel citric acid treatment as described in Chapter 2, Section 2.2.2 of this thesis, are shown in Figure 5.8(a).  $25 \times 25 \mu\text{m}$  sized arrays of HSQ gratings with different trench widths of 45, 90, 135, 180, 225, 270 and 315 nm were fabricated on Ge surfaces. Trenches at increment sizes of 45 nm were produced, as 40 nm was the periodicity of the PEO-*b*-PS BCP on Si substrates to allow adequate mobility of the BCP segments



during solvent annealing. The self-assembly of PS-*b*-PEO di-block copolymer films was observed on the pre-patterned Ge substrates, with or without treating them with citric acid prior to spin-coating the BCP film. Following the microphase separation of the BCP thin film by solvent annealing (60 °C for 2 h), the topography of the substrate on an unpatterned area is shown in the inset in Figure 5.8(a). PS-*b*-PEO formed PEO cylinders in a PS matrix perpendicular to the substrate surface, a dot morphology, as shown in the inset of Figure 5.8(a). The difference in contrast between the two blocks was achieved only after the substrates were subjected to 15 h of ethanol treatment, as explained in Section 5.1.1 of this Chapter. This crucial step is described as the ‘activation step’ and is advantageous for hardmask fabrication, by incorporating the metal oxides in the PEO domain. The PEO block swells during ethanol treatment and partially etches the block during the activation step.<sup>26,35</sup> The substrates were subsequently imaged by SEM. Figure 5.8(a) shows that PEO dots morphology arranges randomly in the absence of a guiding template and this was observed in all open areas. The centre-to-centre distance between two PEO cylinders was ~42 nm and the PEO dots had a mean diameter of ~20 nm. Due to the lower surface energy of PS (33 mN/m) compared to PEO (43 mN/m), PS preferred to remain at the air interface whereas PEO will wet the Ge surface.<sup>30</sup>

Figures 5.8(b) to (d) show SEM images of the BCP alignment within different sized HSQ trenches on the same chip. The BCP thin film was spin-coated onto a Ge substrate after rinsing in DI water only and drying thoroughly under N<sub>2</sub>. In the 90 nm HSQ trenches only one row of dot structures were observed within an individual trench. As the trench width was increased, lamellar structures began to appear

within the trenches along with dots. Figure 5.8(b) depicts the BCP arrangement in a 135 nm-sized trench. PEO cylinders, parallel to the substrate began to appear regularly at this point. Shorter length BCP lines were also observed to align parallel as well as perpendicular to the HSQ lines, suggesting that the 135 nm trench size was adequate to commence the phase separation of the BCP into lines domains. As the trench size was further increased to 225 nm, as seen in Figure 5.8(c), only lamellar structures were observed. However, alignment perpendicular to the HSQ lines was commonly observed in this trench. Figure 5.8(d) shows an SEM image of a perfect array of BCP lines parallel to the HSQ trenches with a width of 270 nm. This phenomenon was also observed in trench sizes of 315 nm. Good quality and long range arrangement of array of BCP lines were observed only in the widest trenches amongst all the HSQ trenches and was observed in all of the Ge chips that were processed in such way. This result was in contrast with those obtained on Si substrates with the same BCP and conditions as described in Section 5.1.1 of this Chapter, where it was found that lamellar structures were only obtained in the smaller trench width of 90 nm and not in wider trenches on Si. Hence the PS-*b*-PEO BCP interacts differently with a Ge compared to a Si surface.

On Ge, larger guiding areas up to a certain dimension, i.e. more than 250 nm, were required for parallel nanowires-like arrangement. This remarkable phenomenon observed on Ge could be attributed to the surface chemistry of Ge, which differs from that of Si. As mentioned in the introduction of the Chapter 4 of this thesis, the surface of Ge is always accompanied by its native oxides, GeO and GeO<sub>2</sub>. GeO<sub>2</sub> is a water soluble oxide<sup>36</sup>, however in the BCP self-assembly procedure described here is

a completely water devoid process (toluene and ethanol solvents). The presence of surface oxides makes the Ge surface hydrophilic in nature. The surface energy of Ge is reported to be lower than Si, ( $\text{Ge}_{\{100\}} = 1.835 \text{ mNm}^{-1}$  and  $\text{Si}_{\{100\}} = 2.130 \text{ mNm}^{-1}$ ) and hence the PEO block may prefer wetting the Ge surface more effectively than Si.<sup>37</sup> The contact angles measured for untreated GeOI were  $59.6^\circ/60.3^\circ$  (left/right angle) and for citric acid treated GeOI were  $54.7^\circ/57.2^\circ$  (see Chapter 4, Section 4.2.3). Thus, the surface energy of untreated GeOI is 37 dyne/cm and that for citric acid treated is 41 dyne/cm. Hence, this behaviour may favour the long range arrangement of the PEO block. However, PEO cylinders perpendicular to the substrate were mostly found on EBL unpatterned areas, so it is possible that the Ge surface along with the HSQ lines induce the lamella structures within the trenches.

As mentioned in Section 5.1.4 of this Chapter, the HSQ resist after EBL exposure forms a silica-like network which is hydrophobic in nature.<sup>14</sup> The simple hydrophobicity interaction between the polymer and the HSQ sidewalls could be reason for preferential wetting of the BCP on the HSQ sidewalls. Since, it is reported that amid the PS-*b*-PEO pair, PS is the hydrophobic block whereas PEO is the opposite, it is certain that the hydrophilic PEO block would preferentially wet the HSQ sidewall. Thus when the PEO block is partially removed during ethanol etching, the area adjacent to the HSQ walls appear darker in the SEM images. Moreover, as mentioned in Section 5.1.1 of this Chapter, PEO has more affinity for a substrate than an air interface. Si-H and Si-O bonds have been reported to be the reaction sites of HSQ,<sup>29</sup> which can react with those on PEO, eliminating species like ethane and forming  $\text{HSQ}_{\text{bulk}}\text{-Si-O-(PEO)}$  linkages along the HSQ sidewalls, as

suggested in Scheme 5.1. Thus a strong linkage between the PEO and HSQ is established and lateral ordering of the BCP throughout the HSQ trench is possible. The reason why more parallel alignment is observed frequently in wider trenches is because of the scarce availability of SiO (HSQ) material (since the trench-width is wider). As the Ge surface area increases proportionally with the trench width, the surface energy in the confined space decreases causing an increase in the PEO affinity towards the surface and the formation of lamellar structures.



**Scheme 5.1.** Probable mechanism of PEO block's interaction with the sidewalls of HSQ resist

The inset in Figure 5.8(d) shows that up to 8 PEO lines could be accommodated in a trench size of 270 nm, with each PEO line bearing a critical width of between 15-18 nm (PS line widths were measured to be between 20-22 nm).

Prior to imaging the BCP thin films were treated with ethanol for 15 h to partially remove the PEO block. This step was significant for the later stages where a metal oxide hardmask was to be established to etch the BCP patterns into a Ge substrate, as described in Section 5.1.2 of this Chapter. The ethanol treatment induces structural modification within the thin film without altering the dimension of the nanostructures.<sup>26</sup> The process moderately removes the PEO which gives a contrast different to that of PS which is useful during SEM imaging.

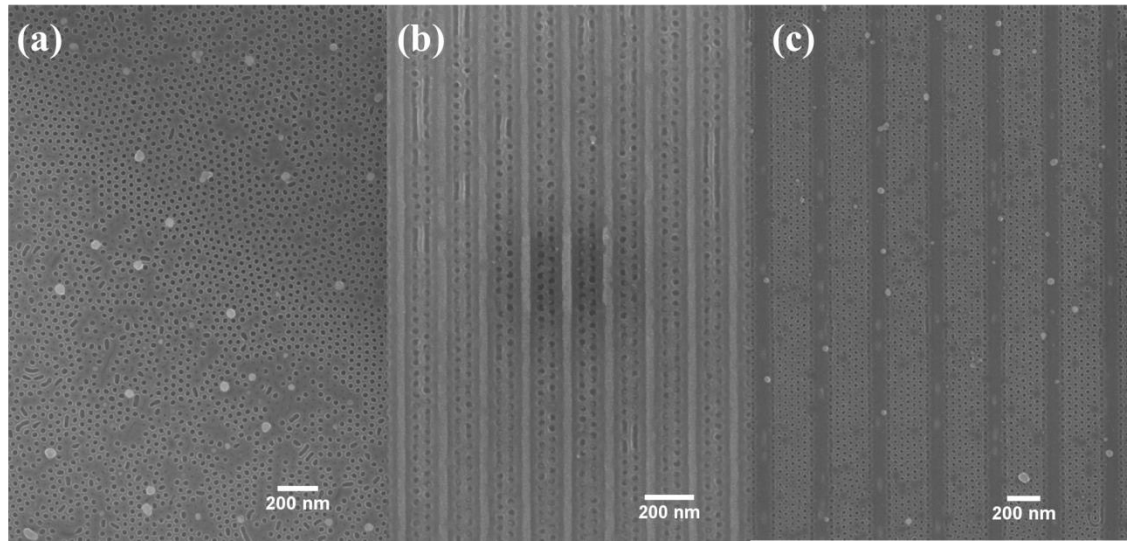


**Figure 5.9.** SEM images of a Ge surface treated with 1 M citric acid prior to BCP processing. DSA of the PEO cylinders in (a) open area showing PEO cylinders, (b) a 135 nm HSQ trench and (c) a 270 nm HSQ trench.

The subsequent step was to conduct the DSA of the BCP on a  $\text{GeO}_x$ -free surface. Such surfaces were created by treating them with 1 M citric acid prior to spinning the BCP thin film. The acid treatment ensured an oxide-free surface, however passivating the substrate with a thin layer of citric acid. Figure 5.9(a) shows an SEM image of the self-assembled BCP thin film on a Ge substrate in an unpatterned area. The PEO dot size measured 20 nm and the centre-to-centre distance was 40 nm. Figure 5.9(b) displays the DSA of the BCP film in a 135 nm HSQ trench and Figure 5.9(c) shows the DSA in a 270 nm HSQ trench. All of the wider HSQ trenches (225, 270 and 315 nm) only produced PEO cylinders, as opposed to the parallel lamellar structures observed in the same trench size on the citric acid untreated Ge substrates. When the Ge surface was treated with citric acid, citrates are probably adsorbed onto the surface giving it a negative zeta potential (depending on the citric acid

concentration).<sup>38</sup> This acid passivation may change the surface energy of Ge and not favour long range arrangement of the BCP domains on the surface.

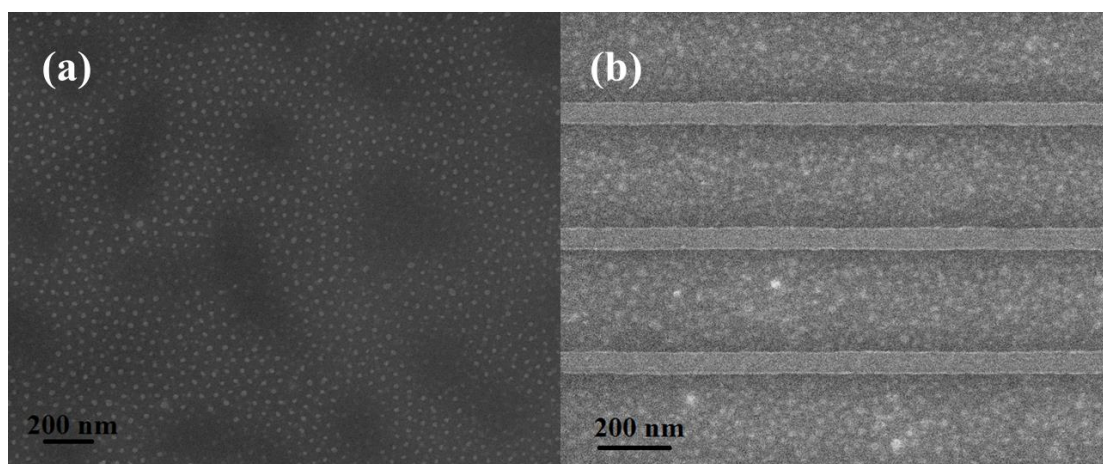


**Figure 5.10.** *Ge surface treated with HCl prior to spinning down a BCP thin film; SEM images after 15 h of ethanol treatment (a) open Ge surface (b) HSQ trench of 315 nm.*

Ge surfaces have previously been cleaned by a process that involves chlorine termination.<sup>39</sup> To verify if the Cl-termination of a Ge surface could aid in the BCP process, one of the HSQ patterned Ge substrates was immersed in 1.3 M HCl concentration solution for 10 min prior to spinning the BCP solution. The BCP thin film was then processed as described in Chapter 2, Section 2.2.3 of this thesis, see Figure 5.10. This process, by no means, proved helpful to the BCP process. Figure 5.10(a) shows the random arrangement of PEO cylinders on an unpatterned Ge surface; the arrangements of the cylinders were nearly hexagonally packed. However, the centre-to-centre distances between two cylinders increased to between 55-60 nm and the size of the dots reduced to between 12-13 nm. There was no

alignment of any cylinder or lamellar structures observed in any of the trenches. The trench size revealed in Figure 5.10(b) is 325 nm, without the presence of definite structures. The HCl passivation does not prefer to wet any of the BCP blocks and thus, results in micellar formation on the surface (as shown in Figure 5.10(a)). PS-*b*-PEO is an amphiphilic polymer that exhibit self-associating properties, which in aqueous solutions tend to aggregate into microdomains promoting the formation of micelles. Thus, the process for cleaning the Ge surface with acids before the BCP process was not particularly fruitful.

### 5.2.2 Iron Inclusion method on Ge

In a bid to transfer the long ranged BCP structures into the Ge substrate, it was necessary to establish a hardmask of the nanopatterns. After the activation step, a 0.4 % wt. of iron nitrate solution was spin-coated on the patterned substrates followed by uv/ozone treatment for 3 h. During the uv/ozone treatment, the metal crosslinks with the PEO blocks and removes the organic compounds present in the solvent and polymers. One of the main reasons for carrying out the ethanol treatment erstwhile is that during the deposition of metal oxide the remaining hydrophilic PEO will aid in absorption of the metal solution into the PEO voids. This is because PEO swells during ethanol treatment and later due to PEO having an affinity towards cations, the incorporation of metal oxide by PEO will speed up.<sup>41</sup> The active sites in PEO are created by the oxygen atoms present in the polymer backbone which interact with the metal ions by intermolecular force of attraction. After this process, iron oxide ( $\text{Fe}_2\text{O}_3$  predominantly) lines and cylinders were obtained which as shown in Figure 5.11. The presence of  $\text{Fe}^{3+}$  ions in the BCP film



is confirmed in a report that elucidated a generic method for the fabrication of highly dense long range hexagonally ordered various inorganic oxide nanodots on different substrates by using a microphase separated BCP.<sup>26</sup>

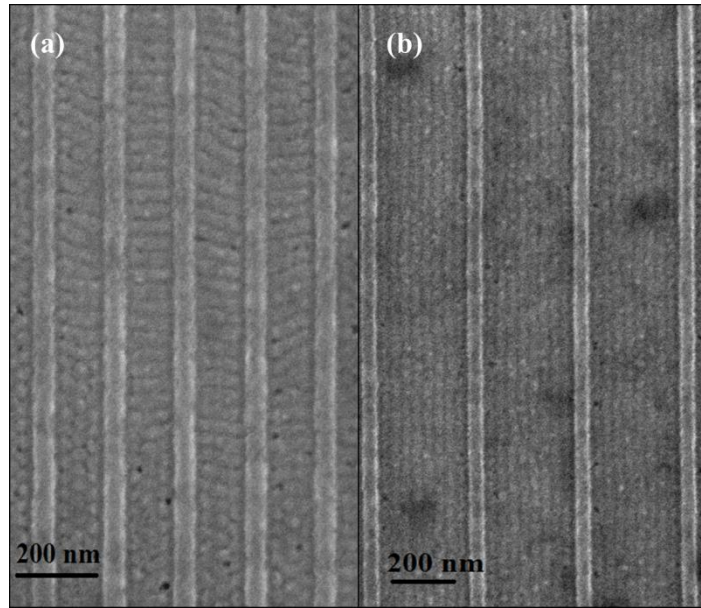


**Figure 5.11.** SEM images of  $\text{Fe}_3\text{O}_4$  lines with (a) 135 nm pitch size and (b) 315 nm pitch size.

Figure 5.11(a) illustrates iron oxide nanostructures obtained by the metal inclusion process in the phase separated BCP. The iron oxide structures form a hardmask for further etching into the Ge. The iron oxide hardmask has been reported to have a good thermal stability and robust adherence to surface at high temperatures.<sup>26,41</sup> The process of iron oxide inclusion did not alter the size of the nanostructures; the centre-to-centre distance of the ferrous oxide dots was measured to be 40 nm in Fig. 5.11(a), whereas the width of the lamellar structures is ~20 nm.



### 5.2.3 Pattern Transfer on Ge

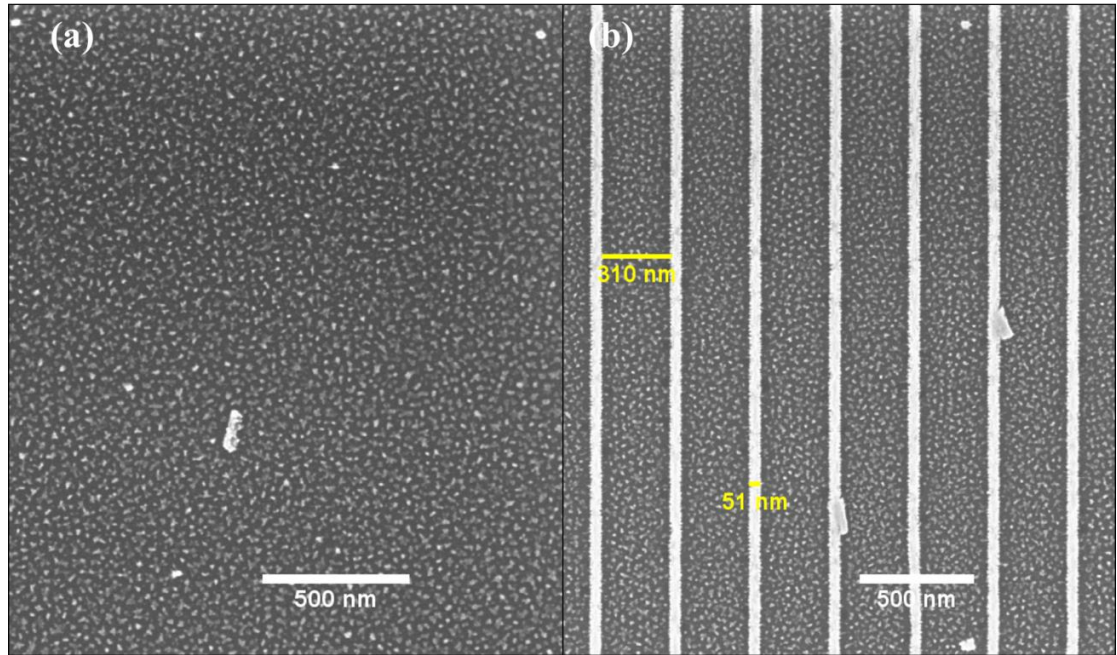


**Figure 5.12.** Top-down SEM images of Ge damaged nanopatterns following pattern transfer with a ferrous oxide hardmask by RIE with  $\text{CH}_4$  for 9 s on (a) unpatterned areas and (b) a 315 nm pitch HSQ trench.

The ferrous oxide nanopatterns were then used as a hardmask to etch the nanopatterns into a functional Ge substrate by RIE, firstly, for 9 s, as described in Section 5.1.3 of this Chapter. A highly selective etch with only  $\text{CH}_4$  gas was employed as it was reported to transfer poly(styrene-*b*-4 vinyl pyridine) BCP pattern efficaciously into Ge substrates.<sup>41</sup> Figure 5.12(a) illustrates Ge nanostructures formed in an EBL unpatterned area. Additionally, the roughness of the HSQ side walls can also be noticed in Figure 5.12(b). This roughness could be due to the fact that the  $\text{CH}_4$  etch chemistry is known to consume HSQ, thus etching it at higher rate than intended and resulting in rougher sidewalls.<sup>29</sup> Figure 5.12(b) demonstrates

damaged Ge nano-lamellar structures within a 315 nm trench, as opposed to the lamellar structures observed in Figure 5.11(b). This etch recipe, or time, proved to overly etch the BCP nanodomains and destroyed the lines as well as dot morphology.

Next, the Ge substrate was etched with the same parameters, but with a reduction in the etch time to 6 s. Figure 5.11 shows the SEM images of Ge nanofins pattern transferred from an iron oxide hard mask. From the SEM images, it is evident that the 6 s etch was also harsh. In the 135 nm pitch trench, discontinuous Ge nanofins laying perpendicular to the HSQ lines can be seen (Figure 5.11(a)). In Figure 5.11(b), 225 nm wide HSQ trenches show up to 4 continuous Ge nanowires parallel to the HSQ lines. However, as evident from Figure 5.11(c), the etching process resulted into disruption of the lines and appears more like nanodots structures. The RIE etch process must thus, be optimised for this BCP system on Ge substrates.

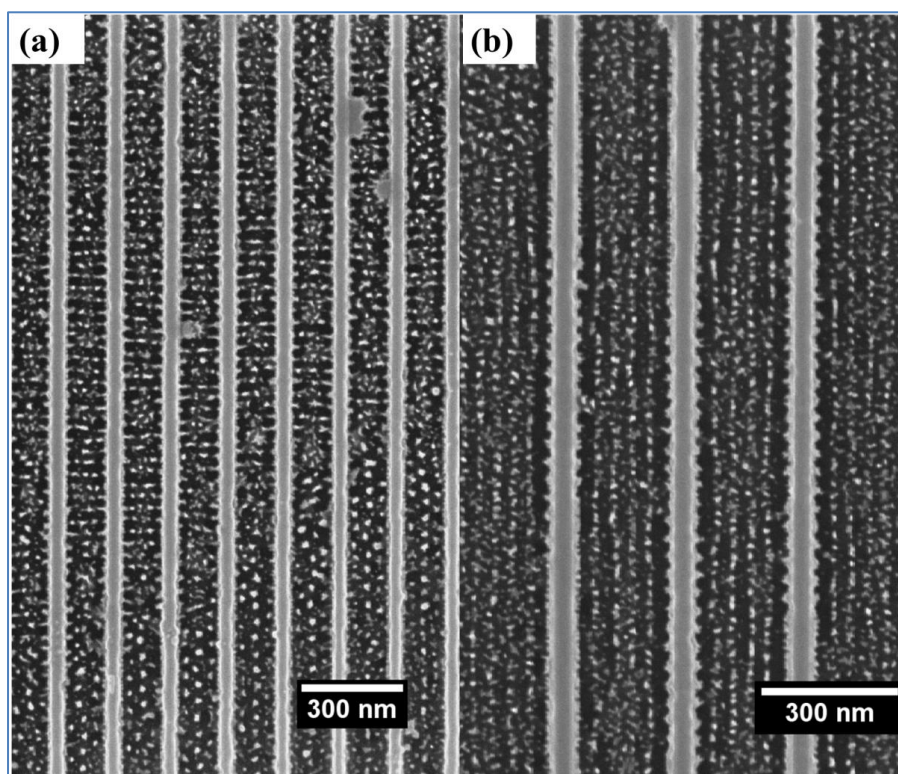


**Figure 5.13.** SEM images of nanopatterns etched in to Ge surface by RIE etch process for a reduced time to 6 s. Pattern transfer in (a) 135 nm and (b) 225 nm wide HSQ trenches.

#### 5.2.4 Conclusion for Germanium

DSA of BCP has been demonstrated on Ge surfaces for the first time in this study. HSQ guides were patterned on the Ge surface by a top-down EBL process. The HSQ trenches acted as guides for the self-assembly of PS-*b*-PEO thin films. Unlike self-assembly on Si, Ge offered long range arrangement of the BCP inside wider trenches. Long range arrangement of 5, 6 and 7 parallel PEO lines were obtained in HSQ trenches with 225, 270 and 315 nm widths, respectively. This phenomenon could be attributed to the lower surface energy of Ge compared to Si, which encourages more lamellar alignment of the BCP on the surface. Moreover, the

native surface oxides of Ge can also be an added benefit for improved alignment, as surface treatment with citric acid or dilute HCl before casting the BCP film resulted in poor quality BCP arrangement/structures. Iron oxide inclusion in the BCP porous template was also successful and was not affected by the change in substrate material (Ge). Etching of Ge using the BCP template using CF<sub>4</sub> for 9 s did not prove to be prosperous whereas, with a reduced time of 6 s the etch condition was slightly improved. However, the etch recipe for the PS-*b*-PEO system on Ge needs to be further optimised.

### 5.3 BIBLIOGRAPHY

1. M.D. Austin, H. Ge, W. Wu, M. Li, Z. Yu, D. Wasserman, S.A. Lyon, S.Y. Chou. *Appl. Phys. Lett.* 2004, **84**, 5299.
2. J.K. Kim, S.Y. Yang, Y. Lee, Y. Kim. *Prog. Polym. Sci.* 2010, **35**, 1325.
3. G. Xia, S.-J. Jeong, J.E. Kim, B.H. Kim, C.-M. Koo, S.O. Kim. *Nanotechnology*. 2009, **20**, 225301.
4. L. M. Demers, D.S. Ginger, S.-J. Park, Z. Li, S.-W. Chung, C. A. Mirkin. *Science*. 2002, **296**, 1836.
5. C. Ross, K. Gotrik, H.K. Choi, K. Aissou, A. Hannon, W. Bai. *SPIE Newsroom*. 2013. DOI: 10.1117/2.1201301.004650.
6. T. Thurn-Albrecht, J. Schotter, G.A. Kästle, N. Emley, T. Shibauchi, L. Krusin-Elbaum, K. Guarini, C.T. Black, M.T. Tuominen, T.P. Russell. *Science*. 2000, **290**, 2126.
7. J.Y. Cheng, C.A. Ross, V.Z.-H. Chan, E.L. Thomas, R.G.H. Lammertink,

- G.J. Vancso. *Adv. Mater.* 2001, **13**, 1174.
8. Y.S. Jung, C.A. Ross. *Nano Lett.* 2007, **7**, 2046.
  9. T. Thurn-Albrecht, R. Steiner, J. DeRouchey, C.M. Stafford, E. Huang, M. Bal, M. Tuominen, C.J. Hawker, T.P. Russell. *Adv. Mater.* 2000, **12**, 787.
  10. S.Y. Yang, I. Ryu, H.Y. Kim, J.K. Kim, S.K. Jang, T.P. Russell. *Adv. Mater.* 2006, **18**, 709.
  11. I. Bitai, J.K.W. Yang, Y.S. Jung, C.A. Ross, E.L. Thomas, K.K. Berggren. *Science*. 2008, **321**, 939.
  12. S. Xiao, X.M. Yang, E.W. Edwards, Y.-H. La, P.F. Nealey. *Nanotechnology*. 2005, **16**, S324.
  13. S.-J. Jeong, J.Y. Kim, B.H. Kim, H.-S. Moon, S.O. Kim. *Mater. Today*. 2013, **16**, 468.
  14. D. Borah, S. Rassapa, M.T. Shaw, R.G. Hobbs, N. Petkov, M. Schmidt, J.D. Holmes, M.A. Morris. *J. Mater. Chem. C*. 2013, **1**, 1192.
  15. X.M. Yang, S. Xiao, Y. Hsu, M. Feldbaum, K. Lee, D. Kuo. *J. Nanomater.* 2013, **2013**, 615896.
  16. J.G. Son, J.-B. Chang, K.K. Berggren, C.A. Ross. *Nano Lett.* 2011, **11**, 5079.
  17. D.O. Shin, B.H. Kim, J.-H. Kang, S.-J. Jeong, S.H. Park, Y.-H. Lee, S.O. Kim. *Macromolecules*. 2009, **42**, 1189.
  18. T. Ghoshal, R. Senthamaraiannan, M.T. Shaw, J.D. Holmes, M.A. Morris, *Nanoscale*. 2012, **4**, 7743.
  19. M.A. Morris, D. Borah, T. Ghoshal, P. Mokarian. *Google patent*. EP2594995 A1.
  20. T. Wahlbrink, T. Mollenhauer, Y.M. Georgiev, W. Henschel, J.K. Efavi,

- H.D.B. Gottlob, M.C. Lemme, H. Kurz, J. Niehusmann, P. Haring Bolivar. *Microelectron. Eng.* 2005, **78**, 212.
21. X. Zhang, B.C. Berry, K.G. Yager, S. Kim, R.L. Jones, S. Satija, D.L. Pickel, J.F. Douglas, A. Karim. *ACS Nano*. 2008, **2**, 2331.
22. D. Borah, T. Ghoshal, M.T. Shaw, A. Chaudhari, N. Petkov, A.P. Bell, J.D. Holmes, M.A. Morris. *Nanomater. Nanotechnol.* 2014, **4**, 25.
23. T. Ghoshal, R. Senthamaraikannan, M.T. Shaw, J.D. Holmes, M.A. Morris. *Adv. Mater.* 2014, **26**, 1207.
24. G. Kim, M. Libera. *Macromolecules*. 1998, **31**, 2569.
25. G. Kim, M. Libera, *Macromolecules*. 1998, **31**, 2670.
26. T. Ghoshal, M.T. Shaw, C.T. Bolger, J.D. Holmes, M.A. Morris. *J. Mater. Chem.* 2012, **22**, 12083.
27. C. Cummins, R.A. Kelly, A. Gangnaik, Y.M. Georgiev, N. Petkov, J.D. Holmes, M.A. Morris. *Macromol Rapid Commun.* 2015, **36**, 762.
28. C.B. Tsvetanov, R. Stamenova, D. Dotcheva, M. Doytcheva, N. Belcheva, J. Smid, *Macromol. Symp.* 1998, **128**, 165.
29. R.G. Hobbs, R.A. Farrell, C.T. Bolger, R.A. Kelly, M.A. Morris, N. Petkov, J.D. Holmes. *ACS Appl. Mater. Interfaces*. 2012, **4**, 4637.
30. T. Ghoshal, T. Maity, R. Senthamaraikannan, M.T. Shaw, P. Carolan, J.D. Holmes, S. Roy, M.A. Morris. *Sci Rep.* 2013, **3**, 2772.
31. R.A. Farrell, N. Petkov, M.A. Morris, J.D. Holmes. *J. Colloid Interface Sci.* 2010, **349**, 449.
32. R.A. Farrell, T.G. Fitzgerald, D. Borah, J.D. Holmes, M.A. Morris. *Int. J. Mol. Sci.* 2009, **10**, 3671.

33. L. Spialter, L. Pazdernik, S. Bernstein, W.A. Swansiger, G.R. Buell, M.E. Freeburger. *J. Am. Chem. Soc.* 1971, **93**, 5682.
34. C.K. Fink, K. Nakamura, S. Ichimura, S.J Jenkins. *J. Phys.: Condens. Matter.* 2009, **21**, 183001.
35. A. Chaudhari, T. Ghoshal, M.T. Shaw, C. Cummins, D. Borah, J.D. Holmes, M.A. Morris. *Proc. SPIE Advances in Patterning Materials and Processes XXXI*, 2014, 905110.
36. P.W. Loscutoff, S.F. Bent. *Annu. Rev. Phys. Chem.* 2006, **57**, 467.
37. R. J. Jaccodine. *J. Electrochem. Soc.* 1963, **110**, 524.
38. Y.-K. Hong, D.-H. Eom, S.-H. Lee, T.-G. Kim, J.-G. Park, A.A. Busnain. *J. Electrochem. Soc.* 2004, **151**, G756.
39. R.G. Hobbs, M. Schmidt, C.T. Bolger, Y.M. Georgiev, P. Fleming. *J. Vac. Sci. Technol. B.* 2012, **30**, 041602.
40. C.B. Tsvetanov, R. Stamenova, D. Dotcheva, M. Doytcheva, N. Belcheva, J. Smid. *Macromol. Symp.* 1998, **128**, 165.
41. C. Cummins, A. Gangnaik, R. Kelly, A. Hydes, J. O'Connell, N. Petkov, Y.M. Georgiev, D. Borah, J.D. Holmes, M.A. Morris. *J. Mater. Chem. C.* 2015, **27**, 6091.



# CHAPTER 6

---

## CONCLUSIONS



## 6. CONCLUSION

Nanolithography is concerned with the top-down fabrication of structures and devices at the nanoscale. Chapter 1 of this thesis highlighted the nanolithographic technique of electron beam lithography (EBL) and reviewed the resists required for EBL-based nanofabrication. Various classes of resists that have been introduced in the past 5-6 years were reviewed, *viz.*, emphasising their synthesis, exposure and development parameters, resolution and their compatibility as EBL resists. A brief outline of bottom-up nanofabrication with block copolymers (BCPs) and graphoepitaxy methods, which involves the amalgamation of top-down-EBL and BCP technologies, were also described.

In the Chapter 2, all the physical tools utilised in the research reported in this thesis were detailed. Subsequently, the experimental protocols described in Chapters 3 to 5, *i.e.* resists evaluation, fabrication of Ge nanostructures and the processes involved in the directed self-assembly of the BCPs on EBL patterned substrates were described.

Chapter 3 of this thesis presents a study on a novel, positive-tone EBL resist known as SML and compares its lithographic performance to well-established positive resists: PMMA (polymethyl methacrylate) and ZEP 520A. From the contrast curve studies of SML, ZEP and PMMA, the SML resist was observed to possess a high contrast of about 12 with a 7:3 IPA:water developer, which was equivalent to that of ZEP and PMMA. The sensitivity of SML was however lower than the other two resists, which can account for its minor drawback, as the lower sensitivity can increase exposure times with SML. Single pixel lines exposed on the resist revealed

that high-resolution structures down to a linewidth of 15 nm (30 nm pitch) with a mean line edge roughness (LER) of 0.227 nm ( $3\sigma$  value) was achievable with SML. The smallest linewidths resolved in ZEP and SML resist, *i.e.* 7 and 5 nm, respectively, were also reported in Chapter 3. Such resolutions are of great interest for microelectronic device fabrication. Assessment of SML's etching and metal lift-off ability showed that SML was a good candidate for both the processes. Etch data showed that etching was more uniform with SML since no feature widening and bridging was observed in contrast to ZEP. Using SML, dense (40 nm pitch) metal lines of 15 nm linewidth were readily achievable with a basic lift-off technique. The larger process window for EBL exposure dose confirmed that SML was more commendable than ZEP resist. Roughness of SML and ZEP resists, along with incrementing e-beam doses, showed the effect of surface irregularity on the lithographic performance of the two resists. SML exhibited a lower surface roughness as a function of exposure dose when compared to ZEP, which was also reflected in the LER of the EBL patterned structures. Thus, the effect of initial surface roughness of a resist eventually determines the quality of the patterned lithographic structures. As a final point, FTIR was conducted on SML, ZEP and PMMA resists to identify the chemical composition of the SML resist. SML was determined to have a composition based on a methyl acrylate backbone. The chemical structure of SML was very similar to those of PMMA and ZEP resists. SML contains a methylstyrene group which was absent in PMMA, but present in ZEP. The presence of this group in SML was the rationale for its higher sensitivity compared to the other two resists. However, the methyl styrene group was the reason why SML and ZEP exhibited high etch resistances. ZEP resist includes a chlorine group in its structure which makes it highly sensitivity, which was lacking in the

SML and PMMA resists. In conclusion, a comparative study of SML to PMMA and ZEP resists was presented, which determined its proficiency as an EBL resist for semiconductor nanofabrication.

The problem of application of hydrogen silsesquioxane (HSQ)-EBL patterning on germanium surfaces has been addressed in the past due to the poor adhesion between HSQ and Ge. In Chapter 4 of this thesis, a simple solution for eliminating the adhesion issue was demonstrated. The difficulty of adhesion arises due to the presence of native oxides on Ge surfaces, which are water soluble in nature. HSQ requires an aqueous based developer that can easily “wash away” the EBL exposed HSQ structures. Two common acid solutions, namely citric acid and acetic acid, have been shown to successfully remove surface Ge oxides. These acids also passivate the Ge surface with carboxylic groups which further aids in having oxide-free surfaces for up to 1 h, which is enough time to carry out EBL exposures. In this Chapter, high resolution HSQ gratings down to ~5 nm were patterned on Ge surfaces. Such critical dimension structures anchored onto Ge surfaces efficaciously and could withstand dry chemical etch processes. FTIR measurements of the Ge surfaces treated with citric acid and acetic acid confirmed the passivation of the surfaces with carboxylic group. A reaction pathway for the surface passivation with the acids followed by HSQ adhesion was also proposed in this Chapter. Moreover, the applications of this technique for fabricating Ge nanowire devices were demonstrated. The acid treatments did not interfere with further processing or characterisation steps (electrical measurements or graphoepitaxy with block copolymers). These applications proved the acid processes are attuned with semiconductor nanofabrication.

Nanofabrication with EBL is often a slow and a low throughput process, especially when dimensions are critical and dense. Directed self-assembly (DSA) of block copolymers (BCPs) on EBL defines surfaces has been considered as an approach to resolve this issue of pattern densification within shorter time, whilst being cost-effective. In Chapter 5 of this thesis, DSA of the diblock copolymer system, poly(styrene-*b*-ethylene oxide) (PS-*b*-PEO) on EBL patterned HSQ resist trenches with various sizes, was presented. The effect on microphase separation of the BCP film by varying conditions such as solvent annealing, temperature and time, trench side-wall variation substrate type, *i.e.* Si and Ge, were analysed. Firstly, optimum solvent annealing times and temperatures were obtained on Si substrates with HSQ resist side walls. The BCP film microphase separate to form hexagonally packed PEO dots of ~20 nm diameter with 40 nm centre-to-centre spacing within the HSQ trenches of various sizes. When the HSQ lines were etched into the Si substrates, the PEO moiety started forming lamellar structures only within the 90 nm trench size. For the next condition, the Si substrates with HSQ trenches were subjected to uv/ozone oxidation prior to depositing of the BCP film. This condition yielded the best results as perfect (2 PEO lines), long range, lamellar arrangement throughout the HSQ side-walls were found in 90 nm HSQ trenches. The substrates were subsequently subjected to iron oxide inclusion and then RIE etch to transfer the BCP patterns successfully into the functional Si layer. In this Chapter, for the very first time, DSA of BCPs on Ge surface was demonstrated. The same BCP system was employed and surface conditions of Ge were varied (to modify the native oxides present on Ge surfaces). HSQ trenches were patterned on Ge and BCP processes similar to Si were carried out on Ge. Significantly, long range order of the BCP,

parallel to HSQ side-walls was found in wide trenches, *i.e.* 225, 270 and 315 nm. The lower surface energy of Ge may be the attributing factor in forming the lamellar arrangement within the wide trenches. Surface conditions were varied by treating the Ge surface with citric acid or HCl acid before spinning the BCP film, but surface passivation could not improve the ordering. The patterned substrates were then subjected to iron oxide inclusion, which was successful. However, the two etch times employed were harsh for the BCP/iron oxide hard-mask resulting in discontinuity in the patterns. Thus, further investigation into the right etch recipe and time of the BCP patterns on Ge surface needs to be conducted.

### 6.1. Future Works

Electron beam lithography is the finest writing pencil known, an advantage that can be used for patterning beyond sub-5 nm regime. Advances in EBL systems have led to reduction in the beam size diameter down to 2 to 1 nm. However, achieving feature sizes equivalent to this small probe size remains difficult to achieve mainly due to the issues with resist morphologies and lithographic processes. To obtain the best outcome from any EBL process, the tool and the resist parameters must be optimised. All the resist parameters collectively described in Section 1.3 of this Chapter determine the quality of a resist. However, it is not always that a single resist will exhibit all the parameters commendably, *i.e.* the resist may have a high resolution but may suffer low sensitivity or etch durability. Due to the growing interest of lithography community to attain high performance lithography, activities have been raised to develop novel EBL resists. In this thesis, a new resist, SML, is characterised for high-resolution EBL. It was clarified that SML resist is a methyl acrylate based resist, like PMMA which, from the beginning of EBL technology, has

been considered to be the pioneer EBL resist due to decent resolution, ease of handling and cost. Many complex resist formulations were seen in Chapter 1 of this thesis, which not only are difficult to synthesise but are not very user friendly. It can be said that if simple PMMA polymer based resists are synthesised, they could offer convenient and low cost EBL patterning, and result into higher throughput. Thus, one of the prospects is to develop such EBL resists. The last segment of work described in this thesis is the graphoepitaxy conducted on Ge surfaces with PS-*b*-PEO BCPs. A successful method to transfer the BCP patterns into Ge functional layer was not understood successfully. Therefore, a suitable etch recipe or even alteration of the hardmask (iron oxide in this thesis) can be part of the further investigation for DSA methods.

Thus, the research reported in this thesis acknowledges various high-resolution, EBL assisted, nanofabrication methods that can be implemented in the semiconductor industry. The results mainly determine nanowire fabrication, having critical dimensions from 5 nm and above. Further investigation into pattern transfer of the EBL structures is required for some processes. Several patterning issues faced during EBL processes have been realised and solutions to them have been reported in this thesis. The presented work is an insight into processes based around electron beam lithography technology.